Doped Semiconductor Nanocrystals: Synthesis, Characterization, Physical Properties, and Applications

Progress in Inorganic Chemistry, **2005**, vol. 54, 47-126

J. Daniel Bryan and Daniel R. Gamelin
Department of Chemistry
University of Washington
Seattle, WA

Abstract.

This review focuses on recent progress in the study of doped semiconductor nanocrystals prepared by direct solution chemical routes. The emphasis is on materials that can be prepared and handled as high-quality colloidal nanocrystalline suspensions, allowing them to be easily processed by a variety of conventional methods and incorporated into glasses, polymers, or hetero-architectures, appended to biomolecules, or assembled into close-packed ordered arrays, and providing many opportunities related to materials processing and nanoscale engineering. In contrast with the tremendous successes achieved with the preparation of pure (and core/shell or related heteroepitaxial) semiconductor nanostructures, solution methods have not yet excelled at preparing doped nanocrystals, but recent advances portend an exciting future for this area. The review is divided into three themes: synthesis of colloidal doped inorganic nanocrystals (Section II), analytical techniques for probing synthesis (Section III), and physical properties of the resulting materials (Section IV). In Section V, examples are presented involving the use of colloidal doped semiconductors as building blocks in higher dimensionality structures. The review focuses largely on 3d transition metal ions as dopants, since those with open d-shell electronic configurations have various unique physical properties including magnetic ground states and low-energy excited states that make them attractive for altering the magnetic, absorptive, photoluminescent, or other physical properties of their host semiconductors.

Keywords: *doped semiconductor nanocrystals, quantum dots, nucleation and growth, spectroscopy, diffraction, microscopy, magnetism, sp-d exchange.*

CHAPTER 2

Doped Semiconductor Nanocrystals: Synthesis, Characterization, Physical Properties, and Applications

J. DANIEL BRYAN and DANIEL R. GAMELIN

Department of Chemistry
University of Washington
Seattle, WA

CONTENTS

Progress in Inorganic Chemistry, Vol. 54 Edited by Kenneth D. Karlin

I. INTRODUCTION

Semiconductor nanocrystals are the subject of a thriving area of physical and synthetic inorganic chemistry (1–8), motivated by both fundamental science and the long-term technological potential of these materials. Semiconductor nanocrystals are already commercially marketed for application as luminescent biolabels (9–11) and have been demonstrated as components in regenerative solar cells (12–14), optical gain devices (15), and electroluminescent devices (16–18). A potentially far greater market awaits these materials in the area of information processing technologies if the numerous and daunting challenges associated with nanoscale technology can eventually be overcome. This chapter focuses on an area of nanoscale semiconductor research that has received relatively little attention, but that will undoubtedly play an increasingly important role in technological applications of these materials, namely, that of doping. It is well known from present semiconductor technologies that the incorporation of impurities or defects into semiconductor lattices is the primary means of controlling electrical conductivity, and may also have an immense effect on the optical, luminescent, magnetic, or other physical properties of the semiconductor. For example, whereas pure stoichiometric ZnO is an insulator, the conductivity of ZnO can be tuned over 10 orders of magnitude with only relatively small changes in the concentrations of native or non-native defects such as interstitial zinc or aluminum. Likewise, it will be imperative to be able to control and understand doping in nanoscale semiconductors if this class of materials is going to evolve into practical applications in electronics or photonics technologies.

One of the most interesting categories of dopants in semiconductors is that of magnetic ions. Semiconductors containing magnetic impurities have been studied for several decades and have come to be known as “diluted magnetic semiconductors” (or sometimes “semimagnetic semiconductors”) (19, 20). Interest in diluted magnetic semiconductors (DMSs) originally arose from the so-called “giant Zeeman effects” observed in the excitonic levels (19, 20). The excitonic Zeeman splittings of DMSs routinely exceed the splittings of the corresponding nonmagnetic semiconductors by over two orders of magnitude, giving rise to possible applications in optical gating (21). More recently, interest in DMSs has turned toward their applications in spin-based electronics technologies, or “spintronics” (22–25). In this area, the giant Zeeman splittings are used to generate spin-resolved conductivity channels in semiconductors. The resulting spin-polarized currents may provide new spin-based degrees of freedom to semiconductor devices that will increase the information content of a charge pulse, and could potentially introduce new functionalities having no analogue in current-based semiconductor technologies. Many of the devices proposed by theoreticians or tested in prototype versions by experimentalists have involved nanoscale DMSs as key functional components (25–32). There is growing interest in understanding the fundamental physical properties of nanoscale DMSs in the forms of quantum dots, wires, and wells for spin-based electronics applications. This nascent field has had several outstanding experimental successes over just the past 5 years, including the demonstration of functional spin-based light emitting diodes, spin filters, and related devices. The future promises to reveal increasingly sophisticated methods for controlling and applying the unique physical properties of nanoscale DMSs in spin-based electronics devices.

Another major category of dopants for semiconductor nanocrystals is that of luminescence activators. Interest in the luminescent properties of pure semiconductor nanocrystals has driven much of the research into these materials for the past decade, and manipulation of the luminescent properties of these nanocrystals by doping with ions such as Mn^{2+} or Eu^{2+} has the potential to broaden the range of useful spectroscopic properties that can be achieved from this class of materials. The prospect of high quantum yields combined with narrow emission line shapes and broadband excitation profiles make these luminescent colloids interesting candidates for optical imaging applications. A third interesting category of dopants are electronic dopants, those that introduce carriers by acting as either shallow donors or acceptors within the semiconductor band structure. Although electronic doping of nanocrystals has not yet been widely explored, it is clear that this area will play a major role in the future of nanotechnology as self-assembled device structures become more accessible.

This chapter focuses on recent progress in the preparation and understanding of doped semiconductor nanocrystals prepared by direct solution chemical routes. The emphasis is on materials that can be prepared and handled as high-quality colloidal nanocrystalline suspensions. The solution compatibility and chemical flexibility of colloidal semiconductor nanocrystals allow them to be easily processed by a variety of conventional methods and incorporated into glasses, polymers, or heteroarchitectures, appended to biomolecules, or assembled into close-packed ordered arrays. This flexibility provides many opportunities related to materials processing and nanoscale engineering. In contrast with the tremendous successes achieved with the preparation of pure (and core/shell or related heteroepitaxial) semiconductor nanostructures, solution methods have not yet excelled at preparing doped nanocrystals, but recent advances portend an exciting future for this area.

In many regards, the field of wet chemical synthesis of colloidal doped quantum dots (QDs) began with a provocative article describing the synthesis, characterization, and remarkable luminescent properties of Mn^{2+}-doped ZnS (Mn^{2+}:ZnS) nanocrystals as powders, not colloids (33). The Mn^{2+}:ZnS nanocrystals described in this chapter were synthesized by reacting diethylzinc with hydrogen sulfide in toluene to precipitate nanocrystalline Mn^{2+}:ZnS powder, which was exposed to 300-nm ultraviolet (UV) curing radiation to optimize its photoluminescent efficiency. Luminescence measurements reportedly showed a dramatic 10^6-fold enhancement of the Mn^{2+} radiative relaxation rates with photoluminescent quantum yields as high as 18% in these doped QDs. This enhancement was attributed to quantum confinement effects within the ZnS nanocrystals that relaxed the electric-dipole forbiddeness of the Mn^{2+} ${}^4T_1(G) \rightarrow {}^6A_1$ radiative transition by unspecified electronic-mixing effects. Although other syntheses of doped semiconductor nanocrystals had been reported previously (34), this article sparked intense investigation into Mn^{2+}:ZnS and related doped semiconductor nanocrystals by several laboratories hoping to verify the amazing properties of these new luminescent materials, and thereby catalyzed exploration into new syntheses of colloidal doped QDs. With time, however, it became evident that the original report had misjudged the radiative emission rates. In a series of thorough investigations of Mn^{2+}:ZnS nanocrystals conducted in several laboratories (35–38), the emission of Mn^{2+}:ZnS QDs was observed to possess a slow decay component that was readily associated with the radiative decay of the ${}^4T_1$ excited state of Mn^{2+} in the ZnS lattice, and the lifetimes of $\sim$2 ms observed in the nanocrystals were similar to that of Mn^{2+} in bulk ZnS (see Section IV.A for further discussion of these experiments). The claims of unprecedented fast radiative decay attributable to quantum confinement were thus debunked, but not before they had imparted a lasting momentum to the interest in this new class of materials. Shortly thereafter, attention also turned to investigation of the magnetic properties of this same class of materials.

The difficulties encountered in early attempts to prepare high-quality doped nanocrystals have drawn attention to the new challenges that arise when doping nanoscale materials with small quantities of impurities. Two categories of new challenges may be identified. The first has to do with the host material, and is concerned with issues such as the enormous surface/volume ratios of nanocrystals and the inherent statistical inhomogeneities of any ensemble of doped nanocrystals. For example, consider the case of an excellent preparation of 5-nm diameter CdSe QDs having a very narrow size distribution. These nanocrystals are made up of ~2400 atoms, ~30% of which are in the outermost layer where they are exposed to solvent and are geometrically relaxed in a lower symmetry environment. Dopants substituting for host cations at these surface sites may differ quite considerably from those in the nanocrystal cores in their geometries, redox potentials, electronic structures, or other physical properties. Figure 1 schematically plots the fraction of atoms within one and two monolayers (MLs) of the surface of a CdSe nanocrystal as a function of nanocrystal diameter. This surface/volume ratio parallels the trend in quantum confinement over the same size range, such that even a statistical distribution of dopants throughout a quantum confined nanocrystal would yield substantial dopant inhomogeneity due to the surfaces, and this inhomogeneity may compromise some of the target physical properties of the doped material.

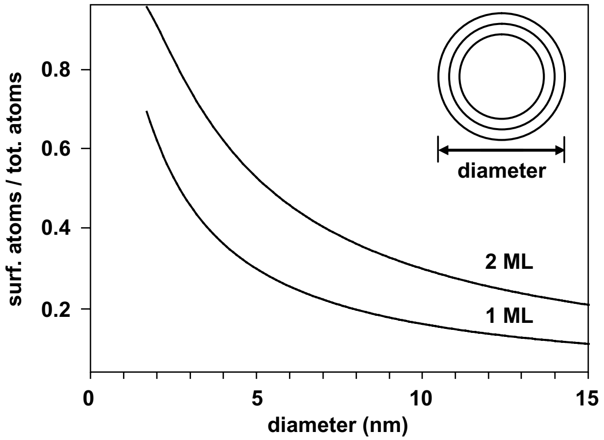

Figure 1. Schematic depiction of the fraction of atoms within one and two MLs of the surface of a hypothetical CdSe nanocrystal, plotted versus nanocrystal diameter.

In addition to surface–volume inhomogeneities, any ensemble of doped nanocrystals will exhibit a range of dopant populations per nanocrystal leading to inhomogeneity in effective dopant concentration among nanocrystals. Dopant distributions among nanocrystals are described using the binomial expression given in Eq. 1, where n is the total number of dopant ions per nanocrystal having N total cation sites available for substitution and x is the dopant mole fraction.

$$P(n \mid N) = \frac{(N)!}{n!(N-n)!}(xN)^n(1-(xN))^{N-n} \tag{1}$$

For $n \ll N$, $P(n \mid N)$ simplifies to $P(n)$, the Poisson distribution.

$$P(n) = \frac{(xN)^n e^{-xN}}{n!} \tag{2}$$

Assuming a uniform nanocrystal size, Eq. 2 yields the dopant distributions shown in Fig. 2(*a*) for ensembles of 5-nm diameter nanocrystals doped at the indicated levels. This model is easily expanded to include nanocrystal size distributions if desired, but already at this stage it is evident that large variations in the doping levels of individual nanocrystals may arise from perfect statistical dopant distributions within an ensemble of nanocrystals. Whereas the dopant concentration may be well defined on average, it follows that the number of dopants in any individual nanocrystal selected for a single-nanocrystal experiment cannot be controlled or even known well. This feature could significantly impact single QD electronics or photonics measurements that rely on doped nanocrystals.

Finally, dopant inhomogeneities due to statistical dopant density fluctuations are also problematic, but this problem is shared with the analogous bulk materials and is not unique to the nanocrystals. Equation 3 describes the probability of finding N nearest neighbors around a central dopant ion in an infinite crystalline lattice for a given dopant concentration, x, where M is the number of cationic sites in the first shell around the central cation (12 in II–VI and III–V semiconductors) (39)

$$P(x) = \frac{M!}{N!(M-N)!}x^N(1-x)^{M-N} \tag{3}$$

From Eq. 3, the probabilities that the central impurity ion is isolated (P_1) or belongs to an isolated pair (P_2), closed triangle (P_{3c}), or open trimer (P_{3o}) within

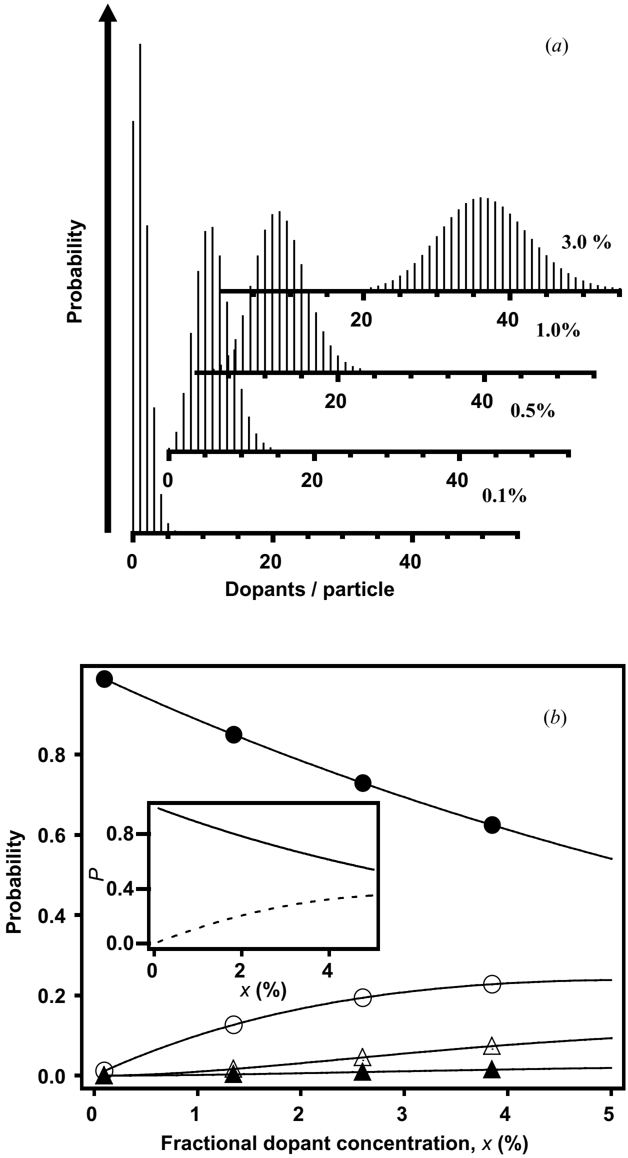

Figure 2. (*a*) Statistical distributions of dopant ions per nanocrystal for various dopant levels (x%) in ensembles of 5.0 nm CdSe nanocrystals. (*b*) Probabilities that a central impurity ion is isolated (P_1, •) or belongs to an isolated pair (P_2, ○), closed trimer (P_{3c}, ▲), or open trimer (P_{3o}, △) within a zinc blende lattice, plotted versus fractional dopant concentration from 0 to 5%. Inset: P_1 (solid line) and the sum of P_2, P_{3c}, and P_{3o} (dashed line).

a zinc blende lattice are given by Eq. 4a–d (40, 41).

$$P_1 = (1 - x)^{12} \tag{4a}$$

$$P_2 = 12x(1 - x)^{18} \tag{4b}$$

$$P_{3c} = 18x^2(1 - x)^{23}(7 - 5x) \tag{4c}$$

$$P_{3o} = 24x^2(1 - x)^{22} \tag{4d}$$

Impurity ions in wurtzite lattices are described by the same expressions for P_1, P_2, and P_{3c}, with a numerically insignificant difference in P_{3o}. These expressions are only quantitatively accurate in the dilute limit, but many of the doped nanocrystals discussed in this chapter fall in this limit. The reader is referred to Ref. 42 for a generalized treatment of the problem. Figure 2(*b*) plots the probabilities calculated from Eq. 4a–d as a function of impurity concentration. The fraction of dopants having at least one nearest-neighbor dopant is quite high even at moderate impurity concentrations (<5%). Needless to say, whereas purification to ensure size uniformity is possible (size-selective precipitation), no purification method has yet been developed for ensuring uniform dopant concentrations in an ensemble of nanocrystals.

The second general category of new challenges has to do with the impurity itself, and may be summed up with the following question: How do we know when nanocrystals have been successfully doped? Whereas molecular inorganic chemists often apply X-ray crystallographic techniques to identify synthetic products, X-ray diffraction studies of doped crystals yield predominantly the characteristic diffraction features of the host and provide little reliable indication of the success or failure of doping. Similarly, whereas a chemist or materials scientist synthesizing nanostructures of pure materials will often turn to microscopy [scanning electron microscopy (SEM), transmission electron microscopy (TEM)] to evaluate the product, nanocrystal doping suffers from the problem that only an extremely small fraction of the product is not the host material, and consequently a doped nanocrystal will be essentially indistinguishable from its pure analogue by these microscopies in most instances. To solve this problem, researchers must turn to other analytical techniques. In particular, spectroscopic methods that are sensitive to some physical property particular to the dopants themselves have proven to be extremely successful. If the dopants are magnetic, then magnetic spectroscopic techniques may be applied to selectively probe them within their diamagnetic hosts. If they absorb light within the forbidden gap of the semiconductor, then absorption spectroscopies may be applied to selectively probe the dopants. In this regard, the challenge of identifying and characterizing a magnetic dopant within an inorganic nanocrystal is in some ways analogous to that of probing the active sites of metalloenzymes (43, 44), which have similarly low concentrations of transition metal cations embedded within large diamagnetic hosts.

This chapter seeks to identify some of the contributions that inorganic chemists can make to the growing field of doping inorganic nanocrystals, which up until recently has been dominated by physicists employing vapor deposition methods (31, 45, 46). This chapter is divided into three themes: synthesis of colloidal doped inorganic nanocrystals (Section II), analytical techniques for probing synthesis (Section III), and physical properties of the resulting materials (Section IV). In Section V, a few examples are presented involving the use of colloidal doped semiconductors as building blocks in higher dimensionality structures. This chapter focuses largely on the use of 3*d* transition metal ions as dopants. Transition metal ions with open *d*-shell electronic configurations have various unique physical properties including the combination of magnetic ground states and low-energy excited states that make them attractive dopants for altering the magnetic, absorptive, photoluminescent, or other physical properties of their host semiconductors. The same unique physical properties allow transition metal ions to be probed directly using various magnetic, optical, and magnetooptical physical methods. Systematic studies of transition metal doping in nanocrystals are then anticipated to provide a solid platform for subsequent electronic doping experiments that may be considerably more challenging to probe experimentally. Finally, this chapter focuses largely, but not exclusively, on II–VI semiconductors, since doped colloids of these have been by far the most thoroughly studied to date. Other semiconductors, other dopants, and doped insulating nanocrystals are discussed only briefly.

II. SYNTHESIS OF DOPED NANOCRYSTALS

A. Synthetic Methods: General Comments

Many approaches have been taken to prepare colloidal doped semiconductor nanocrystals. For example, hot-injection methods have been used to synthesize colloidal Mn^{2+}-doped CdSe (47, 48), ZnSe (49), and PbSe (50) colloidal nanocrystals. Colloidal ZnO DMS–QDs doped with Co^{2+}, Ni^{2+}, and Mn^{2+} have been prepared by low-temperature hydrolysis and condensation (51–54). Sol–gel methods have been used to prepare colloidal doped TiO_2 (55–57) and SnO_2 (58–62) nanocrystals. Inverted micelle methods have been used for preparation of a range of doped II–VI sulfide DMS–QDs at low temperatures (63–68). A high-temperature lyothermal "single-source" method was used to synthesize Co^{2+}- and Eu^{3+}-doped CdSe nanocrystals (69, 70). Autoclaving has occasionally been used to induce crystallization at lower temperatures than reached under atmospheric pressures while retaining colloidal properties, for

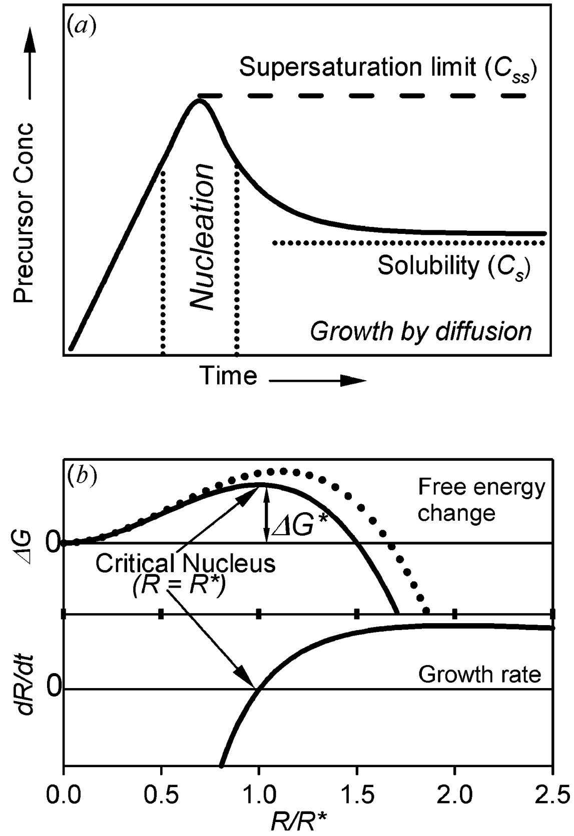

Figure 3. (*a*) LaMer model describing nucleation and growth of crystallites versus time for a constant influx of precursor. [Adapted from (72).] (*b*) Classical nucleation model showing Gibbs free energy change (ΔG) and growth rate (dR/dt) versus crystallite size, R. [Adapted from (73, 74).] Dashed line shows ΔG for nucleation in the presence of a dopant that destabilizes the lattice.

example in the preparation of colloidal doped SnO_2 (58–62) and InAs (71) nanocrystals. Whereas the specific details of these synthetic approaches are extremely important on a case-by-case basis, this section instead focuses on identifying general issues that may be of broad interest to chemists working in this area.

A recurring theme in many studies of nanocrystal doping is the propensity for dopants to be excluded from the internal volumes of the nanocrystals. We therefore begin with a description of crystal nucleation and growth, and of the challenges that arise when impurities are introduced. Exerting control over crystal nucleation and growth is a critical aspect of all nanocrystal research, and is arguably the subject most intensively studied in the area of pure nanocrystals, but has not been examined in sufficient detail for the younger field of doped nanocrystals. The basic model used to describe crystal nucleation and growth in a wet chemical synthesis of colloids first presented by LaMer and Dinegar (72) is summarized in Figure 3(*a*). In this model, a continuous influx of precursors is assumed. When the concentration of precursors in solution reaches a critical level of supersaturation (C_{SS}), spontaneous phase segregation occurs and the dissolved precursor concentration in solution is depleted to below that required for nucleation, but remains above the saturation concentration (C_{S}) such that the crystals continue to grow. Optimization of the experimental conditions to separate nucleation and growth conditions provides the best control over the resulting product. The most successful nanocrystal syntheses therefore exploit exquisite control over nucleation and growth kinetics to yield optimal nanocrystal homogeneity. In so-called hot injection methods (1, 2), for example, solution precursors are mixed rapidly at elevated temperatures to induce crystal nucleation. This injection is accompanied by a crucial drop in temperature that rapidly quenches further nucleation, but allows growth of the crystals from solution nutrient. The kinetic separation of nucleation and growth ensures synchronous nucleation of a well-defined ensemble of crystallites, followed by slower growth from solution, thereby yielding colloids with exceptional homogeneity. Recently, this area has been the subject of several excellent review articles (1, 2) and we use this background as our point of embarkation for discussion of the influences of doping on nanocrystal nucleation and growth.

B. Influence of Dopants on Nanocrystal Nucleation

Crystal nucleation is the chemical reaction that takes solvated precursor ions or molecules into the solid-state crystalline product. To understand the reaction fully, one must understand both its thermodynamic and kinetic aspects. In classical nucleation theory (73, 74), the driving force for spontaneous phase transition is the exothermicity of lattice formation. This driving force is described by the difference in free energies between solvated and crystalline forms of the material, ΔF_{V}, and contributes to the reaction coordinate in proportion to the crystal's volume. For very small crystals with large surface/volume ratios, the volumetric lattice energy is offset by the surface free energy of the crystal, γ, which destabilizes the crystal toward solvation in proportion to the crystal's surface area. The Gibbs free energy change for the reaction is thus described by Eq. 5 (74).

$$\Delta G = 4\pi R^2\gamma + 4/3\pi R^3\Delta F_V \tag{5}$$

Plotting ΔG versus crystal radius yields the reaction coordinate diagram for crystal nucleation and growth. Under diffusion limited growth conditions, the derivative of Eq. 5 with respect to crystal radius R is related to the negative of the growth rate, $-dR/dt$ [Fig. 3(*b*)]. The activation barrier in Fig. 3(*a*) defines the critical radius, $R = R^*$, below which nucleated particles will redissolve $(dR/dt < 0)$ and above which they will survive to grow into larger crystals $(dR/dt > 0)$. This simple model has been improved upon by quantum chemical calculations that yield dynamics and other information unavailable in such a simple formulation (74), but the classical nucleation model describes the principal aspects of this chemistry in a very general and intuitively valuable way. In addition to improved theoretical descriptions of one-step homogeneous nucleation, there is growing evidence that in many cases nucleation proceeds by a two-step mechanism, in which amorphous polynuclear or polymolecular aggregates are formed in the first step, and the second step involves structural reorganization of these clusters into the crystalline form.

The basic physical reasoning behind the classical nucleation model remains unchanged with the introduction of dopants, but the chemistry becomes more complex. Consider the scenario in which a small concentration of an impurity ion that has a substantial incompatibility with the host lattice is introduced to the reaction mixture. An example would be Mn^{2+} in the synthesis of CdSe, for which X-ray diffraction studies of bulk single crystals show large shifts in lattice constants with doping (19), consistent with Vegard's law (75). What would be expected from Eq. 5 in this case? The lattice constant shifts reflect strain within the CdSe lattice upon substitution of a Cd^{2+} ion by a Mn^{2+} ion. This strain manifests itself in Eq. 5 as a sacrifice of some of the driving force for lattice formation, and hence a reduction in the magnitude of ΔF_V. As shown in Fig. 3(*b*), reducing ΔF_V increases the activation barrier for nucleation and increases the dimension of the critical radius. Consequenctly, it is considerably more difficult for the doped crystal to nucleate than it was for the pure host crystal in the absence of impurities. It is reasonable to expect that in a doping experiment involving a mixture of nutrients, nucleation of doped crystals may generally not be kinetically competitive with nucleation of pure crystals. The greater the dopant–host incompatibility, the less likely it is that a critical nucleus will form containing impurity ions. The important observation from this discussion is that crystal nucleation in a mixed solution is governed by the reaction pathway with the most favorable reaction coordinate, and this is typically that of the pure crystalline material. Consequently, the composition of the critical nucleus is likely to be the pure host material in the vast majority of cases. The compositions of critical nuclei are notoriously difficult to determine experimentally, and studies in this area have to date been primarily the domain of theoreticians, who have generally predicted that for spontaneous phase segregation "the properties of a critical nucleus can differ significantly from those of the stable bulk phase that eventually forms" (74), and that by the time the experimentalist can observe it, the composition is generally already that of the bulk material. With doped inorganic nanocrystals attracting increasing interest among experimentalists, some of these ideas are beginning to be tested in new ways.

An experimental confirmation of the theoretician's axiom is found in the synthesis of ZnO nanocrystals doped with Co^{2+} ions, in which crystal compositions at various stages of synthesis were probed by electronic absorption spectroscopy (see Section III.C) (52). A great deal can be learned about the nanocrystal synthesis from monitoring this band-gap absorption during synthesis (76–78), including information about nanocrystal sizes, size distributions, and reaction kinetics. In the case of ZnO, base titration experiments following the reaction in Eq. 6 have proven particularly informative. Figure 4(*a*) shows electronic absorption spectra collected during the titration of reactants in the

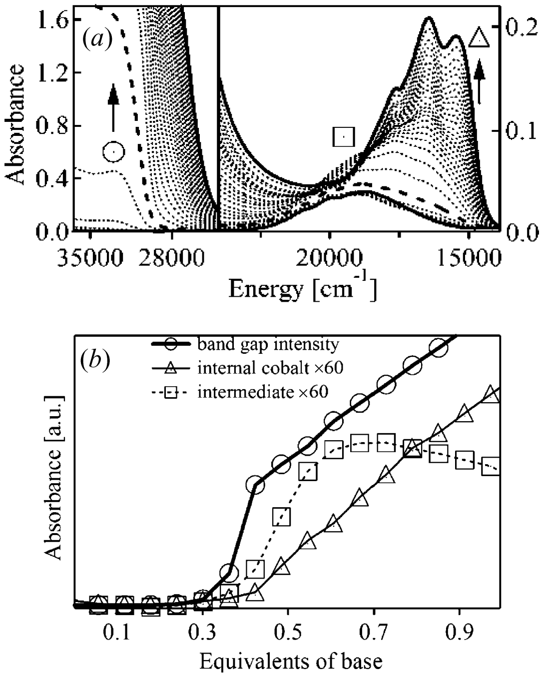

Figure 4. (*a*) Electronic absorption spectra of the ZnO bandgap (left) and Co^{2+} ligand field (right) energy regions collected during titration experiments showing the band gap (○), intermediate Co^{2+} ligand field (□), and substitutionally doped Co^{2+}:ZnO ligand-field (Δ) intensities. (*b*) Intensities of ○, □, and Δ features versus added base equivalents, showing the nucleation of pure ZnO cores followed by substitutional Co^{2+} incorporation into ZnO during nanocrystal growth. [Adapted from (52).]

synthesis of cobalt-doped ZnO. In this experiment, an ethanol solution of $N(Me)_4OH$ was added at room temperature to a solution of $Zn(OAc)_2 \cdot 2H_2O$ and $Co(OAc)_2 \cdot 4H_2O$ dissolved in dimethyl sulfoxide (DMSO) (52).

$$(1-x)\mathrm{Zn(OAc)_2} + x\,\mathrm{Co(OAc)_2} + 2\mathrm{NMe_4OH} \rightarrow \mathrm{Co^{2+}\!:ZnO} + \mathrm{H_2O} + 2\mathrm{NMe_4OAc} \qquad (6)$$

The reaction can be followed by monitoring the characteristic absorption due to ZnO band-gap excitations, occurring at energies above $\sim$28,000 cm^{-1}. The energy of the first excitonic transition depends on the nanocrystal size, and so provides a probe of nanocrystal growth. For a fixed size, the intensity of the transition provides a measure of the nanocrystal concentration (i.e., the yield of the chemical reaction), and this offers a measure of nucleation yields.

As seen in Figure 4, addition of the first few aliquots of OH^- did not nucleate ZnO nanocrystals. This is consistent with the LaMer model summarized in Fig. 3, in which critical supersaturation (C_{SS}) of precursor must be reached before nucleation will occur. Once critical supersaturation is reached, nucleation occurs, and is followed by diffusion-limited growth from solution. The standard representation of the LaMer model describes the case of continuous influx of precursor and considers conditions where C_{SS} is reached only once in the course of the experiment. A modification of this classic diagram to include stepwise precursor addition and multiple crossings above C_{SS} is appropriate for the base titration synthesis of ZnO. Nucleation is detected by the appearance of the characteristic ZnO band-gap absorbance. Zinc oxide growth is base limited and does not dramatically deplete the solution of precursors. Further base addition leads to more ZnO nucleation and a stoichiometric increase in the concentration of ZnO nanocrystals, shown as the increasing ZnO band-gap absorbance with increasing base. The precursors formed under these reaction conditions are polynuclear metal–oxo clusters referred to as basic zinc acetates. The best studied basic zinc acetate cluster is the tetramer, $[(OAc)_6Zn_4O]$, the crystal structure of which is shown in Fig. 5 (79). This tetramer and the related decameric cluster, $[(OAc)_{12}(Zn_{10}O_4)]$, have been detected by desorption chemical ionization–mass spectrometry (DCI–MS) in the analogous synthesis of ZnO in ethanol (80). Extrapolation of the ZnO band-gap absorbance back to zero intensity in Fig. 4(*b*) very nearly intersects the origin of the graph, indicating that the majority of added base was consumed to form ZnO, and hence that the steady-state concentration of precursors is relatively small. Although extremely useful for characterizing the synthesis of ZnO crystals, these data alone do not provide any information about the role of dopants in nucleation. For that information, some dopant-specific analytical probe is required.

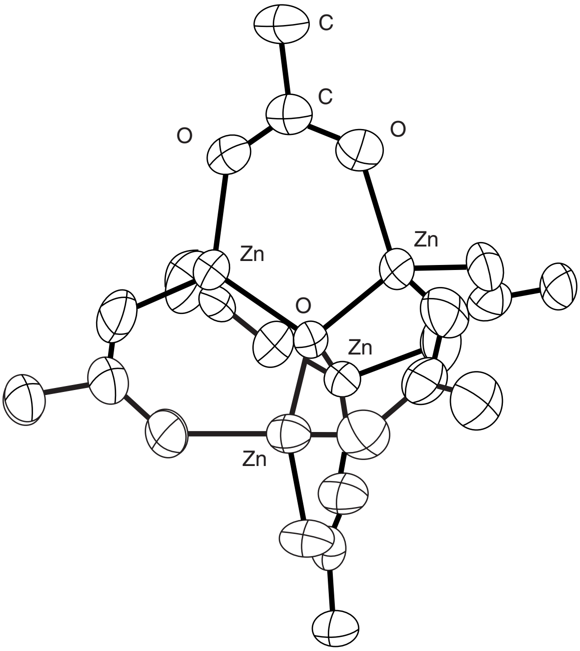

Figure 5. The tetrameric basic zinc acetate cluster, $[(OAc)_6Zn_4O]$. [Adapted from (79).]

In the same samples, a second absorption feature was detected that is associated with the dopant ions themselves. These ligand-field transitions allow distinction among various octahedral and tetrahedral Co^{2+} species and are discussed in more detail in Section III.C. The three distinct spectra observed in Fig. 4(*b*) correspond to octahedral precursor (initial spectrum), tetrahedral surface-bound Co^{2+} (broad intermediate spectrum), and tetrahedral substitutional Co^{2+} in ZnO (intense structured spectrum). Plotting the tetrahedral substitutional Co^{2+} absorption intensity as a function of added base yields the data shown as triangles in Fig. 4(*b*). Again, no change in Co^{2+} absorption is observed until sufficient base is added to reach critical supersaturation of the precursors, after which base addition causes the conversion of solvated octahedral Co^{2+} into tetrahedral Co^{2+} substitutionally doped into ZnO. Importantly, a plot of the substitutional Co^{2+} absorption intensity versus added base shows the same nucleation point but does not show any jump in intensity that would correspond with the jump in ZnO intensity. Instead, extrapolation of the tetrahedral Co^{2+} intensities to zero shows intersection at the base concentration where ZnO first nucleates, demonstrating the need for crystalline ZnO to be present before the conversion of Co^{2+} from octahedral to tetrahedral geometries may occur. These data demonstrate that in the case of cobalt doping into ZnO, the cobalt ions are quantitatively excluded from the critical nuclei. This result may be explained in the context of the classical nucleation theory outlined above.

One remarkable aspect of this chemistry is the sensitivity of the nucleation reaction to such a minor perturbation as replacement of Zn^{2+} by Co^{2+}. Both Co^{2+} and Zn^{2+} ions have essentially identical ionic radii [~0.72 Å (81)], and there is very little ligand-field stabilization energy favoring the octahedral geometry of Co^{2+}. Despite this compatibility, the differences between Co^{2+} and Zn^{2+} are great enough to dominate the course of the reaction even with only 2% Co^{2+}. This remarkable sensitivity is undoubtedly partly attributable to the very small dimensions of the critical nuclei. The size of the critical nucleus is unknown, but may be on the order of only tens of atoms, formed from only a small number of basic zinc acetate clusters. Although the total solution concentration of Co^{2+} may be low, the effective impurity concentration in such a small cluster determines its lattice energy, and so for very small clusters even a single dopant may have a disproportionately large influence on the stability of the crystallite. Other factors may also be important, including the relative solubilities, ligand substitution rate constants, and geometries of Co^{2+} and Zn^{2+} precursors.

Analysis of ZnO nanocrystal yields measured as a function of added Co^{2+} confirms the important influence dopant ions have on nanocrystal nucleation. Figure 6(*a*) plots the ZnO absorption intensity (proportional to percent nucleation), which reflects ZnO concentration in solutions, as a function of added Co^{2+} for reactions run under similar conditions as in Fig. 4. A very strong dependence of the nanocrystal nucleation yield on initial dopant concentration is observed. For example, addition of only 2% Co^{2+} to the starting solution eliminates ~35% of the nucleation events relative to pure ZnO. Nucleation is extremely difficult at Co^{2+} concentrations above ~10–15%. A similar trend is observed for Ni^{2+} doping, which has substantially different ligand substitution chemistry from Co^{2+}. The interpretation of these results is again accessible from the classical nucleation theory diagram in Fig. 3, which shows the increase in activation energy and critical radius upon introduction of impurity ions. From these data it was concluded that basic zinc acetate precursors containing one or more Co^{2+} ions cannot successfully nucleate doped ZnO under these experimental conditions. The extreme sensitivity of nucleation within this relatively small range of dopant concentrations demonstrates the important role dopants may play in this chemistry, even in cases of very high dopant–host compatibility. For other cases with larger dopant–host incompatibilities, such as Mn^{2+} in CdSe or CdS, the inclusion of dopants in the critical nuclei is therefore very unlikely barring exceptional circumstances.

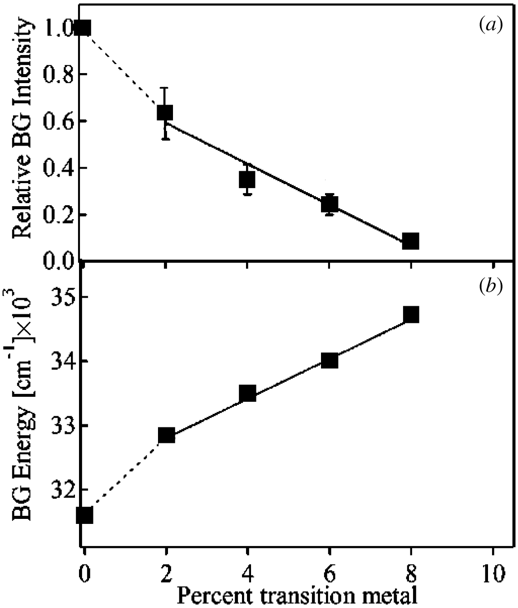

Figure 6. ZnO band-gap (*a*) intensities and (*b*) energies collected during synthesis of Co^{2+}-doped ZnO nanocrystals, plotted versus initial dopant concentration. [Adapted from (52).]

C. Impurities and Nanocrystal Growth

The exclusion of dopants from the critical nuclei does not preclude their statistical incorporation into the nanocrystals during growth, and it is likely that the dimensions of typical semiconductor critical nuclei are sufficiently small that the existence of undoped cores in such nanocrystals is acceptable for all practical purposes. Since the majority of the mass of nanocrystals is not formed during nucleation, we now consider the factors affecting incorporation of dopants during growth from solution. Consider the case of 3*d* TM^{2+} ions doped into CdS or CdSe nanocrystals. Several researchers have found that TM^{2+} ions do not incorporate readily into CdS and CdSe nanocrystals grown under standard conditions at either low or high temperatures (47, 63, 82). Some understanding of this behavior can be obtained by investigating where the dopants do end up. Very few studies of this type have been reported. In one of the earliest studies, electron paramagnetic resonance (EPR) spectroscopy (see Section III.B) was used to evaluate the synthesis of colloidal Mn^{2+}:CdSe nanocrystals made by hot injection (47). Figure 7 shows the EPR spectra of two preparations of Mn^{2+}:CdSe from this work. The top left spectrum shows

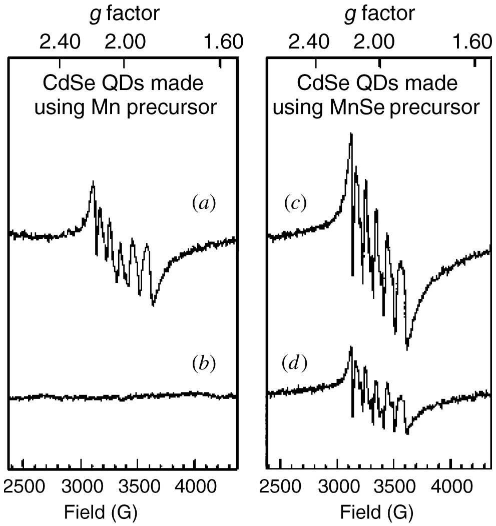

Figure 7. 5 K EPR spectra of 4.0-nm diameter CdSe QDs prepared using ionic Mn^{2+} precursor (*a*, *b*) and $Mn_2(\mu\text{-SeMe})_2(CO)_8$ precursor (*c*, *d*). Before Py exchange, both (*a*) and (*c*) show the Mn^{2+} hyperfine splitting pattern. After pyridine exchange, only samples prepared using $Mn_2(\mu\text{-SeMe})_2$-$(CO)_8$ precursor show Mn^{2+} signal (*b*, *d*). [Adapted from (47).]

the nanocrystals made by injection of a solution of $CdMe_2$ into hot TOPO in the presence of a small quantity of $Mn(CO)_5Me$. Although the characteristic six-line hyperfine spectrum of Mn^{2+} was observed in the product nanocrystals, the bottom left spectrum shows that this EPR signal disappeared entirely after pyridine (Py) ligand exchange (stirring for ~24h total in pyridine, performed in multiple steps), demonstrating that the Mn^{2+} was not within the CdSe nanocrystals. Similar results were also obtained for other manganese precursors such as $MnMe_2$ and tricarbonyl methylcyclopentadienylmanganese. The authors concluded that the Mn^{2+} EPR signal in Fig. 7(*a*) must have originated from loosely bound surface Mn^{2+} or other decomposition products that were not removed by size-selective precipitation, and that Mn^{2+} had not been incorporated within the nanocrystals successfully by this method. In another study, nanocrystalline ZnS and CdS were synthesized in the presence of Eu^{3+} and Tb^{3+} using several synthetic techniques at various temperatures in attempts to incorporate these lanthanides into the semiconductor nanocrystals (83). Although lanthanide emission was observed, luminescence excitation spectra showed only the $4f^n$–$4f^n$ internal transitions of the lanthanide ions, but sensitization by the semiconductor host was absent. From these data, the authors concluded that none of the synthesis techniques employed were able to incorporate lanthanides into the II–VI semiconductor nanocrystals, but only

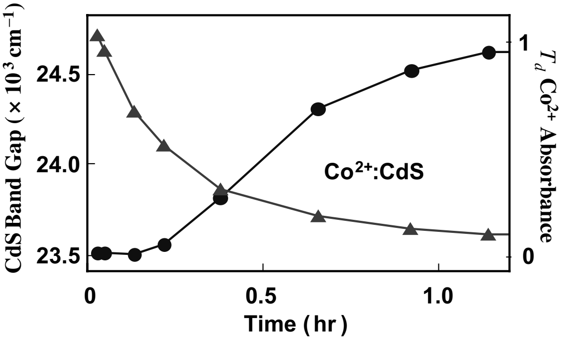

Figure 8. Kinetic evolution of CdS band-gap energy (▲) and Co^{2+} ligand-field absorption intensity (●), collected *in situ* during the synthesis of Co^{2+}:CdS nanocrystals in inverted micelles.

resulted in the lanthanides likely bound to the particle surfaces. This incompatibility was attributed to the charge mismatches and large size differences between the dopants and host cations in these cases.

Dopant incorporation during nanocrystal growth is essentially a kinetics problem. Figure 8 shows electronic absorption data collected *in situ* during the synthesis of CdS nanocrystals in inverted micelles in the presence of Co^{2+} ions (84). The reaction was initiated by addition of excess S^{2-} to the inverted micelle suspension of Cd^{2+} (99%) and Co^{2+} (1%) ions. Through these experiments, nanocrystal growth and dopant incorporation could be monitored simultaneously. The data in Fig. 8 show that during the initial stages of the reaction, nanocrystal growth is relatively rapid and there is no discernible conversion of octahedral solvated Co^{2+}, likely $[Co(H_2O)_6]^{2+}$, to the tetrahedral geometry. This indicates that dopant incorporation is kinetically uncompetitive with nanocrystal growth at early stages of growth, when lattice nutrient is abundant and growth occurs rapidly. Microscopically, this implies that Co^{2+} ions are not competitive with solvated Cd^{2+} ions for open surface coordination sites under S^{2-}-rich conditions. As the reaction progresses, the concentration of solvated Cd^{2+} is diminished and Co^{2+} binding eventually becomes competitive, giving rise to the characteristic tetrahedral Co^{2+} absorption. What results is a gradient of dopant ion concentration throughout the nanocrystal growth layers that is dictated by the kinetic competition between irreversible addition of Cd^{2+} versus Co^{2+} ions to the surfaces of growing CdS nanocrystals. Such a gradient may be generally expected, and will be greatest in cases of large dopant–host incompatibility.

A deeper understanding of the chemistry from Fig. 8 is obtained by closer inspection of the final products. Figure 9(*a*) shows a set of absorption spectra (68) collected on Co^{2+}:CdS QDs prepared by the same inverted micelle method and resuspended in Py. Over time, the Co^{2+} ligand-field absorption intensity

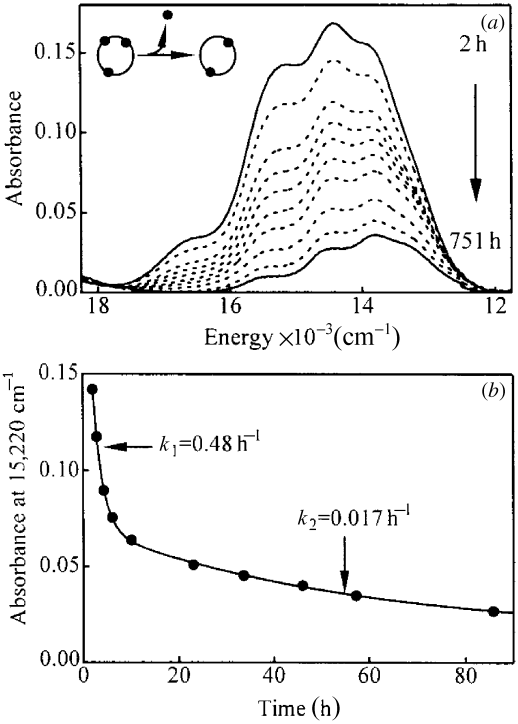

Figure 9. (*a*) Co^{2+} ligand-field absorption spectra for as-prepared Co^{2+}:CdS nanocrystals, collected between 2 and 751 h after suspension in Py. (*b*) Decay of the Co^{2+} ligand-field absorption intensity from (*a*), monitored at 15,220 cm^{-1}. [Adapted from (68).]

decreases, indicating solvation of surface-bound dopants analogous to the scenario observed for Mn^{2+} in Figure 7(*a*). The Co^{2+} ion solvation was exceedingly slow at room temperature, however, with 20% of the dopants remaining after 1 month in pyridine. This slow solvation reflects the thermodynamic stability of Co^{2+} bound to a CdS nanocrystal surface. Inspection of the solvation data revealed biphasic kinetics [Fig. 9(*b*)], and analysis of the deconvoluted absorption spectra led to the conclusion that the two metastable forms were both tetrahedral Co^{2+} ions bound to the surfaces of the QDs, having either one (NS_3) or two (N_2S_2) pyridine ligands as illustrated in Fig. 10(*a*).

The significance of these solvation intermediates lies in their relationship to intermediates along the growth pathway to internally doped nanocrystals, since these data reveal the thermodynamic stability of tetrahedral surface-bound Co^{2+} ions. Binding of impurity ions to nanocrystal surfaces is a necessary step in doping a growing nanocrystal. The absence of a detectable intermediate between

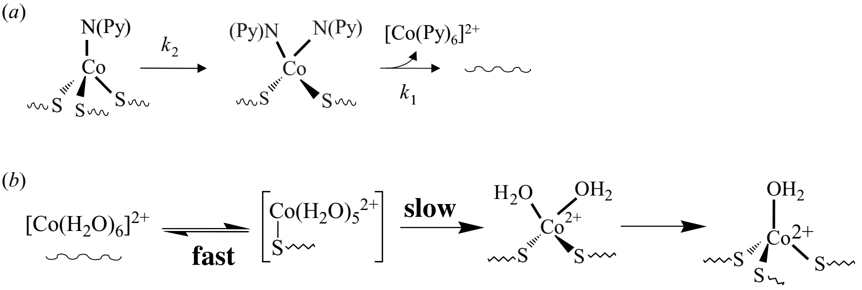

Figure 10. (*a*) Mechanism of solvation of surface bound Co^{2+} ions on CdS by Py, determined from analysis of ligand-field absorption spectra. (*b*) Mechanism of Co^{2+} binding to the surfaces of CdS nanocrystals during aqueous-phase synthesis. [Adapted from (68).]

Co^{2+} with N_2S_2 coordination and solvated Co^{2+} suggests that once the second bond to the surface is replaced by pyridine, cleavage of the last remaining bond to the CdS surface is relatively rapid. This finding is consistent with the large ligand substitution rate constants of Co^{2+} ions. The key to irreversible dopant binding to the surface in this case therefore appears to be the formation of the second Co^{2+}—S^{2-}_{surf} bond. In aqueous reaction solutions, where the reaction proceeds in the opposite direction of the solvation process shown in Fig. 10(*a*), formation of the first Co^{2+}—S^{2-}_{surf} bond is anticipated to be facile and to occur essentially with collisional probability. Once formed, however, this bond is labile and is easily cleaved to return the Co^{2+} ion back to solution. Cleavage of a Co^{2+}—OH_2 bond and formation of the second Co^{2+}—${S^{2-}}_{surf}$ bond must be slow, but strongly favored at equilibrium in the aqueous reaction mixture. Surface binding in H_2O is summarized in Fig. 10(*b*). Co^{2+} binding to the CdS surface is driven in part by the chelating effect of the surface and is evidently thermodynamically favorable in H_2O, but not in Py.

It is not possible to assume for every case that nanocrystal growth will continue and eventually internalize a dopant once it is bound to the nanocrystal surface, however. It is also necessary to consider the influence of that surface-bound dopant on the ability of the lattice to propagate. This topic has been addressed thoroughly in the extensive literature of crystal growth, and the fundamental principles developed there also apply to nanocrystals. For simple crystalline structures and isomorphic substitution, a clear picture of the role of defects emerges, for example, from electron microscopy studies of the growth of $CaCO_3$ crystals in the presence of Mg^{2+} ions (85). In this case, Mg^{2+} binding to a growing surface was found to pin step edges, inhibiting further crystal growth until the activation barrier to complete overgrowth of the defect could be overcome. A similar scenario is expected for most nanocrystal doping experiments, and has been observed experimentally in the case of the Co^{2+}-doped

ZnO nanocrystals described above. Figure 6(*b*) shows a significant decrease of ZnO nanocrystal diameter with increasing concentration of dopants added to the synthesis mixture, manifested as a blue shift in the ZnO band gap (52). Similar inhibition of growth has been observed in doped SnO_2 nanocrystals (58, 60). These data were collected simultaneously with those of Fig. 6(*a*), which showed a concomitant decrease in the number of nucleation events. Thus, despite the greater nutrient/nanocrystal ratios at higher Co^{2+} concentrations, the nanocrystal diameters were reduced. This trend is understood by examining the role of defects in determining the solubility of a nanocrystal. The presence of an impurity ion at or near the surface of a crystal shifts the equilibrium toward solvation by raising the effective specific interfacial energy, precisely as observed in the microscopy studies of Mg^{2+}:$CaCO_3$ step-edge pinning (85). This truncation of nanocrystal growth by impurities is ultimately closely related to the well-known phenomenon of freezing point depression. In general, we may conclude from these studies that the chemistry of the dopants is indeed important, and factors such as ligand substitution rates, ligand-field stabilization energies, and the types of other ligands available under reaction conditions may all contribute to the ultimate success or failure of a synthetic procedure aimed at doping inorganic nanocrystals.

A few methods have been explored for encouraging dopant incorporation during nanocrystal growth, primarily in CdSe doping. In the example of Mn^{2+} doping of CdSe nanocrystals described above (47), the authors attributed the exclusion of Mn^{2+} from their nanocrystals to the form of Mn^{2+} in solution. When the dopant was introduced as the "single-source" monomer $Mn_2(\mu\text{-}SeMe)_2(CO)_8$, successful doping could be demonstrated using EPR spectroscopy by showing that the EPR signal was insensitive to Py ligand exchange [Fig. 7(*c*) and (*d*)]. Wavelength-dispersive X-ray spectroscopy (EDX) showed the dopant concentration to be $<1\%$ in the nanocrystals, or approximately one-half as large as the relative Mn^{2+} concentration of the metal precursor mixture. Furthermore, etching the surfaces of the nanocrystals chemically removed a disproportionate fraction of the Mn^{2+} ions, demonstrating an increased concentration of the dopants at or near the nanocrystal surfaces. These results demonstrate the general propensity for dopants to be excluded from CdSe nanocrystals under high-temperature growth conditions, but also illustrate how the chemistry of the dopant precursor may play a major role in determining the outcome of the synthesis.

The possibility of structural prearrangement of ions to direct the incorporation of dopants into inorganic nanocrystals in an explicit two-step nucleation process is a powerful motivation for exploration of cluster or other "single-source" precursors. Doped CdSe nanocrystals have been prepared (70, 86) using modified "single-source" precursor methods originally developed for synthesizing high-quality CdSe nanocrystals (87–89), in which lyothermal

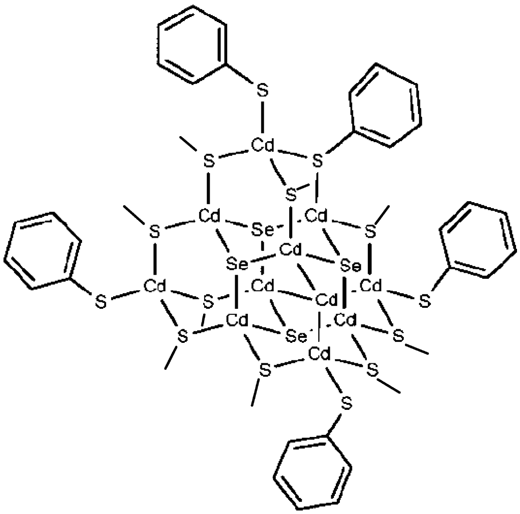

Figure 11. The $[Cd_{10}Se_4(SC_6H_5)_{16}](NMe_4)_4$ cluster precursor used in the synthesis of CdSe and Co^{2+}:CdSe QDs. Note that the thiophenolates have been truncated for clarity, and the molecule contains no sulfides. [Adapted from (89).]

decomposition of monomers such as $\{Cd[S_2CNMe(^nHex)]_2\}$ or clusters such as $[Cd_{10}Se_4(SC_6H_5)_{16}](NMe_4)_4$ (Fig. 11) (89) provide both anion and cation nutrient in a one-pot reaction. In one such study, cobalt ions were introduced using the cluster $[Co_4(SC_6H_5)_{10}](NMe_4)_2$ in the desired stoichiometry and heating this mixture with $[Cd_{10}Se_4(SC_6H_5)_{16}](NMe_4)_4$ to ~200°C in hexadecylamine under N_2 (70). The resulting nanocrystals were stripped three times with Py to remove potential surface cobalt ions prior to physical measurements. On the basis of systematic trends observed in lattice parameters (measured by powder X-ray diffraction, see Section III.A) and lattice vibrational energies (measured by Raman spectroscopy) with stoichiometry of the reaction mixture, the authors concluded that random ion displacement of core Cd^{2+} sites by Co^{2+} ions in the wurtzite CdSe QDs was achieved by this method. Magnetic susceptibility experiments confirmed the presence of Co^{2+} in these nanocrystals (see Section IV.B). Europium-doped CdSe nanocrystals were also prepared by a similar approach (69).

The microscopic steps in the decomposition of these clusters and formation of the doped CdSe lattices were not discussed, but it is apparent that whereas the Cd–Se clusters may remain intact as proposed in an earlier discussion of the same lyothermal synthesis (89), the cobalt clusters must dissociate to liberate Co^{2+} ions for random core doping to occur. When viewed side by side, the structural similarity between the $[Cd_{10}Se_4(SC_6H_5)_{16}](NMe_4)_4$ cluster (Fig. 11) and the basic zinc acetate clusters $[(OAc)_6Zn_4O]$ (Fig. 5) and $[(OAc)_{12}(Zn_{10}O_4)]$ is striking (in fact, all three are examples of fractal Sierpinski tetrahedra), and it is tempting to speculate that a similar dopant-free CdSe nucleation initiates the reaction, with dopant incorporation during growth only. Exploration into the use of heterometallic single-source precursors, such as the hypothetical cluster $[Cd_{10-n}Co_nSe_4(SC_6H_5)_{16}](NMe_4)_4$, would be extremely interesting and should assist in determination of whether or not cluster decomposition occurs prior to nanocrystal nucleation. Nevertheless, the materials made by this cluster approach are among the best characterized colloidal DMS NCs reported to date. Additional results from studies of these NCs are discussed in more detail in Sections III.A and IV.B.

D. Surface-Exposed Dopants

For many years, the paradigm in the study of pure QDs has been size uniformity. For doped QDs, this paradigm is superceded by that of controlled dopant speciation, because without a known and preferably homogeneous dopant speciation it is exceedingly difficult to draw any meaningful conclusions from subsequent physical measurements. Even in the most favorable synthetic scenario, in which dopants are isotropically distributed throughout the nanocrystals, the statistical population of dopants at the nanocrystal surfaces comprises a large percentage of the total dopant population. Surface-bound dopants may have different geometries, electronic structures, or strengths of interaction with the semiconductor than internal dopants, and their presence may obfuscate the origins of the nanocrystals' physical properties or even compromise the desired physical properties (63, 68, 90). Here, we therefore outline the principal methods that have been demonstrated to ensure homogeneous dopant speciation in semiconductor nanocrystals.

The two examples mentioned in Figs. 7 and 9 in which Py was observed to remove dopants from the surfaces of nanocrystals, immediately suggest one possible approach to purification of doped nanocrystals, namely, by using coordinating solvents or ligands as surface cleaning agents. The choice of experimental conditions for this procedure is critical, and some reliable verification of its success is essential because of the wide range of possible dopant solvation rates. As described in Section II.C, stirring in Py for ~24 h completely removed Mn^{2+} ions bound to the surfaces of CdSe QDs (47). In the case where both surface and internal Mn^{2+} ions were formed in the as-prepared nanocrystals, this procedure should result in a product in which the only Mn^{2+} ions remaining are those not exposed to solvent, that is, internal dopants. The relatively short time period required to remove dopants from the QD surfaces makes this approach practical in the case of CdSe QDs. In contrast, as described in Section II.C, the removal of Co^{2+} ions from the surfaces of CdS nanocrystals

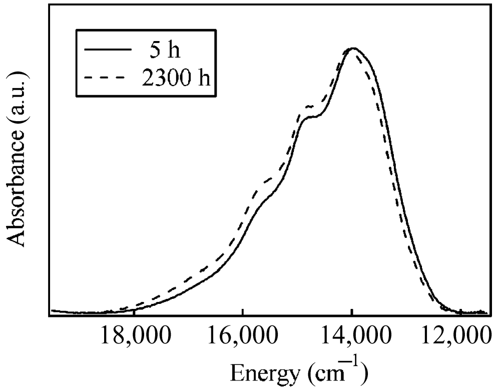

Figure 12. Ligand field absorption spectra of Co^{2+} ions on the surfaces of ZnS QDs, collected 5 h (solid line) and 2300 h (dashed line) after suspension in Py. [Adapted from (91).]

using Py was extremely slow, with biphasic rate constants of $k_1 = 0.48/\text{h}$ and $k_2 = 0.017/\text{h}$ [Fig. 9(*b*)] (68). Because of these small rate constants, the reaction must be allowed to proceed for several weeks before >95% of the surface bound Co^{2+} is removed. These small rate constants make this procedure less attractive for this particular case. The use of Py to clean dopants from ZnS nanocrystal surfaces appears to be even less favorable. After 2300 h of continuous suspension in Py, the concentration of Co^{2+} ions bound to the surfaces of ZnS QDs has not diminished by any appreciable extent (Fig. 12) (91), indicating a very stable surface-bound Co^{2+} species. These comparisons demonstrate that the method of cleaning nanocrystal surfaces by Py exchange is not suitable for all situations, and its success must be carefully verified by some independent method. Several variations of the surface-cleaning-by-solvation approach may be explored, including the use of elevated temperatures (52) or better ligands to accelerate solvation. As such, this flexible approach is generally extremely useful for improving the quality of doped nanocrystals by improving dopant homogeneity.

The solvation of transition metal ions bound to the surfaces of nanocrystals clearly relates to the thermodynamics of their interaction with the surface. It is interesting to note that Mn^{2+} solvation from CdSe nanocrystal surfaces appeared to be complete after a Py ligand-exchange procedure that took ~24 h (47), whereas Co^{2+} on the surfaces of CdS nanocrystals requires weeks to be solvated by Py (68), and Co^{2+} on the surfaces of ZnS nanocrystals was not solvated by Py to any measurable extent (91). The thermodynamic variations thus depend sensitively on the geometries of the surface-binding sites offered to the dopants. For example, the S—S separations of CdS surfaces are apparently too large to stabilize Co^{2+} ions to the same extent as those of ZnS. As discussed in Section II.C, the capacity a surface has to stabilize bound dopants is intimately related to the process of dopant incorporation during nanocrystal growth. It is therefore not surprising to find that TM^{2+} ions are more easily incorporated into ZnS nanocrystals than into CdS nanocrystals grown under parallel conditions (68).

A second method demonstrated to successfully eliminate surface-exposed dopants is the so-called isocrystalline core–shell (ICS) procedure (68, 91). This procedure involves the isolation and purification of as-prepared nanocrystals to remove dopants from the growth solution, followed by solution epitaxial growth of additional layers of the pure host material to overgrow surface-exposed dopants. As shown in Fig. 13, as-prepared Co^{2+}:CdS nanocrystals containing almost exclusively surface-bound dopants could be converted to internally doped nanocrystals by overgrowth of additional CdS shell layers, as verified by ligand-field electronic absorption spectroscopy. As shown in Fig. 14, a similar result was demonstrated for ZnO nanocrystals in which Co^{2+} ions were deliberately bound to the nanocrystal surfaces. These two examples illustrate worst-case scenarios, in which all of the dopants were initially bound to the nanocrystal surfaces, and the results confirm the efficacy of the ICS approach. For these specific cases, the ICS procedure is formally analogous to the well-known δ-doping process employed in vacuum deposition syntheses of

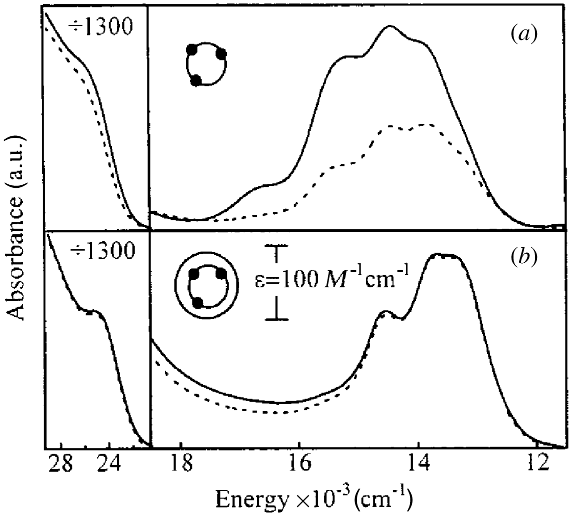

Figure 13. (*a*) 300 K electronic absorption spectra of ~3.0-nm diameter 2.3% Co^{2+}:CdS QDs in Py showing CdS band gap (left panels) and Co^{2+} ligand-field (right panels) absorption. Note the different *x* and *y* axes for the two energy regions. The solid line was collected 2 h and the dashed line 23 h after suspension in Py. (*b*) Absorption spectra (300 K) of 3.7-nm diameter 0.9% Co^{2+}:CdS QDs prepared by the isocrystalline core shell method 2 h (solid) and 28 h (dashed) after synthesis. [Adapted from (68).]

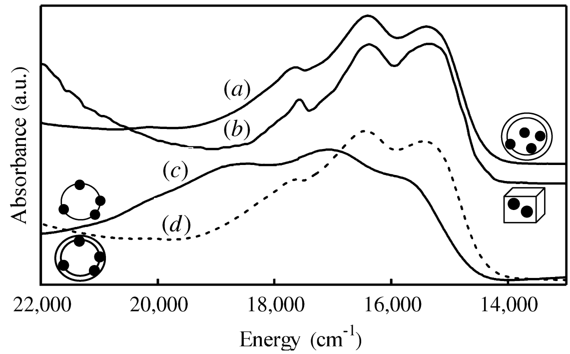

Figure 14. 300 K electronic absorption spectra showing the Co^{2+} $^4A_2 \rightarrow {}^4T_1(P)$ ligand-field absorption of (*a*) isocrystalline core/shell Co^{2+}:ZnO QDs in EtOH, (*b*) bulk Co^{2+}:ZnO single crystal, (92), (c) ZnO QDs in EtOH with Co^{2+} deliberately bound to the surfaces, and (*d*) sample (*c*) following isocrystalline shell growth. [Adapted from (51).]

crystalline thin films. An analogous procedure has also recently been used for the preparation of Ge nanowires incorporating *n*- and *p*-type heteroatoms by vapor deposition methods (93). An attractive feature of these ICS methodologies for nanocrystals is that they allow the preparation of internally doped crystals even in cases where large dopant–host incompatibilities hinder incorporation of dopants into the internal volumes of the nanocrystals under normal growth conditions, as long as the dopants can be bound to the surfaces with sufficient stability to be epitaxially overgrown. This simple and general approach may therefore facilitate the synthesis of a variety of novel and challenging doped nanocrystals.

Core–shell methodologies are particularly important when luminescence is the target physical property of the nanocrystals. Due to the high surface/volume ratios (Fig. 1), nanocrystals typically have a relatively high number of unpassivated surface sites that may act as nonradiative recombination centers or as photoredox centers, thereby reducing the luminescence quantum efficiencies and possibly leading to nanocrystal photodegradation. The most successful remedy of this problem has been surface passivation by growth of a wider bandgap epitaxial shell, typically ZnS grown on CdSe, CdS, or ZnSe nanocrystals (94–100). In doped nanocrystals, the dopants themselves act as nonradiative recombination centers when exposed to the nanocrystal surfaces, and recent studies have found that shell growth may also enhance luminescence from these dopants by surface passivation. The ICS procedure was recently applied to achieve luminescence enhancement in core/shell Mn^{2+}:ZnS/ZnS nanocrystals grown by the same inverted micelle procedure described in the previous paragraph (101). Whereas as-prepared Mn^{2+}:ZnS (<0.25%) nanocrystals showed relatively weak emission from the Mn^{2+} $^4T_1$ excited state, overgrowth of an epitaxial shell layer of ZnS led to an approximate sevenfold enhancement of the emission quantum yield for this transition. Additionally, whereas the as-prepared nanocrystals showed emission quantum yields that were sensitive to UV irradiation at 305 nm, interpreted as passivation of nanocrystal surface defects by undefined photochemical processes, the nanocrystals prepared by the ICS method remained unchanged under similar UV irradiation. A model was developed relating the emission intensities of the as-prepared and ICS nanocrystals to the distribution of dopant ions at the nanocrystal surfaces, and the authors concluded that Mn^{2+} ions were not randomly distributed in the nanocrystals, but preferentially occupied sites close to the NC surfaces. This example provides a clear demonstration that surface-exposed dopants may alter the physical properties of a doped nanocrystal, and illustrates the importance of applying the ICS or other procedures to eliminate such surface exposure.

An interesting approach recently applied to doped nanocrystals is the heterocrystalline core–shell method commonly applied to pure nanocrystals. In a series of papers (102, 103), Mn^{2+}:CdS nanocrystals were synthesized in inverted micelles under conditions very similar to those described above and in Figs. 8, 9, and 13. The poor luminescent properties of the resulting Mn^{2+}:CdS nanocrystals were attributed to nonradiative recombination at unpassivated CdS surface states. From the discussion in Section I and II.C, however, it is likely that a large fraction if not all of the Mn^{2+} ions resided on the surfaces of these as-prepared nanocrystals as observed for Co^{2+} (Fig. 9). This interpretation is supported by studies in other laboratories that showed large Mn^{2+} surface populations in Mn^{2+}:CdS nanocrystals grown by the same inverted micelle approach (63). Nevertheless, growth of a ZnS shell around these Mn^{2+}:CdS nanocrystals led to an approximately ninefold increase in Mn^{2+} $^4T_1 \rightarrow {}^6A_1$ photoluminescence quantum yield and a concomitant decrease in CdS surface state emission (102, 103). A final Mn^{2+} photoluminescence quantum efficiency of >28% was concluded for these core–shell nanocrystals with CdS excitation (103). The changes associated with shell growth were attributed to surface defect passivation, but they very likely arise in large part from the internalization of Mn^{2+} dopants residing on the surfaces of the as-prepared CdS nanocrystals, as observed for Co^{2+}:CdS nanocrystals (68) (Section II.C). The resulting material may in fact have the interesting structure in which all Mn^{2+} dopant ions are located at the CdS–ZnS interface or in the ZnS shell, but are still sensitized by the CdS core QD. The improved luminescence quantum yields of these Mn^{2+}-doped nanocrystals made them valuable for application in hybrid organic–inorganic multilayer electroluminescence devices prepared by spin-coat processing (104) (see Section V.A).

III. ANALYTICAL PROBES OF DOPING

As illustrated in the above examples, the physical properties of doped nanocrystals are very strongly linked to the dopant speciation. Nanocrystals with impurities randomly substituted throughout the lattice will generally behave differently from those in which the impurities are segregated to the surfaces. This raises the important question: What methods should be used to judge the success of a synthetic procedure before moving on to study physical properties? The field has not yet reached a consensus on what the criteria should be for proving successful doping, nor is it likely that any one method will be satisfactory for all cases. A survey of the literature reveals that data from a variety of physical methods have been presented as evidence of doping. In this section, we present an overview of the most common methods that have been applied for the purposes of characterizing the doping of semiconductor nanocrystals.

A. X-Ray Diffraction and Raman Spectroscopy

Doping a crystal with impurities does not result in the appearance of new X-ray diffraction peaks, but instead leads to gradual shifts in the lattice parameters of the host material as the dopant concentration is increased from the dilute limit. The shifts arise from the strain induced when the dopant is incorporated into the periodic crystal lattice. In what is now known as Vegard's law (75), the average lattice parameter should vary linearly with dopant concentration in the crystal, and deviations from linearity are indications of phase transitions or segregation. For bulk semiconductor crystals, Vegard's law is an invaluable tool for studying doping (20), and shifts in X-ray diffraction peaks have recently been used as supporting evidence for the conclusion of isotropic doping in inorganic nanocrystals by several groups (69, 70, 105). The powder X-ray diffraction data in Fig. 15, for example, show a linear decrease in the a and c lattice parameters of wurtzite CdSe nanocrystals with increasing analytical Co^{2+} content up to 17% Co^{2+} (70). A discontinuity in the lattice parameter shift was observed only between 17 and 30%, suggesting the possibility of a phase transition or segregation at this highest concentration. From these data, random ion displacement of core Cd^{2+} sites by Co^{2+} ions in the CdSe QDs was concluded for the lower concentrations, in agreement with Vegard's law.

For nanocrystals, the interpretation of lattice parameter shifts is complicated by the very small dimensions of the crystallites. Because of the small crystal dimensions, the diffraction peaks are broadened as described by the Debye–Scherrer equation (106), making accurate assessment of small shifts more challenging. Systematic errors such as zero-point or sample-height offsets can also cause artificial shifts in lattice constants (107). The inclusion of an internal

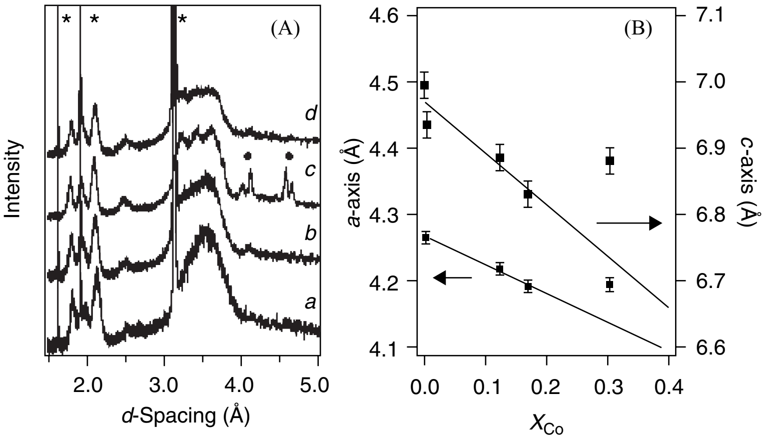

Figure 15. (A) X-ray powder diffraction of Co^{2+}:CdSe nanocrystals: (*a*) 0.4, (*b*) 12, (*c*) 17, and (*d*) 30% Co^{2+}. Silicon reference (*) and hexadecylamine (•) peaks are also observed. (B) shift of *a* and *c* unit cell dimensions as a function of Co^{2+} concentration. Lines represent least-squares fits to the data <30% Co^{2+}. [Adapted from (70).]

standard such as bulk silicon can be used to account for such artifacts and is essential for any quantitative analysis of the unit cell parameters. Although commonly used in the characterization of bulk phase materials, this procedure is infrequently employed in studies of doped nanocrystals.

Fully miscible solid solutions such as $Zn_xCd_{1-x}S$ $(0 < x < 1)$ offer the best-case scenario in which to study lattice constant shifts in doped nanocrystals. Figure 16 shows the lattice constant shifts measured for a series of nanocrystalline and bulk $Zn_xCd_{1-x}S$ alloys. Two features of the data are noteworthy: (1) Nearly identical slopes (differing by ~4%) are measured for both data sets, and (2) A significant offset (~0.03 Å) between the data sets is measured. The nearly identical slopes confirm the validity of a Vegard's law analysis of the nanocrystal data. The offset raises the possibility of an experimental determinate error or nanoparticle surface effects that may change the apparent lattice parameter. Although the offset may at first appear negligible, its magnitude is ~15% as large as the total lattice parameter shift over the entire doping range, a range that is much larger than those obtained for less miscible systems such as $Zn_{1-x}Mn_xSe$(20) or $Zn_{1-x}Ni_xO$ (109).

Perhaps of greater concern than calibration may be the increased sensitivity to surfaces in powder XRD of nanocrystals relative to macroscopic crystalline materials. Although XRD is routinely described as a bulk technique, it is important to recognize that the nanocrystals themselves are up to 30% surfaces, making the XRD experiment of nanocrystals more sensitive to surface effects

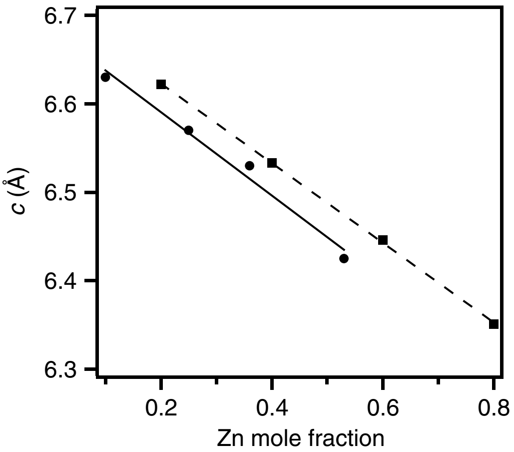

Figure 16. The *c*-axis lattice parameter for nanocrystalline (●) and bulk (■) $Cd_xZn_{1-x}S$. Nanocrystalline and bulk data were adapted from (105) and (108), respectively.

than the same experiment performed on the corresponding bulk material. Although the data in Fig. 15 are consistent with the conclusion of random substitutional doping in the Co^{2+}:CdSe nanocrystals, it is worthwhile considering whether the data would also be consistent with other interpretations, such as that the dopants are all on the nanocrystal surfaces. What should be observed in the X-ray diffraction data in this hypothetical scenario?

Several groups have used XRD or wide-angle X-ray scattering (WAXS) to study the growth of heterocrystalline shells around semiconductor QDs, primarily for the purposes of enhancing luminescence quantum yields by surface passivation (95, 97–100). Figure 17 shows diffraction patterns for ~4.0 nm diameter CdSe nanocrystals overcoated with (panel A) ZnS (95) or (panel B) CdS (100) shells of different thicknesses. In both cases, as the surface shell thicknesses are increased, gradual shifts to higher angles of all diffraction peaks are observed. At 2.6 monolayers coverage in the CdSe/ZnS nanocrystals, a new feature at 56° becomes evident in the CdSe/ZnS core structure, as does identifiable ZnS structure at other diffraction angles. Not until ~5.3 monolayers have been added are new features clearly observed that would suggest the presence of a secondary phase, ZnS. These data were interpreted by the authors as indicative of epitaxial growth of ZnS on the CdSe surfaces up to about two monolayers, either coherently with large strain or incoherently with dislocations (95). Coherent epitaxial growth is suggested by the observation of continuous lattice planes extending across entire surfaces of the core–shell nanocrystals in TEM measurements. Once the thickness of the ZnS shell was increased to above

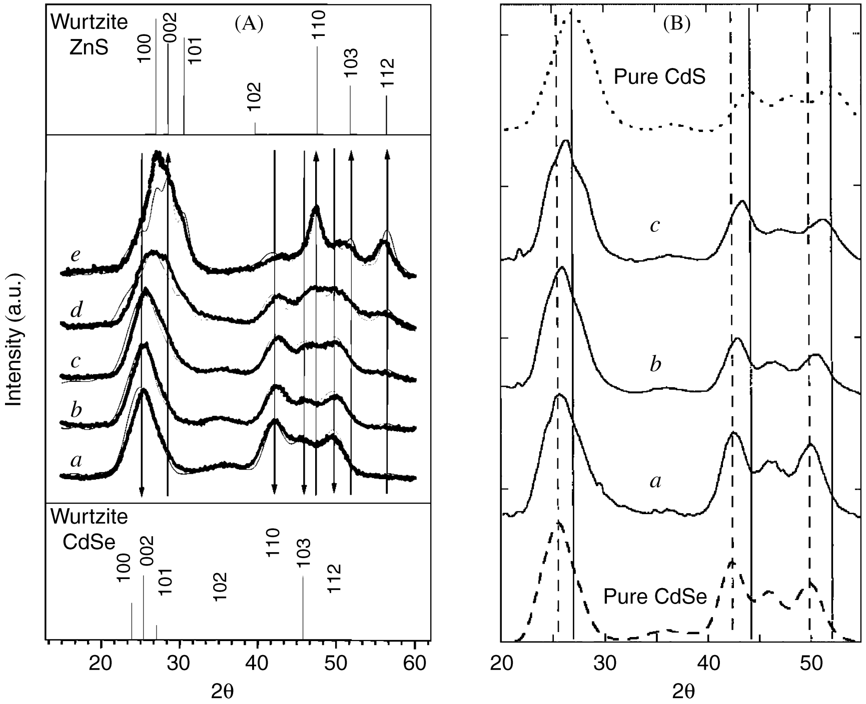

Figure 17 X-ray powder diffraction patterns for core–shell nanocrystals. In panel (A) 4.0 nm diameter CdSe QDs overcoated with (*a*) 0, (*b*) 0.65, (*c*) 1.3, (*d*) 2.6, and (*e*) 5.3 monolayers of ZnS shell. The thin solid lines show simulations of the data. Powder patterns for wurtzite CdSe and ZnS are included for comparison in the botton and top insets, respectively. [Adapted from (95).] (B) 3.5 nm diameter pure CdS nanocrystals (dotted), 3.9 nm diameter CdSe nanocrystals (dashed), and core–shell samples having the same 3.9 nm CdSe core and CdS shell thicknesses of (*a*) 0.2 nm, (*b*) 0.7 nm, and (*c*) 1.1 nm. The dashed vertical lines represent peak positions for pure CdSe; the solid lines represent pure CdS. [Adapted from (100).]

about two monolayers, the strain in the epitaxial ZnS layer arising from its 12% lattice mismatch with the CdSe core caused defects that allowed strain relaxation and ultimately resulted in incoherent growth. For the CdSe/CdS nanocrystals, only a continuous shift toward the diffraction angles of CdS was observed with increasing shell thickness (100).

A similar result has been found using Raman spectroscopy of core–shell nanocrystals. Like XRD, Raman spectroscopy has also been widely employed to study doping of bulk semiconductors (110–112) but so far has only rarely been applied to doped semiconductor nanocrystals (70). Analogous to Vegard's law, shifts in lattice Raman vibrational energies have been found to occur with increasing dopant concentration in both the bulk and nanocrystalline materials.

A Raman study of CdSe/ZnS core–shell nanocrystals (97) also found a 1.9-cm^{-1} blue-shift of the LO band with 0.5 monolayer ZnS shell growth, however, and continuous gradual shifts in the phonon energies were observed up to the equivalent of nearly three full monolayers before new features associated with the ZnS shell were clearly detected. For calibration, 1.3 monolayers of ZnS around a 4.0-nm nanocrystal of CdSe would yield an analytical Zn^{2+} concentration of 43% $^{+}$ ($\sim$1200 atoms in the core, $\sim$900 atoms in the shell), a value that would be at the very high end of a TM^{2+} doping experiment. For more typical doping concentrations of $<$10%, surface segregation of the dopant would not give rise to a new phase, but may lead to a small shift in apparent lattice parameters or vibrational energies if the dopants are ordered epitaxially on the nanocrystal surfaces. Clearly, although linear shifts in apparent lattice parameters and vibrational energies are consistent with substitutional doping in semiconductor nanocrystals , they may also be consistent with epitaxial growth of islands or even whole monolayers of segregated phases on the surfaces of the nanocrystals, and such data for nanocrystals must therefore be interpreted with caution. The fact that X-ray diffraction, Raman spectroscopy, or other traditional probes of doping may be strongly influenced by changes in surface structure when applied to materials that are $\sim$25% surface highlights one of the new challenges faced when working with this new class of materials.

B. Electron Paramagnetic Resonance Spectroscopy

Electron paramagnetic resonance spectroscopy is an accessible dopant-specific spectroscopic technique that probes transitions within Zeeman-split ground states of paramagnetic ions. For the usual transverse experimental configuration, the microwave absorption selection rule is $\Delta M_J = \pm 1$. Because of zero-field splittings, transverse EPR is sensitive almost exclusively to ions with Kramers ground states, such as Mn^{2+}. As described in Section II.C, EPR spectroscopy has proven to be a very useful method for evaluating success in the synthesis of colloidal Mn^{2+}-doped semiconductor nanocrystals. The EPR spectra of a large number of nanocrystals doped with Mn^{2+} have now been reported. Despite its superb sensitivity to Mn^{2+} ions, this technique has not been widely employed for mechanistic studies in this area.

The sensitivity of EPR to multiple coordination environments has been demonstrated in studies of Mn^{2+}-doped CdS nanocrystals (63). In Mn^{2+}:CdS nanocrystalline powders prepared by inverted micelle synthesis, four distinct resonances were observed and deconvoluted by varying experimental parameters including microwave power, microwave frequency, and temperature. The deconvoluted signals are shown in Fig. 18. Four distinct manganese species were detected through this experiment. A six line spectrum characteristic of isolated paramagnetic Mn^{2+} was observed at 300 K and below [multiline

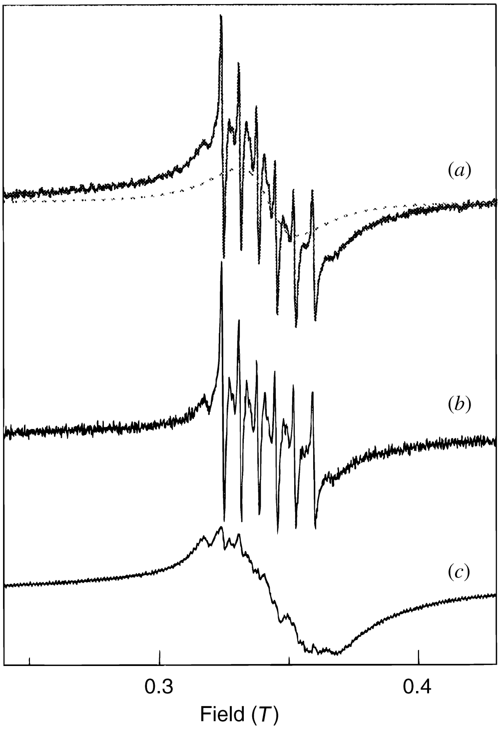

Figure 18. X-band EPR spectra of Mn^{2+}:CdS NCs recorded at (*a*) 300 K and 25-mW power, (*b*) 4.2 K and 0.25-mW power, and (*c*) 4.2 K and 250-mW power. The dashed line in (*a*) was obtained by subtracting signal (*b*) from signal (*a*). [Adapted from (63).]

signal (*b*)]. A broad, slightly asymmetric signal [signal (*c*)] observed only at 4.2 K could be cleanly recorded by using microwave powers high enough to saturate the first signal [signal (*b*)] at 4.2 K. This broad signal was attributed to tetrahedrally coordinated Mn^{2+} in a disordered host, likely in a coordination environment "near the surface" of the nanocrystals. An intense, broad Lorentzian signal was also observed [signal (*a*, dashed)] that increased in intensity with Mn^{2+} concentration and disappeared <4.2 K. This spectrum could be obtained cleanly by subtracting the multiline signal [signal (*b*)] from the full spectrum [signal (*a*, solid)] collected at 300 K. This temperature dependence is suggestive of antiferromagnetism, and signal (*a*, dashed) was attributed to phase segregated MnS. Finally, an additional weak signal was observed using Q-band microwave frequency (not shown) and attributed to octahedral surface-bound Mn^{2+} ions. The deconvolution of these four signals by use of different microwave powers and frequencies, and different temperatures, allowed the authors to demonstrate a heterogenous distribution of Mn^{2+} dopants in the

Mn^{2+}:CdS nanocrystals prepared by this method. A similar approach has been applied to colloidal Mn^{2+} -doped ZnSe nanocrystals (90) prepared via a single-source precursor method (Section II.A), which showed evidence for both a disordered surface-bound or near-surface Mn^{2+} and an internal substitutional Mn^{2+}. In both of these studies, this information was then applied in the analysis of energy-transfer processes involving the near-surface Mn^{2+} ions.

The information provided by EPR spectroscopy related to the synthesis of Mn^{2+}-doped ZnO nanocrystals is found in the data of Fig. 19 (54). The 300 K X-band EPR data in Fig. 19, panel A follow the progress of a sample from an early stage of growth through a surface cleaning process designed to ensure exclusively internal doping of the resulting nanocrystals. Spectrum (*a*) provides a reference for the spectrum of surface-bound Mn^{2+} ions, which were deliberately bound to the surfaces of pure ZnO nanocrystals in this case. The breadth of the features in spectrum (*a*) is attributed to the inhomogeneous Mn^{2+} speciation on the nanocrystal surfaces. Spectra (*b*) and (*c*) provide snapshots of the Mn^{2+} at different stages during growth. Spectrum (*b*) was collected shortly (~10 min) after addition of OH^- to initiate nucleation and growth. The spectrum represents the sample after it has reached its metastable state and no longer exhibits

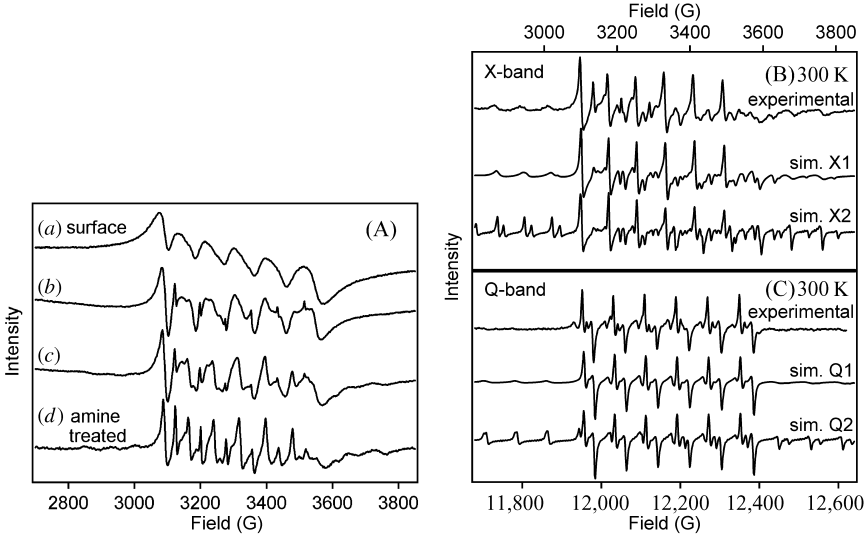

Figure 19. Panel A is the X-band EPR spectra of colloidal Mn^{2+}:ZnO nanocrystals. (*a*) Surface-bound Mn^{2+}:ZnO nanocrystals. Samples prepared from 0.02% Mn^{2+}/99.98% Zn^{2+} reaction solution collected (*b*) 10 min after base addition, (*c*) after 2 h of heating at 60°C, and (*d*) after treating with dodecylamine. Panels B and C are the experimental and simulated 300 K X- and Q-band EPR spectra of colloidal dodecylamine-capped 0.02% Mn^{2+}:ZnO nanocrystals in toluene. Simulations with (X1 and Q1) and without (X2 and Q2) $\sigma = 2\%$ D-strain are included. [Adapted from (54).]

diffusion limited growth. Spectrum (*b*) generally resembles spectrum (*a*), but shows improved resolution of the fine structure. The emergence of resolved hyperfine structure in this spectrum is attributed to partial incorporation of Mn^{2+} into the ZnO lattice. At an average nanocrystal diameter of ~4.0 nm, even a statistical distribution of the dopants will result in a high proportion (~25%) of the Mn^{2+} ions at the surfaces of the nanocrystals. Spectrum (*c*) was collected after heating the same sample to 60°C for 2 h to accelerate Ostwald ripening. As seen from these data, the Mn^{2+} hyperfine features become increasingly better resolved as growth proceeds, reflecting increased homogeneity in the Mn^{2+} speciation. The increased homogeneity qualitatively follows the decrease in the surface/volume ratio upon increasing the crystal diameters from 4.0 to 5.6 nm. Spectrum (*d*) was collected following stripping of surface-bound Mn^{2+} ions off of the nanocrystal surfaces using dodecylamine. The resulting spectrum shows a series of well-resolved hyperfine transitions that could be simulated using axial zero-field splitting (termed D) and *g* values essentially identical to those of the bulk single crystal, except for the addition of $\sigma = \pm 2\%$ D strain in the nanocrystal simulations (Fig. 19, panels B and C). These data not only demonstrate successful doping of the ZnO nanocrystals with Mn^{2+}, but the increasingly well-resolved hyperfine patterns with decreasing surface/volume ratios reveal incorporation of the dopants during growth, and consequently, a distribution of dopants throughout the nanocrystal lattices. The D strain in the nanocrystals was attributed to minor lattice relaxation effects not present in the bulk single crystal and associated with the proximity of surfaces in these small crystallites.

EPR spectroscopy is not limited to Mn^{2+}, but the slow relaxation rates of Mn^{2+} make this ion particularly well suited for EPR studies. The difference between EPR signals for surface-bound and substitutionally doped Mn^{2+} ions is generally very small, however, in part because of the large energetic separation between the ground and first excited states of Mn^{2+} (~18,000 cm^{-1} in II–VI lattices), which leads to small second-order spin–orbit (or zero-field) splittings of the $^6A_1$ ground state. These factors in turn mean that Mn^{2+} continuous wave (CW) EPR spectra lack detailed information about the Mn^{2+} ligand-field environments. This situation is different for other potential dopants such as Co^{2+}, but the EPR spectroscopy of these dopants in semiconductor nanocrystals has not yet been sufficiently explored.

C. Electronic Absorption Spectroscopy

Electronic absorption spectroscopy has played a pivotal role in the development of methods for synthesizing pure semiconductor nanocrystals. Nanocrystal sizes, size distributions, growth kinetics, growth mechanisms, and electronic structures have all been studied in detail using electronic absorption spectroscopy.

The electronic absorption spectra of doped nanocrystals contain considerably more features than those of the pure host nanocrystals. The transitions observed may be grouped into three general classes: (*a*) the valence–conduction band transitions of the semiconductor itself, (*b*) the internal (ligand field, or *d–d*) transitions of the dopant ions in the lattice environment, and (*c*) charge-transfer transitions involving either promotion of dopant electrons into the conduction band or promotion of valence band electrons into a dopant-localized orbital. Each transition type contains information about the electronic structure of the doped nanocrystal. As discussed in Section II.B, the ligand-field transitions are particularly valuable from a synthetic point of view because they are sensitive to the local coordination environment of the dopant ion and may therefore be used to gain microsopic insight into a synthesis.

The first demonstration of the use of ligand-field absorption spectroscopy to probe doping of QDs was for Co^{2+} doping of CdS and ZnS nanocrystals (68). The Co^{2+} ion has seven *d*-electrons that, in a tetrahedral geometry, give rise to a $^4A_2$ ground state and three quartet excited states whose energies depend on the strengths and types of metal–ligand bonding interactions as described by ligand-field theory. The Tanabe–Sugano diagram for tetrahedral Co^{2+} [Fig. 20(*a*)] shows the energies of the first three spin-allowed ligand-field excitations. The energies of these transitions depend on the ligand-field strength (*Dq*) and electron–electron repulsion parameters, and therefore allow distinction between different coordination environments of the dopant ions. This difference was used to evaluate the success of the inverted micelle approach for the synthesis of

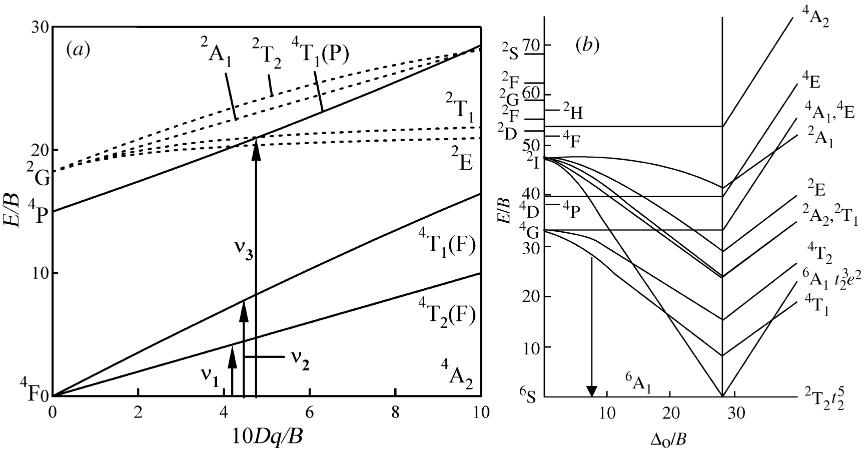

Figure 20. Tanabe–Sugano diagrams for (*a*) tetrahedral Co^{2+} (d^7), showing the energies of the first three spin-allowed ligand-field excitations (ν_1, ν_2, ν_3), and (*b*) tetrahedral Mn^{2+} (d^5), showing the spin-forbidden emissive transition.

Co^{2+} doped CdS and ZnS nanocrystals (68, 91), as described in Section II.D, and to evaluate the incorporation of Co^{2+} ions in the nucleation and growth of ZnO nanocrystals (51, 52), described in Section II.B. The main challenge with application of this method is the low intensities of the *d–d* transitions, which are electric dipole forbidden to first order by the parity selection rule, but which gain intensity by mixing of the *d* orbitals with ligand orbitals and metal *p* orbitals. Intensities are particularly problematic in the special case of Mn^{2+}, which has no spin-allowed excitations because of its half-filled ground-state configuration, which gives rise to a $^6A_1$ ground term having no orbital angular momentum. The ligand-field terms of Mn^{2+} are shown in Fig. 20(*b*), plotted as a function of Dq/B. As discussed in Section III.F, the large energy gap between the $^4T_1$ excited and $^6A_1$ ground states favors luminescence from this excited state [represented as a down arrow in Fig. 20(*b*)], and the luminescence of Mn^{2+} ions doped into semiconductors has been studied extensively.

D. X-Ray Photoelectron Spectroscopy

X-ray photoelectron spectroscopy (XPS) is widely used to characterize thin films grown by vacuum deposition techniques, but relatively few studies of freestanding nanocrystals by XPS have been reported and even fewer studies have been reported that focus specifically on analysis of dopant concentration or speciation by this technique. Due to the short mean free path (escape depth) of the emitted photoelectron, XPS is primarily a surface technique and would therefore seem appropriate for systems with high surface/volume ratios such as nanocrystals. Using peak intensities and atom-specific sensitivity factors [see Ref. (113)], materials composition can be probed by XPS. This approach generally assumes the presence of geometric factors that are not present in nanocrystals because of their small dimensions. A rigorous mathematical treatment for nanocrystals allowed XPS data collected for undoped CdSe nanocrystals to be analyzed to determine quantitative Cd/Se ratios and the percentage of surface coverage by the passivating ligand trioctylphosphine oxide (TOPO) (114). This spectroscopy was also used to characterize the oxidation chemistry of CdSe QDs by monitoring the appearance of a peak in the Se 3*d* core region associated with SeO_2. Several reports on core–shell QDs have included XPS characterization (102, 115, 116).

X-ray photoelectron spectroscopy has been applied as a valence state probe in the study of europium-doped CdSe NCs prepared by lyothermal methods using $Li_4[Cd_{10}Se_4(SC_6H_5)_{16}]$ as the cluster precursor and $EuCl_2$ as the source of europium (69). Lattice contraction with increased dopant concentration (6% contraction in the *a* lattice parameter at 37.4% europium) was observed by XRD and, in accordance with Vegard's law (75), was used to argue random substitutional doping. Interestingly, the europium $3d_{5/2}$ and $3d_{3/2}$ XPS lines were

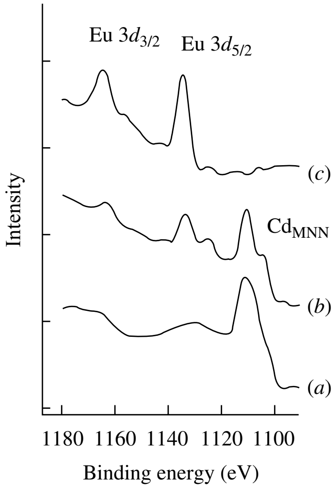

Figure 21. The XPS spectrum of (*a*) CdSe, (*b*) CdEu$_{0.374}$Se, and (*c*) Eu$_2$O$_3$, showing Eu 3*d* core and Cd$_{\mathrm{MNN}}$ Auger lines. [Adapted from (69).]

observed at energies similar to those of Eu^{3+} in Eu$_2$O$_3$ (Fig. 21), leading to the conclusion that the dopants were in the Eu^{3+} oxidation state, although introduced as Eu^{2+}. This conclusion was strongly supported by L-edge X-ray absorption spectroscopy, which showed the europium L$_{\mathrm{III}}$-edge $(2p_{3/2} \rightarrow 5d)$ transitions in both the nanocrystals and Eu$_2$O$_3$ (Eu^{3+}) occurring 7 eV higher in energy than in the Eu^{2+} reference compound, EuS (Fig. 21). Assuming the conclusion of random substitutional doping is correct, the remarkably high Eu^{3+} doping levels of up to 37.4% imply substantial charge imbalance in these nanocrystals, and this must presumably find compensation distally at the nanocrystal surfaces (but see Section III.A concerning Vegard's law).

X-ray photoelectron spectroscopy was also used to study antimony-doped SnO$_2$ nanocrystals prepared as colloids by a sol–gel method involving autoclaving at 270°C (59, 60). Taking advantage of the relationship between escape depth and incident photon energy, in which higher energy photons probe deeper into the nanocrystal, and using a synchrotron radiation source, variable-energy XPS experiments were performed that allowed depth profiling of the Sb^{3+} and Sb^{5+} concentration gradients in $\sim$17% Sb-doped SnO$_2$ nanocrystals (61). For both Sb^{3+} and Sb^{5+}, substantial variation in concentration was observed throughout the nanocrystals (Fig. 22). For $\sim$6.0-nm diameter nanocrystals with average concentrations of $\sim$17%, the effective local concentrations increased continuously from $<$5% in the nanocrystal cores ($<$1-nm diameter) to as high as 27% in the outermost layers of SnO$_2$. This substantial gradient

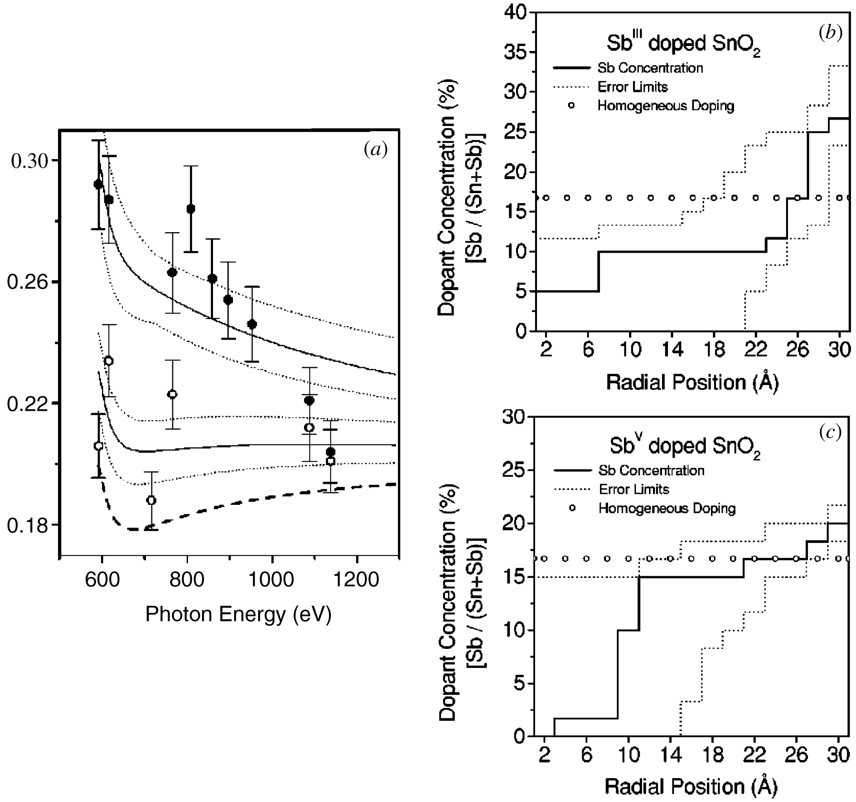

Figure 22. Variable-energy XPS data for Sb-doped SnO_2 nanocrystals. (*a*) Ratio of Sb(III) $3d_{3/2}$ (●) and Sb(V) $3d_{5/2}$ (○) to Sn $3d_{3/2}$ versus photon energy. Solid lines are simulations, dotted lines are estimated error limits, and the dashed line represents the data predicted for the limit of isotropic doping. (*b*) Sb(III) radial distribution profile. (*c*) Sb(V) radial distribution profile. [Adapted from (61).]

suggests nucleation of pure SnO_2 followed by dopant incorporation during growth, as discussed above for doped ZnO and CdS nanocrystals (Sections II.B and C).

E. Extended X-Ray Absorption Fine Structure

Extended X-ray absorption fine structure (EXAFS) data collected at the dopant *K*-shell X-ray absorption edge have been used in some cases as a dopant-specific structural probe, providing very accurate bond lengths and approximate coordination numbers. Whereas X-ray diffraction is rather insensitive to phase segregation at the small doping levels commonly investigated, EXAFS selectively probes the local coordination environment around the nucleus absorbing at the wavelength of irradiation, making it suitable for dopant-specific structural analysis even at low doping levels. This advantage is counterbalanced by the expense and inconvenience of the experiment, which is typically performed at a synchrotron or similar light source. The reader is referred to topical reviews of the EXAFS methodology for further general details.

Several EXAFS studies of doped semiconductor NCs have appeared in the recent literature (58, 69, 90, 117–119). Figure 23 shows the Fourier transform (FT) functions of Mn K-edge (~6.5 keV) data for two nanocrystalline and one bulk Mn^{2+}-doped ZnS samples (118). The scattering peak near 2 Å is attributed to the first coordination shell around the Mn^{2+} ions, namely, the nearest-neighbor S^{2-} ions. The second peak, centered at 3.7 Å, is attributed to the second coordination shell, namely, the next-nearest-neighbor Zn^{2+} and S^{2-} ions. A small shift was observed in the first coordination shell scattering peak when comparing the nanocrystals to the bulk material, and this shift was analyzed to conclude that a difference exists between the Mn—S bond lengths in the nanocrystals and in the bulk material. From a quantitative analysis of background-corrected data in momentum space, the Mn—S bond lengths in the NCs were determined to be 2.39 ± 0.01 Å and 2.36 ± 0.01 Å for the ~5.25 and ~3.25-nm diameter NCs, respectively, and 2.42 ± 0.01 Å in bulk Mn^{2+}:ZnS, all slightly larger than the Zn—S bond lengths of bulk ZnS (2.34 Å). The authors thus concluded that the Mn—S bond length shows a size dependence in nanocrystals of Mn^{2+}:ZnS. This conclusion is important, since it would imply

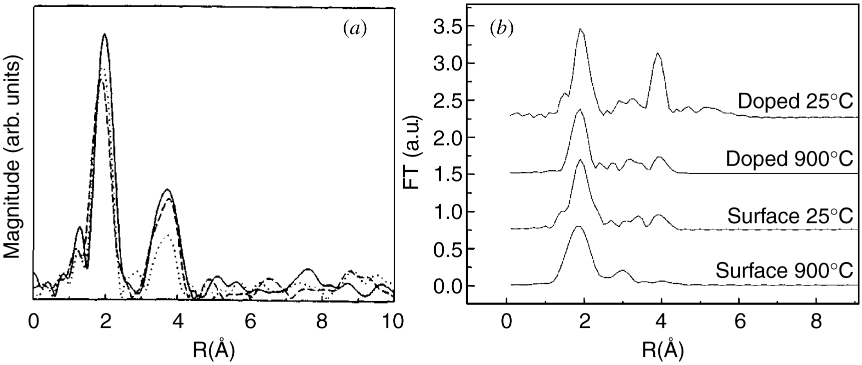

Figure 23. (*a*) Fourier transforms of the EXAFS data for bulk Mn^{2+}:ZnS (solid line), ~5.25-nm diameter 0.5% Mn^{2+}:ZnS nanocrystals (dashed line), and ~3.25-nm diameter 0.5% Mn^{2+}:ZnS nanocrystals (dotted line). [Adapted from (118).] (*b*) Fourier transforms of bulk and surface Cu^{2+}-doped SnO_2 nanocrystals heated for 1 h at high temperatures. The sample type and heating temperatures are listed beside each plot. For clarity the plots have been shifted by 0.75 on the *y* axis. [Adapted from (58).]

that the Mn—S covalency (proportional to orbital overlap) also changes as a function of nanocrystal size in this size regime. No attempts were made to remove dopant ions from the surfaces of these nanocrystals, however, so the presence of substantial surface Mn^{2+} must be borne in mind when evaluating these data. Because ~34% of the cation sites would be in the outermost shell of a 3.25-nm diameter ZnS NC, it is possible that the size dependence of the scattering could instead arise from the increasing proportion of Mn^{2+} ions at the surfaces as the crystal diameters were reduced. Despite the low dopant concentration, the small scattering peak that shows up between the first and second coordination shells in the 3.25-nm diameter ZnS NCs was interpreted as evidence for the presence of Mn^{2+} dimers and trimers in these nanocrystals. Explicit consideration of surface bound Mn^{2+} ions in the EXAFS analysis has been carried out on Mn^{2+} -doped ZnSe nanocrystals (90). The best fits included contributions from both Mn—Se (internal) and Mn—O or Mn—N (surface) Mn^{2+} species. These data demonstrate the remarkable sensitivity of the EXAFS experiment to small concentrations of impurity ions, and the usefulness of this technique as a powerful dopant-selective structural probe.

In a related study (120), Mn^{2+}:CdS nanocrystals from 1.8 to 4 nm in diameter were prepared by the inverted micelle approach with dopant concentrations ranging from 5 to 20%, and the products were studied by EXAFS to characterize the Mn^{2+} coordination environments. Data analysis yielded Mn—S bond lengths (2.38 Å) that were significantly shorter than the Cd—S bond lengths in pure CdS, as expected for the introduction of a smaller ion, Mn^{2+} (0.80 Å), into a Cd^{2+} (0.92 Å) site. To model the data, the authors found it necessary to include a significant (15%) nonsubstitutional scattering contribution, which was attributed to surface-bound Mn^{2+} ions having 2.6 Å Mn^{2+}-thiodecane bonds. The authors also addressed the possibility of Mn^{2+} clustering by EXAFS to demonstrate the existence of a statistical solid solution. In one nanocrystal sample, the Mn^{2+} concentration was determined by Energy Dispersive Spectroscopy (EDS) to be 10%. The EXAFS data for this sample were then analyzed to determine the effective number of Cd^{2+} and Mn^{2+} nearest-neighbor interactions. Analysis of the EXAFS data yielded an average of 10.5 Cd^{2+} nearest neighbors and 1.8 Mn^{2+} nearest neighbors for each Mn^{2+}, or an effective concentration of 15% Mn^{2+}:CdS. The difference between the concentrations determined by EDS and by EXAFS was attributed to uncertainties in the fitting and energy resolution of the EXAFS technique. From Eq. 3, the average nearest-neighbor cationic shell in 10% Mn^{2+}:CdS contains $N = 1.2$ Mn^{2+} ions, and consequently $N = 10.8$ Cd^{2+} ions, consistent with the result obtained from the EXAFS analysis. These analyses support the conclusion that the Mn^{2+}:CdS nanocrystals were true solid solutions with nearly statistical dopant distributions.

Although this chapter focuses mainly on colloidal doped semiconductors, it is of interest to discuss briefly the use of EXAFS to monitor thermally induced dopant segregation in nanocrystalline TiO_2 and SnO_2 powders (58, 119). In these studies, dopants were found to segregate from the internal volume of the crystallites to the grain boundaries between adjacent nanocrystals. These findings are of general importance and are relevant to the colloidal nanocrystals emphasized here since dopant migration from the cores to the surfaces of colloidal nanocrystals may sometimes also occur during postsynthesis hydrothermal annealing or other low-temperature anneal processes commonly employed with the colloidal materials. In one study, EXAFS was used to probe niobium and zinc speciation in TiO_2 nanocrystalline powders annealed between 300 and 600°C (119). The Nb^{5+} ion was shown to substitute for Ti^{4+} at the D_{2d} cation site of anatase at all annealing temperatures. Samples with Zn^{2+} concentrations greater than ~0.1% showed segregation to the grain boundaries with annealing at 600°C, however. The Zn^{2+} was found to adopt coordination environments and Zn—O bond lengths similar to those of wurtzite ZnO. As discussed previously, XRD is not sufficiently sensitive to detect such minority phases, and their presence can only be identified by dopant-specific probes such as EXAFS. In this case, the difference in the solid solubilities of Nb^{5+} and Zn^{2+} in TiO_2 is not due to geometric lattice strain, since octahedral Nb^{5+} (0.69 Å) and Zn^{2+} (0.74 Å) have ionic radii very similar to that of Ti^{4+} (0.69 Å). Rather, their difference lies in an electrostatic interaction between charged defects (e.g., interstitial Ti^{2+}) and the dopants that facilitates their comigration to the grain boundaries.

A parallel set of experiments was performed by the same laboratory in a thorough study of Cu^{2+} and Fe^{3+} ion migration in SnO_2 nanocrystalline powders prepared by sol–gel chemistry (58). These dopants were found to migrate to the nanocrystal surfaces at temperatures as low as ~400°C, as evidenced by increased disorder in their coordination environments detected by EXAFS. The segregation of dopants was confirmed by EXAFS measurements of nanocrystals with Cu^{2+} or Fe^{3+} ions deliberately bound to their surfaces, which showed similar disorder [Fig. 23(*b*)]. Since many of the potential processing methods that may eventually be used in applications of doped oxide nanocrystals (see Section V) involve high-temperature anneal steps, the warning from these studies that dopant migration may be activated even at relatively low anneal temperatures in some cases must be heeded. In the particular cases of doped TiO_2 and SnO_2, dopant migration is facilitated by the charge mismatch between dopant and host, which leads to the formation of compensating defects such as oxygen vacancies or interstitial cations. An important functional consequence of dopant migration was demonstrated when it was observed that the CO gas sensing properties of the Fe^{3+}:SnO_2 nanocrystals diminished in concert with dopant segregation (121). These experiments beautifully demonstrate that EXAFS is a powerful dopant-specific spectroscopic probe for studying speciation in impurity-doped inorganic nanocrystals.

F. Luminescence Spectroscopy

As an analytical tool, luminescence spectroscopy is complicated by energy transfer and nonradiative relaxation processes, which may lead to selective observation of a subset of dopant ions that are capable of emitting. This complexity is illustrated in Fig. 24, which describes the various radiative and nonradiative processes deduced from a detailed luminescence lifetime study of Mn^{2+}:CdS nanocrystals (122). The processes include radiative decay of the Mn^{2+} as well as of excited surface traps, and nonradiative decay of these states as well as nonradiative energy transfer among the excitonic excited state, the Mn^{2+}, and the surface traps. The overall observed luminescence is determined by the relative kinetics of each of these processes. Although luminescence spectroscopy may therefore not be a good probe of dopant uniformity from an analytical standpoint, it is arguably the most important analytical probe when the target property is itself luminescence, and in this regard it has been applied successfully in several cases.

The synthesis of Mn^{2+}-doped CdS nanocrystals has been studied by several groups. In one such study (82), the doped CdS nanocrystals were prepared by simple mixing of ethylene glycol solutions of cadmium and manganese acetate with a solution of sodium sulfide, followed by washing with methanol and thermal treatment in triethyl phosphate to deagglomerate the particles. Mean

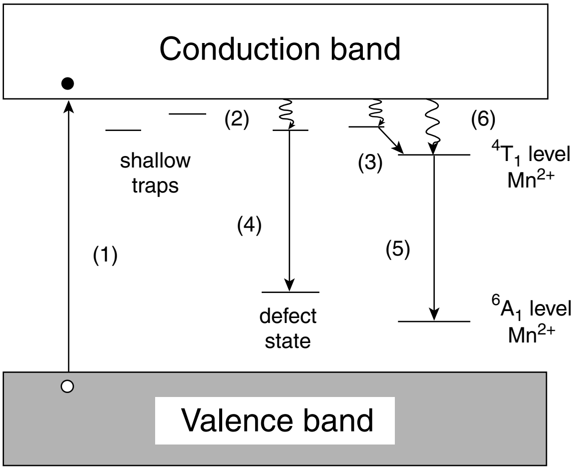

Figure 24. Schematic representation of the proposed radiative and nonradiative processes occurring in nanocrystalline Mn^{2+}:CdS. The straight lines represent radiative processes and the curved lines represent nonradiative processes. (1) Absorption to generate excitonic excited state. (2) Energy transfer to defect. (3) Energy transfer to Mn^{2+} via defect. (4) Radiative decay of defect. (5) Radiative decay of Mn^{2+}. (6) Direct energy transfer to Mn^{2+}. [Adapted from (122).]

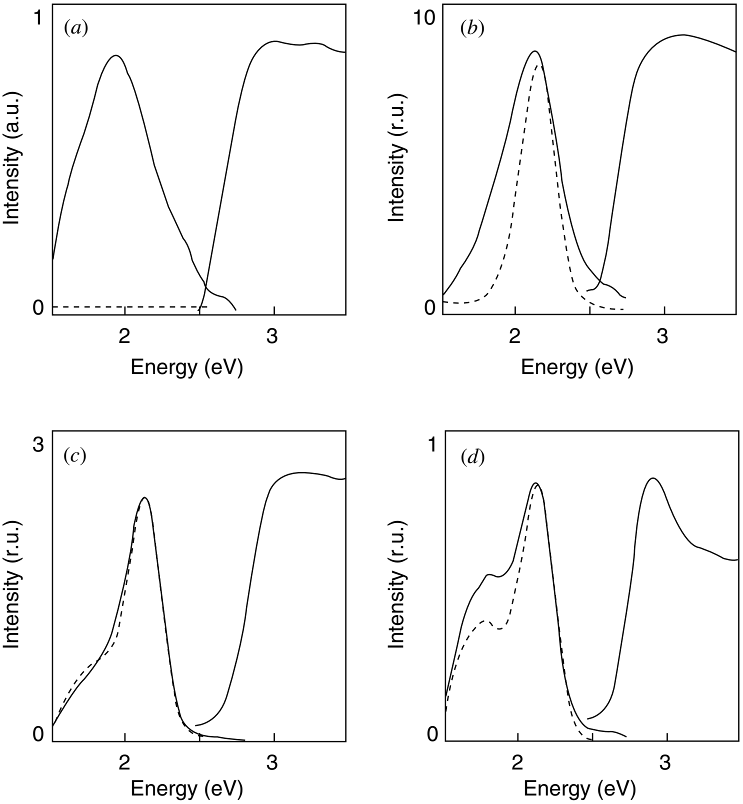

Figure 25. Excitation and photoluminescence (solid and dashed lines) of $x\%$ Mn^{2+}:CdS nanocrystals, where $x = 0$ (*a*), 0.8 (*b*), 2.5 (*c*), and 4.8 (*d*). The solid luminescence spectra were collected in CW mode, and the dashed luminescence spectra were collected with a pulsed excitation source and a 2-ms delay between excitation and emission detection. Note that the intensities of (*b*)–(*d*) are referenced to that of (*a*). [Adapted from (82).]

diameters of ~2.4 nm were determined by X-ray diffraction measurements. Luminescence spectra of these nanocrystals for various doping levels are shown in Fig. 25. The authors identified three distinct emission features that could be correlated to Mn^{2+} doping concentrations. At low or no doping, the emission was dominated by surface trap states of the CdS nanocrystals and appeared as a broad band centered at ~1.9 eV [Fig. 25(*a*)]. The lifetime of this emission was determined to be in the microsecond time scale. At 0.8% Mn^{2+} doping [Fig. 25(*b*)], a new, sharper emission feature centered at 2.16 eV became dominant in the luminescence spectra of the colloids. This feature had a room temperature lifetime of 1.7 ms, and so could be deconvoluted using time-resolved emission spectroscopy. The spectrum of the long-lived component is shown in Fig. 25(*b*) as a dashed line. The energy and lifetime of this feature identify it as arising from the $^4T_1 \rightarrow {}^6A_1$ ligand-field transition of Mn^{2+} ions very likely within the crystalline CdS lattice, where they are isolated from solvent vibrations, and hence have a bulk-like lifetime. The quantum yield for this emission was estimated to be on the order of 60%. As the Mn^{2+} concentration was increased, a third emission feature appeared at ~1.77 eV that also had a lifetime on the millisecond time scale [Figs. 25(*c*) and 25(*d*)]. The quantum yield for this emission was estimated to be on the order of 1%. The relative intensities of the two Mn^{2+} emission features were then plotted versus Mn^{2+} concentration, and the results were found to correlate with reasonable agreement to the Poisson doping statistics for these Mn^{2+} concentrations, discussed in Section I (Eq. 2). These data are plotted in Fig. 26 and fitted to a Poisson function for (a) $P(n) = 1$ and (b) $P(n) = 2$–5. From these data, the authors concluded that the emission of the doped nanocrystals is characteristic of the number of Mn^{2+} ions contained within the nanocrystals, and hence that luminescence spectroscopy may be used to determine the mean concentrations and distribution of Mn^{2+} ions among the particles in this low doping limit.

In another set of studies, it was found that aging of Mn^{2+}-doped CdS QD preparations for ~48 h prior to surface capping yielded higher quality Mn^{2+}:CdS nanocrystals (65, 66). With aging, the average nanocrystal diameter increased from 3.2 to 4.0 nm, indicative of growth of a CdS layer around the initially prepared QDs via Ostwald ripening. Importantly, aging also led to an average decrease in Mn^{2+} concentration per QD by ~40%, showing that the dopants segregated during Ostwald ripening. The final product showed better resolved manganese hyperfine splittings in the EPR spectra, as well as enhanced

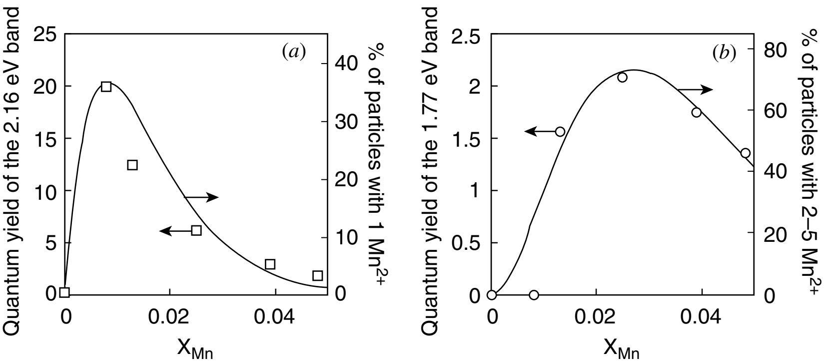

Figure 26. Experimental photoluminescence quantum yields for Mn^{2+}:CdS nanocrystals, plotted versus Mn^{2+} concentration: (*a*) for the long-lived yellow emission from Figure 25; (*b*) for the short-lived red emission from Figure 25. The solid lines represent the proportion of particles with (*a*) 1 and (*b*) 2–5 Mn^{2+} dopant ions, as described by Eqs. 1 and 2. [Adapted from (82).]

$^4T_1 \rightarrow {}^6A_1$ emission intensities (66). The increased Mn^{2+} $^4T_1 \rightarrow {}^6A_1$ luminescence intensity and resolution in EPR spectrum are consistent with internalization of Mn^{2+} ions within the cores of CdS nanocrystals, that is, greater homogeneity in dopant speciation. Ostwald ripening was thus concluded to internalize near-surface or surface-bound Mn^{2+} ions. Although unintentional, this aging process is ultimately very similar to the isocrystalline core–shell methodology discussed in Section II.D.

In many cases, luminescence spectroscopy can only serve as an indirect probe of doping because the dopant ions themselves act as effective nonradiative traps. For transition metal ions, multiphonon relaxation is usually the dominant nonradiative decay process. Multiphonon relaxation is adequately described using the single configurational coordinate (SCC) model, which assumes that the coupling responsible for nonradiative decay can be approximated by the interactions between the donor (excited) and acceptor (e.g., ground or lower excited state) potential surfaces along one single effective nuclear coordinate, Q_{eff}. Within the "super simple harmonic oscillator approximation" (harmonic potential surfaces, identical force constants and normal-coordinate descriptions in the ground and excited states), the $T = 0$ K multiphonon decay rate constant is given by Eq. 7:

$$k_{\text{mp}}(0) \approx (E)\left(\frac{e^{-S}S^{p}}{p!}\right) \tag{7}$$

where, $p = \Delta E_{0-0}/\nu_{\text{eff}}$ is the dimensionless energy gap between the upper state and the closest lower energy state in units of the vibrational energy, ν_{eff} (cm^{-1}), of the effective nuclear coordinate Q_{eff}. The parameter E is the electronic transmission factor, and S is the Huang–Rhys dimensionless excited-state distortion parameter in units of ν_{eff}. As seen in Eq. 7, k_{mp} is strongly dependent on the reduced energy gap, p. Additionally, for a fixed gap, the introduction of even small excited-state distortions, S, can dramatically increase k_{mp}. This model is easily extended to elevated temperatures, where substantial increases in k_{mp} may be observed due to thermal population of excited vibrational levels. For tetrahedral Mn^{2+}, p is large ($p \approx 28\text{B}/\nu_{\text{eff}}$, where B is the Racah e^-–e^- repulsion parameter) due to electron–electron repulsion because the $^4T_1 \rightarrow {}^6A_1$ transition requires a spin flip [Fig. 20(*b*)]. In contrast, the $^4T_1(P)$ state of tetrahedral Co^{2+} occurs at a similar energy above the ground state as the Mn^{2+} $^4T_1$ state does, but lies just above the nearby $^4T_1(F)$ state, and hence has a substantially smaller energy gap ($p \approx 12\text{B}/\nu_{\text{eff}}$). Consequently, Co^{2+}:ZnS shows emission from the $^4T_1(P)$ state only at cryogenic temperatures (123), whereas Mn^{2+}:CdS emits at room temperature with high quantum efficiency. The presence of low-energy excited states in Co^{2+} is responsible for the rapid nonradiative decay of the

Co^{2+} $^4T_1(F)$ state. In fact, the absence of low-energy excited states is unique to Mn^{2+} among divalent tetrahedral 3*d* transition metal ions, and consequently Mn^{2+} is the only efficient 3*d* TM^{2+} activator for visible luminescence.

IV. PHYSICAL PROPERTIES: SOME CASE STUDIES

In this section, we discuss the application of several physical methods not as analytical techniques, but as probes of the electronic structures and functionally relevant properties of doped inorganic nanocrystals.

A. Luminescence of Mn^{2+}:ZnS Nanocrystals

The luminescence properties of doped semiconductors have attracted a great deal of interest for many years, and the emergence of synthetic methodologies for preparing doped semiconductor nanocrystals has sparked new interest in the properties of this class of materials. As described in the Introduction, initial claims (33) that Mn^{2+}:ZnS QDs represented a new class of luminescent materials combining high-luminescence quantum yields with fast radiative decay now appear to have been somewhat overstated. To test these claims, luminescence decay kinetics were measured for Mn^{2+}:ZnS nanocrystals in several laboratories almost simultaneously (35–38). These experiments detected a fast ($\tau = 40$, 250 ns) multiexponential decay similar to that initially reported (33), but also showed that this fast decay was followed by a slow single-exponential decay having a long lifetime [$\tau = 1.9$ ms (35)] equivalent to that of bulk Mn^{2+}:ZnS ($\tau = 1.8$ ms) within experimental error. The association of the long-lived emission with Mn^{2+} is demonstrated by the time-resolved emission spectra of nanocrystalline Mn^{2+}:ZnS shown in Fig. 27. The fast decay signal, centered at 405 nm but tailing throughout much of the visible, was attributed to the intrinsic emission of the ZnS nanocrystals. The slow emission, centered at 580 nm, is clearly associated with the $^4T_1 \rightarrow {}^6A_1$ transition of the Mn^{2+}. Subsequent reports helped to substantiate the interpretation of fast decay from traps and slow decay from Mn^{2+}, and have additionally reported the observation of a fast Mn^{2+} emission decay associated with surface-exposed Mn^{2+} ions (37).

The absence of an enormous enhancement in radiative decay rates in the nanocrystals can also be verified by electronic absorption spectroscopy. The original claim stated that the Mn^{2+} $^4T_1 \rightarrow {}^6A_1$ radiative decay lifetime dropped from $\tau_{rad} = 1.8$ ms in bulk Mn^{2+}:ZnS to $\tau_{rad} = 3.7$ ns in ~0.3% Mn^{2+}:ZnS QDs (~3.0 nm diameter) (33). This enhancement was attributed to relaxation of Mn^{2+} spin selection rules due to large *sp–d* exchange interactions between the dopant ion and the quantum-confined semiconductor electronic levels (33, 124–127). Since the Mn^{2+} $^4T_1 \rightarrow {}^6A_1$ radiative transition probability is determined

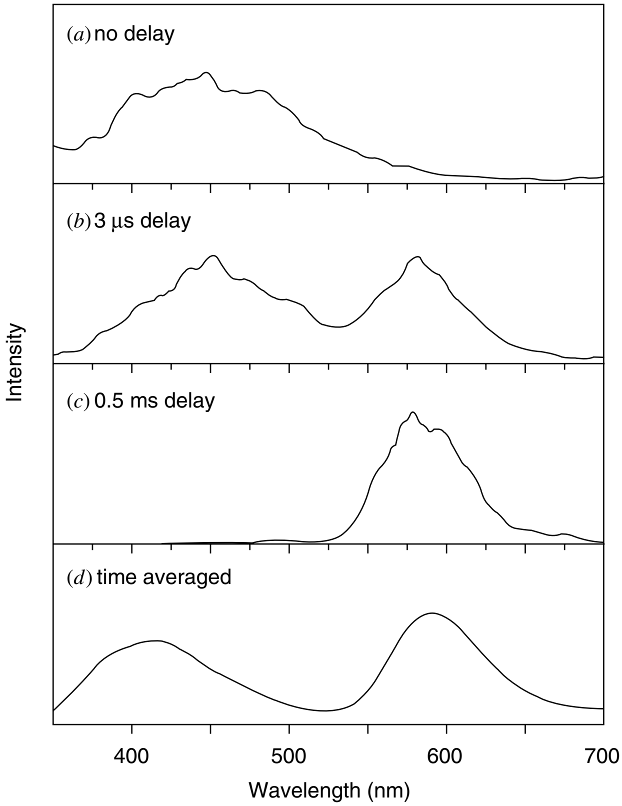

Figure 27. 300 K time-resolved luminescence spectra of Mn^{2+}:ZnS nanocrystals. Applied delay times and gate widths are, respectively, (*a*) ~0 and 2 μs, (*b*) 3 and 200 μs, and (*c*) 0.5 and 1 ms. Pulsed excitation at 266 nm was provided by a Nd^{3+}:YAG laser. (*d*) The time-averaged emission spectrum. [Adapted from (35).]

by the same transition probability integrals that govern the $^6A_1 \rightarrow {}^4T_1$ absorption transition, the radiative decay rate constant ($k_{\mathrm{rad}} = \tau_{\mathrm{rad}}{}^{-1}$) can be estimated from quantitative measurement of the absorption intensity. Equation 8a relates τ_{rad} to the absorption oscillator strength, f, of an electronic transition between ground (a) and excited (b) states, and Eq. 8b relates f to the molar absorption coefficient, $\varepsilon_{\max}$ (128, 129)

$$\tau_{\mathrm{rad}}^{-1} = f\frac{g_a}{g_b}\frac{n[(n^2+2)/3]}{\alpha\lambda^2} \tag{8a}$$

$$f = 4.315 \times 10^{-9}\int \varepsilon d\nu \approx 4.61 \times 10^{-9}\varepsilon_{\max}(\mathrm{fwhm}) \tag{8b}$$

where fwhm = full width at half-maximum. The origin (18,150 cm^{-1}), maximum (19,231 cm^{-1}), and spectral bandwidth (fwhm $\leq$ 1750 cm^{-1}) of the $^6A_1 \rightarrow {}^4T_1$ absorption transition of Mn^{2+} in ZnS at 300 K are known from bulk absorption studies and from luminescence excitation spectra of Mn^{2+}:ZnS DMS–QDs (130). From high-sensitivity absorption spectra of colloidal Mn^{2+}:ZnS nanocrystals collected over the energy region where the $^6A_1 \rightarrow {}^4T_1$ transition is anticipated, the $^6A_1 \rightarrow {}^4T_1$ transition is not observed allowing an upper limit of $\varepsilon_{\mathrm{max}} \leq 1.5\,M^{-1}\mathrm{cm}^{-1}$ to be estimated (131). This value is comparable to that of bulk Mn^{2+}:ZnS ($\varepsilon_{\mathrm{max}}$ ranges from 0.1–1 $\mathrm{M}^{-1}\mathrm{cm}^{-1}$) (132). Using the total degeneracy of the $^4T_1$ excited state of $g_b = 12$, that of the $^6A_1$ ground state of $g_a = 6$, the ZnS bulk index of refraction ($n = 2.37$), and the proposed $\tau_{\mathrm{rad}} = 3.7$ ns (33), Eq. 8b yields $\varepsilon_{\mathrm{max}} \approx 23{,}000\ \mathrm{M}^{-1}\mathrm{cm}^{-1}$. In such a case, the $^6A_1 \rightarrow {}^4T_1$ absorption feature would be clearly observable in the absorption spectra of Mn^{2+}:ZnS nanocrystals, since it would be comparable in intensity to the ZnS band-gap absorbance. For comparison, the value for $\varepsilon_{\mathrm{max}}$ calculated from Eq. 8b using bulk $\tau_{\mathrm{rad}} = 1.8$ ms is $\varepsilon_{\mathrm{max}} \approx 0.05\,M^{-1}\mathrm{cm}^{-1}$, consistent with the experimental data. This simple calculation rules out the possibility of greatly enhanced Mn^{2+} radiative decay rates in nanocrystalline Mn^{2+}:ZnS and supports the assertion that the short lifetime originally reported arises from nonradiative deactivation pathways involving surface Mn^{2+} or other surface traps (35–38).

In fact, Yu et al. (133) examined the time-resolved emission spectra of Mn^{2+}:ZnS nanocrystals under high excitation densities and have reported the observation of luminescence from thermally nonequilibrated $^4T_1$ excited states of Mn^{2+}. Figure 28 shows the room temperature time-resolved emission spectra of Mn^{2+}:ZnS nanocrystals estimated to contain <0.1% Mn^{2+} in ZnS. The emission was excited using 40 ns pulses at 248 nm. Interestingly, at 1-μs delay time, the Mn^{2+} emission spectrum shows a split peak with a dip at 590 nm, precisely where the maximum of the time-averaged emission spectrum occurs. With an increase in delay time, the splitting of the peaks decreases, and at times >150 μs only a single peak is observed. The splitting of the two peaks showed no significant temperature dependence, but was found to depend on the pulse excitation power density (~4–8 mJ cm^{-2}). These results were explained as a manifestation of hot nonthermally equilibrated excited-state populations, which give rise to luminescence from the classical turning points of the $^4T_1$ excited-state potential energy surface to the $^6A_1$ ground state. Subsequent reexamination of these data (134) showed that the unusual band shapes could be reproduced using a SCC model by assuming only a nonequilibrium initial distribution among vibrational levels of the $^4T_1$ state. The calculated emission line shapes as a function of time, fitted to the data from Yu et al. (133), are shown in Fig. 29 and reproduce the experimental data well. Importantly, the fits involved only two adjustable parameters, the initial mean occupation number, $p(n,0)$, and the relaxation

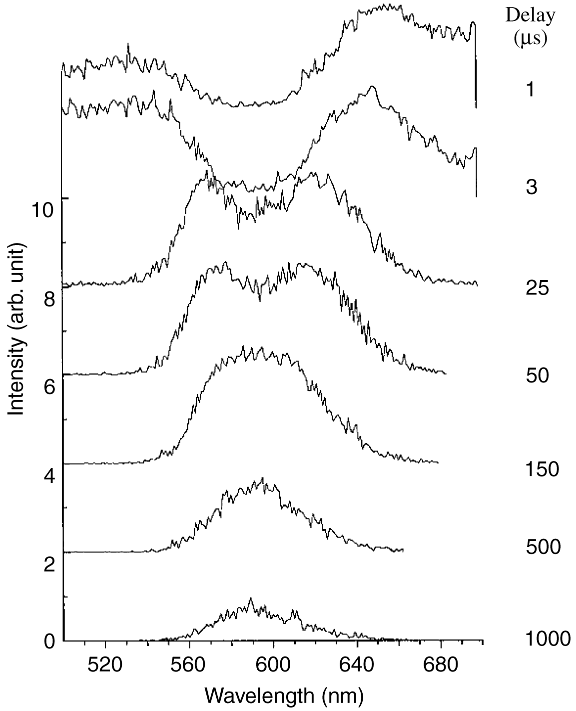

Figure 28. The 300 K time-resolved luminescence spectra of Mn^{2+}:ZnS nanocrystals in polyvinyl butyral (PVB) films, collected at the various delay times indicated following a 248-nm excimer laser pulse (pulse width 40 ns, 2 Hz, excitation density = 5.6 mJ/cm^2, detection gate width = 2 μs). [Adapted from (133).]

rate constant, C, within the $^4T_1$ excited state. Other parameters such as the Huang–Rhys parameter and the vibrational frequency were determined independently. These calculations supported the original interpretation of the data. The authors also noted that the relaxation rate constant, $C = 5.0 \times 10^4 s^{-1}$, extracted from the calculations is several orders of magnitude smaller than those of the corresponding bulk materials ($C = 10^{10} s^{-1}$), and this may reflect correspondingly smaller coupling of the local vibrational mode defining the Mn^{2+} excited-state potential surface to the reservoir of lattice modes. This conclusion finds support in earlier studies in which the phonon density of states in nanoparticles was found to be significantly smaller than in the corresponding bulk materials (135). This nonthermalized Mn^{2+} excited-state population in Mn^{2+}:ZnS nanocrystals therefore appears to result from the effect of the crystallite's finite size on the phonon density of states in the crystal, akin to

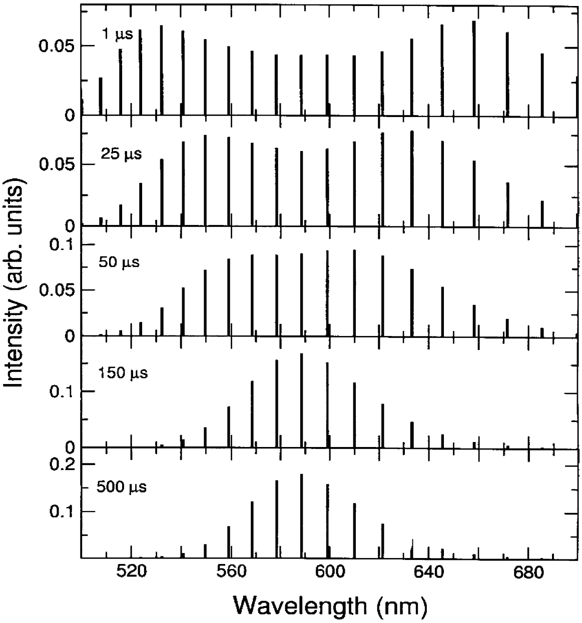

Figure 29. Calculated emission line shapes as a function of delay time, simulating the data presented in Figure 28. [Adapted from (134).]

the slow rates of internal conversion proposed and observed for excitonic states in QDs (136).

B. Magnetism

Magnetic susceptibility is a bulk technique that cannot easily separate contributions from multiple dopant sites if dopant inhomogeneities exist. Even for statistically doped materials with uniform dopant speciation, the significant probability of finding dopant clusters even at low dopant concentrations (discussed in Section I) contributes to the complexity of magnetic susceptibility data and the information content of this experiment may be difficult to interpret in its full detail. Nevertheless, the influence quantum confinement may have on the magnetic properties of DMSs has intrigued researchers and motivated the study of DMS nanocrystals by magnetic susceptibility. Whereas the size-dependence of the magnetic properties of nanocrystalline hard ferromagnets like Fe, Ni, and Co has been studied in detail (137), analogous effects in nanoscale DMSs have not.

A central motivation for the preparation of magnetically doped semiconductor nanocrystals is the possibility of creating ferromagnetic DMS colloids that can be used as components of self-assembled spintronic nanostructures, integrated into devices such as those currently made by self-assembly of non-magnetic semiconductor nanowires and nanocrystals (138, 139). Although this may at first appear to be an insurmountable challenge, it is noteworthy that room temperature ferromagnetism has been observed in nanoscale DMSs grown epitaxially on semiconductor surfaces. Ferromagnetism above room temperature has been reported for nanoscale epitaxial islands of manganese-doped InAs (140) (typically $\sim 60 \times \sim 20$ nm, 16% Mn) and cobalt-doped TiO_2 (141, 142) (typically $\sim 90 \times \sim 12$ nm, up to 40% Co) DMSs on semiconductor surfaces, and a device showing very large magnetoresistance effects (up to 2000%) from ferromagnetic manganese-doped GaAs DMS nanowires of ~100- and 400-nm diameters connected by sub-10-nm constrictions has already been demonstrated at 4.2 K (31). A major motivation for exploring colloidal DMS nanocrystals can thus be stated as the desire to detach such ferromagnetic islands from their substrates to take advantage of processing capabilities already exploited for other colloidal semiconductor nanocrystals. The development of colloidal ferromagnetic DMS nanocrystals that mimic the epitaxial nanostructures grown by MBE and other vacuum deposition methods should be possible, and this would open the door to self-assembly approaches to spin-based semiconductor devices. To date, no free-standing ferromagnetic DMSs have been made, however. The relatively few colloidal DMSs that have been prepared and studied by magnetic techniques have shown only paramagnetism, sometimes perturbed by antiferromagnetic dopant–dopant exchange interactions, and in some cases by spin–glass transitions or antiferromagnetic ordering at low temperatures (see below).

The magnetization of paramagnetic transition metal ions in Mn^{2+} DMSs is often described by the Brillouin function, shown in Eq. 9. Here, μ_B is the Bohr magneton and N represents the number of dopant ions in the sample, typically derived from the experimental dopant concentrations determined by inductively coupled plasma–atomic emission spectroscopy (ICP–AES) or analogous analytical methods. The parameter H is the applied magnetic field, k is the Boltzmann constant, T is the temperature, S is the spin state, and g is the Landé Zeeman factor. In studies of the magnetization of bulk Mn^{2+}:CdTe and Mn^{2+}:CdSe this expression was modified by defining an effective temperature, $T_{\text{eff}} = T + T_0$, which accounts for Mn^{2+}–Mn^{2+} superexchange interactions at higher concentrations (41). For all known cases, $T_0 > 0$, indicating antiferromagnetic exchange interactions. Using T_{eff} in Eq. 9, the magnetization, M, is reduced by an amount related to the magnitude of antiferromagnetic exchange coupling. The parameter T_0 is thus analogous to the Curie–Weiss temperature, Θ. Although empirical, this modified Brillouin function has proven useful in many cases.

$$M = \frac{1}{2} N g \mu_B \left[(2S+1) \coth\left((2S+1) \left(\frac{g\mu_B H}{2kT} \right) \right) - \coth\left(\frac{g\mu_B H}{2kT} \right) \right] \tag{9}$$

Equation 9 (and its empirical modification) is appropriate for describing the magnetization of Mn^{2+} ions in DMSs since their $^6A_1$ ground state has no orbital angular momentum and the energy gap between this and the first excited state ($^4T_1$) is large such that second-order spin–orbit coupling effects are small. The axial zero-field splitting parameter for Mn^{2+} in ZnO is only $D = -2.36 \times 10^{-2}$ cm^{-1}, for example (143, 144). Although tetrahedral Co^{2+} also has no orbital angular momentum in its ground state ($^4A_2$), the proximity of the $^4T_2(F)$ excited state gives rise to a larger zero-field splitting (e.g., $D = +5.5\,cm^{-1}$ in ZnO) (145), and the Brillouin function fails outside of the Curie region of high temperatures and small fields. In the case of Ni^{2+}, which has both spin and orbital angular momentum in its cubic ground-state ($^3T_1$), first-order spin–orbit coupling splits the ground state by hundreds of wavenumbers (52, 146) and the magnetization must be analyzed by explicit consideration of the Zeeman elements for each spinor level. Ni^{2+} in II–VI semiconductors is a classic example of temperature-independent paramagnetism. In addition to the high solid solubility of Mn^{2+} in II–VI lattices, the simplicity of its ground state for magnetic studies must be in part responsible for the overwhelming focus of DMS literature on Mn^{2+} DMSs.

In order to study the magnetism of freestanding DMS–QDs, interparticle exchange must be prevented, and this is usually accomplished using bulky surface ligation. The magnetic properties of Co^{2+}-doped CdSe nanocrystals (0.4–30% Co^{2+}) with surfaces cleaned by Py stripping (see Section II.D) and passivated with Py ligation have been studied in detail (70). At low concentrations and high temperatures, an effective magnetic moment of $\mu_{eff} = 3.52\,\mu_B/Co^{2+}$ was measured. This moment is close to the spin-only value of $3.87\,\mu_B/Co^{2+}$ and confirmed the predominance of isolated paramagnetic Co^{2+} at low concentrations. At higher Co^{2+} concentrations (17 and 30%), antiferromagnetic Co^{2+}—Co^{2+} superexchange coupling was observed and analyzed using a Curie–Weiss model to estimate the antiferromagnetic Heisenberg exchange coupling constants describing superexchange between nearest-neighbor Co^{2+} ions (J_{NN}/k_B). The parameter J_{NN}/k_B was claimed to vary with dopant concentration from $+0.1$ K in 0.4% Co^{2+}:CdSe nanocrystals to -122 K in 30% Co^{2+}:CdSe nanocrystals. Evidence for a spin-glass (SG) phase transition was also observed below 4 K for all concentrations. The authors observed spin-glass transition temperatures (T_g between 2 and 4 K) that were significantly higher than those of bulk Co^{2+}:CdSe, where T_g temperatures between 0.1 and 0.9 K have been observed (147). The dependence of T_g on dopant concentration, x, was modeled

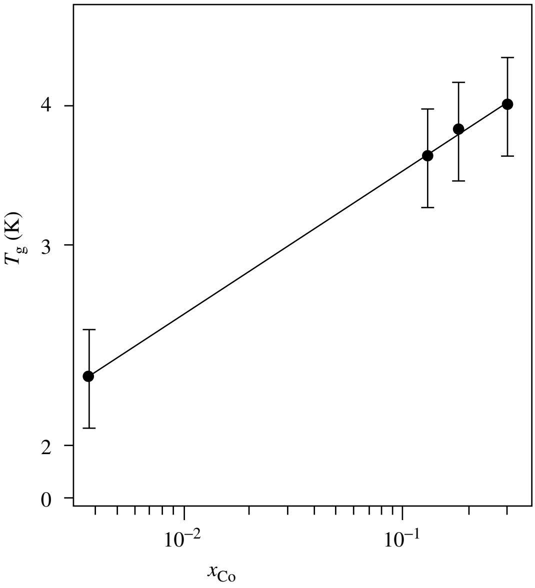

Figure 30. Double-log plot of the spin-glass transition temperature, T_g, versus mole fraction of dopant for Co^{2+}:CdSe nanocrystals. [Adapted from (70).]

by the expression $T_g = Bx^{n/3}$, where B is a constant (shown in Fig. 30). The bulk data were best fit when $n \sim 6.3$ (148), and the nanocrystal data were best fit with $n \sim 0.38$ (70). The smaller value of n was interpreted as indicating a much longer superexchange interaction length in the nanocrystals. One of the possible interpretations of the higher spin-glass transition temperatures and larger superexchange coupling constants considered by the authors related these trends to quantum confinement, in which the shift in the valence band energy relative to the Co^{2+} valence orbitals with decreasing nanocrystal diameter led to enhanced *p–d* hybridization. Further investigation to determine the generality of these intriguing observations and conclusions would certainly be warranted.

The magnetic properties of manganese-doped InAs nanocrystals with diameters ranging from 2.2 to 10 nm and doping levels up to 5% have been reported recently (71). These nanocrystals were prepared by high-temperature arrested precipitation involving dehalosilylation of $InCl_3$ and $MnBr_2$ with tristrimethylsilylarsine in the coordinating solvent, trioctylphosphine (TOP). The nanocrystals were stirred in Py for 24 h to remove surface manganese, and approximately one-half of the manganese was found to be solvated under these conditions. The Mn^{2+} EPR signals were observed after Py ligand exchange [Fig. 31(*a*)],

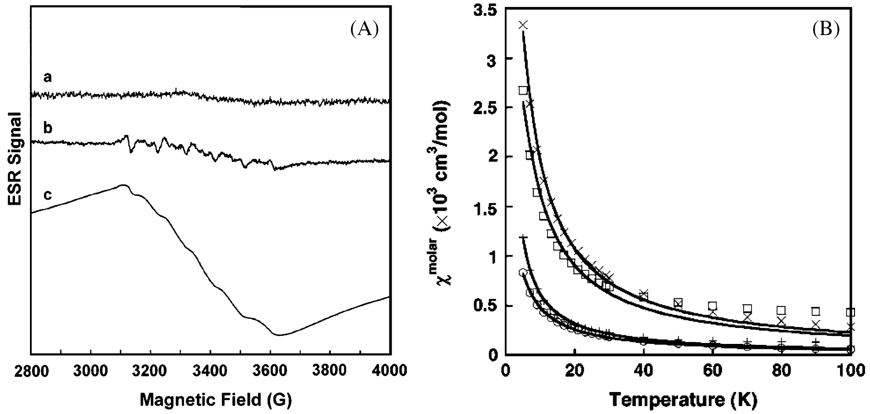

Figure 31. (A) The 115 K X-band EPR spectra of (*a*) TOP-capped 5-nm diameter InAs nanocrystals, (*b*) TOP-capped 5 nm diameter 1% manganese-doped InAs nanocrystals, and (*c*) pyridine-capped 5-nm diameter 2.4% manganese-doped InAs nanocrystals. (B) Temperature-dependent magnetic susceptibilities for manganese-doped InAs nanocrystals, measured at 0.5 *T*: (*x*) 4-nm diameter, 2.4% Mn, (□) 4-nm diameter, 4.8% Mn, (+) 4.6-nm diameter, 1.4% Mn, (O) 4-nm diameter, 2.0% Mn. The solid lines are the best fits of the Curie–Wiess expression to the data, assuming $S = \frac{5}{2}$. The fits yielded effective magnetic moments of 3.7, 3.0, 2.7, and 2.2 μ_B/Mm, and J_{NN}/k_b exchange constants of −4.3, −2.1, −2.7, and −3.7 K, respectively. [Adapted from (71).]

from which the authors concluded that manganese was in the Mn^{2+} oxidation state. Although Mn^{3+} would be the charge neutral oxidation state, no evidence of Mn^{3+} was found, suggesting the possibility that manganese also serves as a *p*-type dopant in these nanocrystals, but evidence of this was also not detected. We note that Mn^{3+} would not have been observed in this EPR experiment because of its non-Kramers ground state. Magnetic susceptibility measurements on these nanocrystals [Fig. 31(*b*)] showed temperature-dependent molar susceptibilities that varied with dopant concentration. Paramagnetism was reported between 5 and 100 K, and deviations from Curie behavior attributed to antiferromagnetic exchange were analyzed using the Curie–Weiss law assuming a Néel transition temperature <5 K. The $J_{\text{NN}}/k_{\text{B}}$ values for the various dopant concentrations were determined from the temperature-dependent susceptibility data and ranged from −2.0 to −4.3 K, values that are greater than but comparable to the value of $J_{\text{NN}}/k_{\text{B}} = -1.6$ K found for bulk Mn-doped InAs. The effective magnetic moments, which ranged from $\mu_{\text{eff}} = 2.2$–$3.7\ \mu_{\text{B}}$/Mn, were substantially smaller than the spin-only effective magnetic moments for Mn^{2+} ($\mu_{\text{eff}} = 5.92\ \mu_{\text{B}}$) or Mn^{3+} ($\mu_{\text{eff}} = 4.90\ \mu_{\text{B}}$). The authors proposed that the small μ_{eff} values may be attributable to donor–acceptor interactions between Mn^{2+} ions and As_{Ga} antisite defects. The most important aspect of this study is its representation of an attempt to synthesize by wet chemical means DMS nanocrystals of a III–V semiconductor, an area that has hitherto been achieved only by vacuum deposition methods such as molecular beam epitaxy. One may reasonably expect exciting advances in this direction in the near future as the syntheses of III–V DMSs receive more attention from chemists.

The absence of ferromagnetic ordering in these manganese-doped InAs DMS nanocrystals is noteworthy, since the colloidal Mn^{2+}:InAs QDs (71) appear to have sufficient Mn^{2+} to be analogous to ferromagnetic islands grown by molecular beam epitaxy (140), only with much smaller dimensions (<10-nm diameter vs. ~60 × 20-nm rod). Similarly, colloidal Co^{2+}:TiO_2 DMS—NCs studied by cobalt K-edge X-ray absorption and EXAFS spectroscopies (55) appear to be nearly identical to analogous ferromagnetic anatase islands grown by MBE (140), but are again somewhat smaller (~6 × 3 vs. ~90 × 12-nm islands) and show only paramagnetism. Likewise, many ferromagnetic thin films of ZnO DMSs grown by vacuum deposition methods have been reported (149–153), but only paramagnetism has been observed in freestanding nanocrystals of these same DMSs (52, 54, 154). Carrier-mediated magnetic ordering mechanisms have been proposed for each of these ferromagnetic DMSs (155), and it is possible that the DMS nanocrystals prepared to date lack the donor or acceptor defects necessary for magnetic ordering. Whereas vacuum deposition techniques are capable of controlling carrier concentrations quite well, wet chemical approaches to electronic doping are only now being developed and still suffer from many of the same challenges as described here for magnetic dopants. Recent work in which room temperature ferromagnetism was observed upon aerobic aggregation of paramagnetic ZnO DMS nanocrystals at room temperature (154) has provided some clues about how to generate ferromagnetism from colloidal DMS nanocrystals (see Section V.C), but research in this direction is still at an early stage. With each success will come a deeper understanding of the microscopic origins of ferromagnetism in this interesting class of materials.

C. Magnetooptical Spectroscopies and *sp–d* Exchange Interactions

Very few magnetooptical studies of free-standing DMS quantum dots have been reported, although there is a growing body of literature dedicated to magnetooptical studies of epitaxial DMS quantum dots. The first studies of free-standing DMS nanocrystals were of Mn^{2+}-doped CdS (67) and ZnSe QDs (49), and both used analysis of magnetic circular dichroism (MCD) data to quantify the influence of the magnetic dopant on the electronic structure of the semiconductor. Specifically, MCD spectroscopy was used to determine the magnitudes of the excitonic Zeeman splittings (ΔE) in these nanocrystals, and in both cases enhancement of short-range spin–spin interactions in the nanocrystals relative to bulk was concluded. In the first study (67), ΔE was estimated for Mn^{2+}:CdS nanocrystals synthesized by the inverted micelle procedure discussed in Section II. Doping by Mn^{2+} was confirmed by EPR and luminescence spectroscopy, but the Mn^{2+} concentration was not determined analytically. The nanocrystals showed an intense pseudo-$\mathcal{A}$ term MCD signal at the band edge that displayed $S = \frac{5}{2}$ saturation magnetization. The ODMR (ODMR = optically detected magnetic resonance) measurements further verified its association with the Mn^{2+} ions. The MCD signal intensities were converted to excitonic Zeeman splitting energies using Eq. 10, where 2Γ is the linewidth of the first excitonic transition (determined from the absorption spectrum of the same sample), $I^{\max}$ is the maximum intensity of the MCD signal, and $D^{\max}$ is the optical density of the sample at the energy of $I^{\max}$. Equation 10 is appropriate in the limit of $2\Gamma \gg \Delta E$.

$$\Delta E = \frac{2\Gamma I^{\max}}{2.32 D^{\max}} \tag{10}$$

Values for ΔE obtained from this analysis are plotted versus applied magnetic field at 2 and 4.2 K for these Mn^{2+}:CdS nanocrystals in Fig. 32. ΔE was then analyzed using a model in which spatial distributions of Mn^{2+} ions within nanocrystals as well as the reduced magnetization from dimer superexchange up to the third-nearest-neighbor shell were taken into account explicitly. Dopants were assumed to be distributed throughout the nanocrystals statistically. Fitting the data within this model (dashed lines in Fig. 32) yielded a Mn^{2+} concentration of 0.16%. From this concentration, the QDs were estimated to contain an

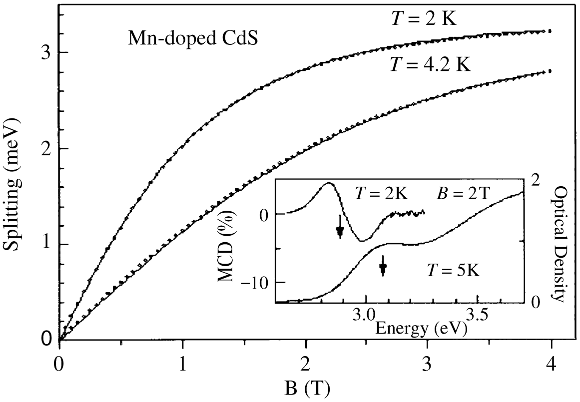

Figure 32. The MCD band-edge intensities of x% Mn^{2+}:CdS nanocrystals, collected as a function of applied magnetic field and temperature and converted to effective band-edge splitting using Eq. 10 (solid lines). Theoretical band-edge splitting calculated for $x = 0.16\%$ (circles). The inset shows the MCD and absorption spectra in the band-edge region. [Adapted from (67).]

average of one Mn^{2+} dopant per crystallite. The authors emphasized the observation of a large Zeeman splitting of the first excitonic state, and moreover emphasized that this splitting should exist in individual nanocrystals containing only one Mn^{2+} ion even in the absence of an applied magnetic field. This splitting is not observed in the MCD experiment at zero field since the measurement probes an ensemble of DMS–QDs with random magnetization directions at zero field. Consequently, the MCD signal is strongly dependent on both temperature and field even though the splitting of the spin sublevels would not depend on these parameters in the limit of one Mn^{2+} per nanocrystal. Within this model, the excitonic splitting at zero field is determined directly from the saturation value of ΔE and equals 3.2 meV in these nanocrystals (67). This value is less than the bulk value of 16 meV for the same dopant concentration (0.16%) (156), a difference the authors attribute to (a) averaging over all possible Mn^{2+} positions in the nanocrystal, since the exchange energy is maximum when the dopant resides in the center of the nanocrystal where the electronic wave functions for the first excitonic state maximize, (b) the close spacing of the three valence subbands that all contribute to the single broad pseudo-$\mathcal{A}$ term MCD signal, but with different signs, and (c) to the random distribution of Mn^{2+} ions among the NCs as discussed in Eqs. 1 and 2. The experimental value for ΔE was thus concluded to be a lower limit, and the authors predicted that by keeping a single Mn^{2+} ion at the center of a nanocrystal and decreasing its size, spin level splittings considerably larger than in bulk DMSs should be obtainable. An alternative explanation for the small ΔE that was apparently not considered is that *sp–d* exchange energies decrease with quantum confinement, a trend suggested by theoretical calculations on Mn^{2+}:CdTe QD heterostructures (157).

In a related study using MCD spectroscopy, Mn^{2+}:ZnSe nanocrystals (49) were prepared by hot injection using $MnMe_2$ as the manganese precursor, and repeated cap exchange with Py was used to verify the internalization of the Mn^{2+}, as probed by EPR and luminescence spectroscopies. The Q-band Mn^{2+} EPR spectrum [Fig. 33(*a*)] confirms the presence of well-isolated Mn^{2+} ions, although the authors stated that other Mn^{2+} species were also observed in this spectrum. The MCD spectra for these DMS–QDs are shown in Fig. 33(*b* and *c*). The first excitonic transition of the ZnSe nanocrystals shows considerable MCD intensity that is dependent upon the strength of the applied magnetic field [Fig. 33(*b* and *c*). The MCD signal intensity was also observed to increase in proportion to the initial Mn^{2+} concentration used for synthesis, with no apparent reduction in magnetization that could be attributed to Mn–Mn dimer formation. From this concentration dependence, the authors concluded that the nanocrystals were in the limit of an average of only one or fewer Mn^{2+} per crystallite (i.e., 0.025–0.125% Mn^{2+}). Since these nanocrystals were prepared with an initial Mn^{2+} cation mole fraction of 2.4% in solution this means that 95–99% of the starting Mn^{2+} was not incorporated into the ZnSe lattices during synthesis.

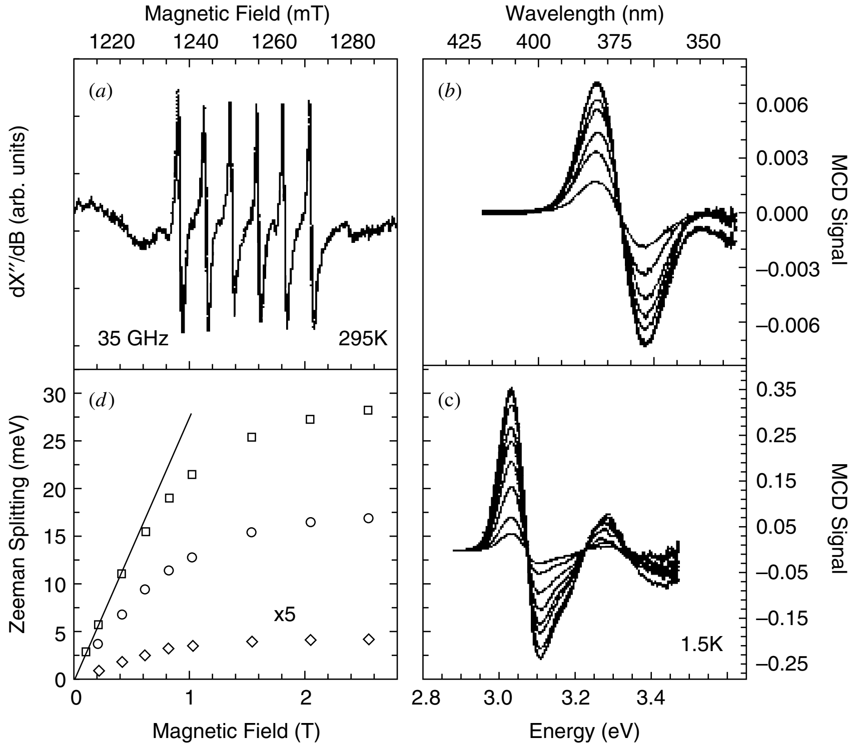

Figure 33. (*a*) The 295 K Q-band EPR spectrum of 2.9-nm diameter 1% Mn^{2+}:ZnSe nanocrystals. (*b*) and (*c*) show 1.5 K variable-field MCD data for 2.9-nm diameter 1% and 5.3 nm 2.5% Mn^{2+}: ZnSe nanocrystals. (*d*) Zeeman splitting (ΔE) versus magnetic field extracted from the data in (*b*, diamonds), (*c*, squares), and for an additional 4.2 nm 2.5% doped sample (circles). The solid line shows a linear fit to the low-field data for (*c*), from which $g_{\text{eff}} = 475$ was calculated. [Adapted from (49).]

The 1.5 K MCD intensities were analyzed as a function of applied magnetic field to extract effective g values describing the excitonic Zeeman splitting in the DMS–QDs. The MCD signal intensities were converted to excitonic Zeeman splitting energies using Eq. 10. The parameter ΔE obtained from this analysis is plotted versus applied magnetic field at 1.5 K for three batches of these Mn^{2+}: ZnSe nanocrystals in Fig. 33(*d*). This analysis yielded an effective excitonic g value of 475 for the Mn^{2+}:ZnSe nanocrystals showing the largest effect (determined from $\Delta E/\beta H$ in the linear region). The ΔE determined in this study is an order of magnitude larger than that found for the Mn^{2+}:CdS nanocrystals in Fig. 32. Note, however, that the authors appear to have used an erroneous form of Eq. 10 for their analysis that would have overestimated ΔE

by a factor of 4, but it is not possible to verify this from the data presented in the paper. The authors concluded by emphasizing the observation of a large Zeeman splitting of the first excitonic state, and also emphasized that this splitting should exist in individual nanocrystals even in the absence of an applied magnetic field because the majority of the QDs were estimated to contain at most one Mn^{2+} dopant.

ZnO QDs doped with Co^{2+}, Ni^{2+}, and Mn^{2+} ions have also been studied by MCD and Zeeman spectroscopies (52, 54). Figure 34 shows the low-temperature absorption and MCD spectra of Co^{2+}:ZnO DMS–QDs (52). The $S = \frac{3}{2}$ saturation magnetization indicated all MCD intensity originated from the Co^{2+} dopants. In addition to showing excitonic MCD intensity similar to those of the Mn^{2+}-doped ZnSe and CdS DMS–QDs described above, these spectra showed rich sub-band-gap features that provided further information about the electronic structures of these materials. As described in Section III.C, the transitions in DMS nanocrystals may be generally classified as LF, CT, or semiconductor band-to-band (BG) transitions (see Fig. 34). The ${}^4A_2 \rightarrow {}^4T_1(P)$ ligand-field transition in Fig. 34 showed extensive absorption and MCD fine structure arising from spin–orbit and vibronic contributions. Note that there is quantitative agreement to within $\sim \pm 1$ cm^{-1} ($\sim$0.01%) between the LF fine structure energies observed in bulk and in these Co^{2+}:ZnO quantum dots. This

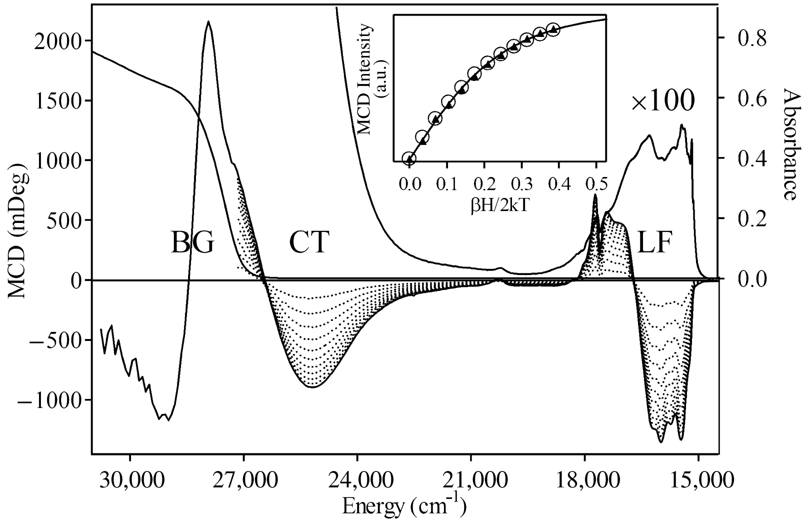

Figure 34. 7 K absorption and 5 K variable-field (0–6.5*T*) MCD spectra of 1.7% Co^{2+}:ZnO nanocrystals. The inset shows the $S = \frac{3}{2}$ saturation magnetization of the LF(○) and BG(▲) MCD intensities. Ligand-field (LF), charge-transfer (CT), and band gap (BG) transitions are indicated. [Adapted from (52).]

suggested that dopants in ZnO are relatively insensitive to quantum confinement, at least in the weak confinement regime. To higher energies, the Co^{2+}:ZnO nanocrystals showed excitonic MCD intensity similar to those of the Mn^{2+}:ZnSe and Mn^{2+}:CdS DMS–QDs discussed above. The LF and excitonic transitions were of comparable MCD intensity, despite the fact that the absorption cross-sections of the latter exceeded those of the former by nearly two orders of magnitude. The smaller $\mathcal{C}_0/\mathcal{D}_0$ ratios (157) for the excitonic transition reflects the indirect mechanism by which this transition gains MCD intensity, namely, through dopant–host covalency.

The 1.7% Co^{2+}:ZnO DMS–QDs in Figure 34 were also examined by Zeeman spectroscopy in transmission mode. An average band-edge Zeeman shift of ~53 cm^{-1}/T over the range of 0–7 T (Fig. 35) was measured. The Zeeman data were analyzed in the mean-field approximation using Eq. 11, where x is the dopant mole fraction and $\langle S_z \rangle$ is the expectation value of the S_z operator of the spin Hamiltonian. $N_0\alpha$ and $N_0\beta$ quantify the exchange interactions between the dopant and unpaired spins in the conduction (CB) and valence bands (VB), respectively (19, 159–161).

$$\Delta E_{\text{Zeeman}}(\text{CB}) = xN_0\alpha\langle S_z \rangle \tag{11a}$$

$$\Delta E_{\text{Zeeman}}(\text{VB}) = xN_0\beta\langle S_z \rangle \tag{11b}$$

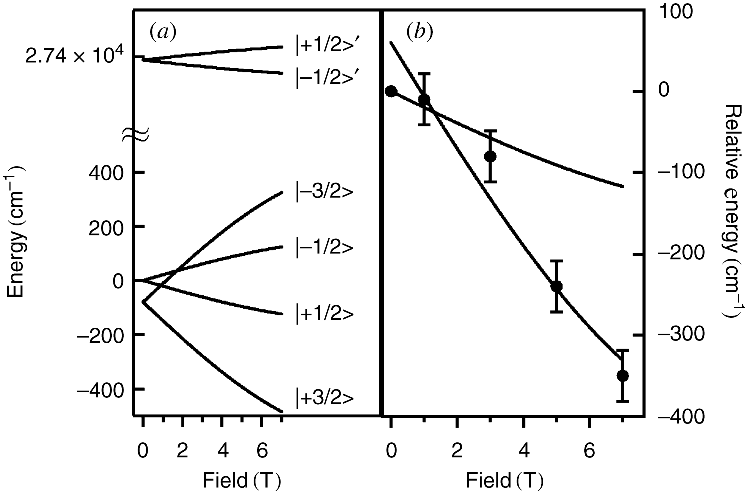

Figure 35. (*a*) Zeeman-splitting pattern for the one-electron band levels of ZnO DMSs with H||z. (*b*) Experimental band-edge Zeeman shift for 1.7% Co^{2+}:ZnO DMS nanocrystals (see Fig. 34). The solid lines represent the transition energies predicted from the Zeeman splittings shown in (*a*) using $N_0\beta = -2.3$eV. [Adapted from (52).]

The covalency of the oxo-Co^{2+} bond gives rise to strong direct antiferromagnetic exchange between the dopant and an unpaired valence band electron. The contribution from this *p–d* hybridization, $N_0\beta_{\text{hyb}}$, dominates the overall exchange magnitude (i.e., $|N_0\beta| \approx |N_0\beta_{\text{hyb}}| \gg |N_0\alpha|$). In bulk Co^{2+}-doped II–VI chalcogenide DMSs, for example, $N_0\beta$ typically exceeds $N_0\alpha$ by an order of magnitude (20, 160, 161). Analysis of the data in Fig. 35 yielded $N_0\beta = -2.3 \pm 0.3\,\text{eV}$, corresponding to an effective g value of $g_{\text{eff}} \approx 200$ for the Zeeman splitting of the Γ_9 valence band doublet. The band level Zeeman energies calculated from this result are shown in Fig. 35(*a*).

In most DMSs, dopant–host covalencies are the dominant factors governing *sp–d* exchange energies, which in turn are important for the magnetooptical and magnetic applications of this class of materials. Microscopically, the *p–d* hybridization in DMSs may be described within perturbation theory as an admixture of valence band character into the dopant 3*d* wave function (Eq. 12a).

$$\psi'_{3d} = \psi_{3d} - c\psi_L \tag{12a}$$

$$c \approx \frac{-\langle \psi_L \mid \hat{H} \mid \psi_{3d} \rangle}{\Delta \text{VSIE}} \tag{12b}$$

The coefficient of covalency, c, is dependent on the metal–ligand resonance integral (numerator), which is proportional to the metal–ligand orbital overlap (Eq. 12b, where VSIE = valence shell ionization energy). As noted previously (162), this integral is relatively large in ZnO due to the small unit cell dimensions ($a = 3.2495$ Å, $c = 5.2067$ Å) and has been expected to play a major role in determining the magnetic properties of ZnO DMSs. The denominator, $\Delta\text{VSIE} = E_{\text{D}} - E_{\text{A}}$, describes the energetic mismatch between VB and dopant-acceptor wave functions and was defined experimentally for Co^{2+}:ZnO QDs by assignment of the ligand-to-metal charge transfer (LMCT) transition at 25,200 cm^{-1} in Fig. 34, an assignment supported by optical electronegativity arguments (52). The relatively high LMCT energy, which arises from the high electronegativity of the lattice oxos, counterbalances the small unit cell dimensions, and consequently $N_0\beta$ in Co^{2+}:ZnO is in fact similar in magnitude to those of Co^{2+}:ZnSe and Co^{2+}:CdSe (Table I). The $N_0\beta$

TABLE I

Selected Values of $N_0\beta$ (eV) for Co^{2+}- and Mn^{2+}-Doped II–VI Semiconductors

Lattice	Co^{2+}	Reference	Mn^{2+}	Reference
CdTe	−2.33	159	−0.83	159
CdSe	−2.12	159	−1.30	161
ZnTe	−3.03	159	−1.1	161
ZnO	−2.3 (±0.3)	52	−2.4 (±0.3)	161

parameter is described microscopically within the context of a configuration interaction model as shown in Eq. 13 (162, 163), in which its proportionality to the covalency of the dopant–valence-band interaction is evident. The parameters E^- and E^+ correspond to virtual emission from or absorption to a singly occupied t_2 orbital on the dopant.

$$N_0\beta = -\frac{16\langle\psi_{\mathrm{VB}} \mid \hat{H} \mid \psi_{3d}\rangle^2}{S}\left[\frac{1}{E^-}+\frac{1}{E^+}\right] \qquad (13)$$

Note that $N_0\beta$ values in Co^{2+} DMSs are typically greater than in Mn^{2+} DMSs (Table I). These greater values are predicted theoretically, since $N_0\beta$ is inversely proportional to the spin of the dopant, S (Eq. 13), a feature that arises from consideration of the total number of exchange pathways between the VB hole and the dopant.

V. PROCESSING AND FUNCTIONALLY RELEVANT PHYSICAL PROPERTIES

Although this chapter focuses on colloidal nanocrystals, one of the motivations for preparing materials in this form is the flexibility they offer for further processing and application. In this section, we introduce a few examples in which colloidal nanocrystals were used as building blocks to construct more complex architectures having interesting and potentially useful physical properties.

A. Electroluminescent Devices

Several examples have been reported recently of solution-processed multilayer electroluminescence devices incorporating semiconductor nanocrystals as the active recombination centers (16–18, 164). Recently, attention has also turned to hybrid electroluminescent devices involving transition metal-doped nanocrystals (104, 165–167). Although many challenges remain, including more specific exploitation of the dopants in many cases, the devices demonstrated to date represent a new direction in application of doped semiconductor nanocrystals made possible by the compatibility of these luminescent nanocrystals with solution processing methodologies.

In one recent study, Mn^{2+}-doped CdS nanocrystals grown with a ZnS passivating shell were used as the recombination centers in direct current (dc) electroluminescent devices (104). The Mn^{2+}:CdS/ZnS nanocrystals were prepared by the inverse micelle procedure (102) (see Section II.C) and these colloids were incorporated into a multilayer device structure by spin-coat processing. Photoluminescence and electroluminescence spectra from one such ITO//PEDOT-PSS//PVK//CdS:Mn/ZnS//Al multilayer device are shown in Fig. 36(*a*). Whereas the photoluminescence spectrum showed predominantly $\mathrm{Mn}^{2+}\ {}^4T_1 \rightarrow {}^6A_1$ emission, the electroluminescence was red-shifted and broadened, indicating that it was dominated by nanocrystal surface defect emission. Importantly, electroluminescence from the PVK polymer layer (at ~405 nm) was not observed, indicating electron-hole recombination occurred only in the

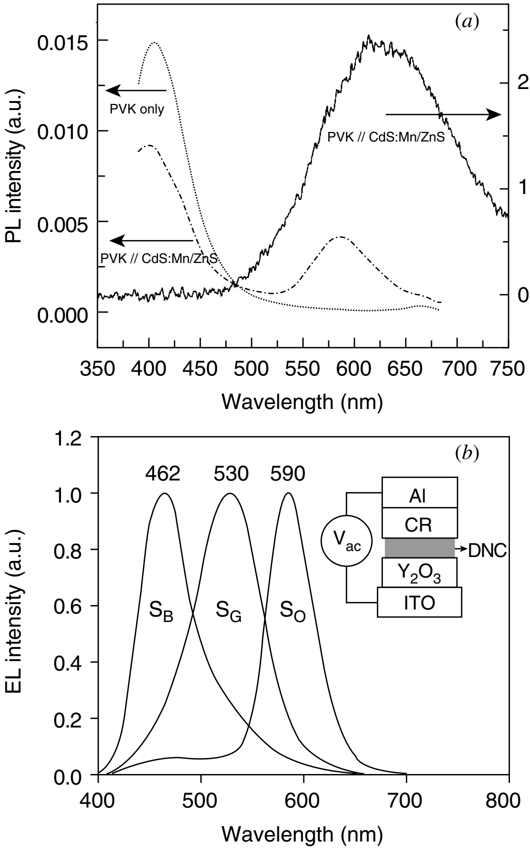

Figure 36. (*a*) Comparison of photoluminescence (360-nm excitation) and dc electroluminescence (16-V applied voltage) spectra obtained from an ITO//PEDOT-PSS//PVK//CdS:Mn/ZnS//Al multilayer electroluminescent device. The photoluminescence spectrum of poly(*N*-vinylcarbazole) (PVK) is included for comparison. [Adapted from (104).] (*b*) The ac electroluminescence spectra of doped ZnS nanocrystals ($S_B = 0.13\%\mathrm{Cu}^+{:}0.1\%\mathrm{Al}^{3+}{:}\mathrm{ZnS}$, sulfide poor, $S_G = 0.13\%\mathrm{Cu}^+{:}\ 0.1\%\mathrm{Al}^{3+}{:}\mathrm{ZnS}$, sulfide rich, $S_O = 0.13\%\mathrm{Cu}^+{:}0.1\%\mathrm{Al}^{3+}{:}0.2\%\mathrm{Mn}^{2+}/\mathrm{ZnS}$, sulfide rich). Inset: Schematic illustration of the multilayer electroluminescent device structure. Turn-on voltages were ~1 V ac @ 100 Hz. [Adapted from (167).]

nanocrystal layer of the device. Electroluminescence was observed only when a positive voltage was applied to the indium tin oxide (ITO) electrode. From the log *I*/log *V* plot, the authors deduced ohmic-like behavior at low voltages (<8 V), suggesting that conductance was limited by the PVK and CdS:Mn/ZnS nanocrystal layers rather than interfaces between them and/or electrode interfaces. At higher voltages (>8 V), the data could be analyzed using the trapped-charge-limited-current model. By changing the organic hole–transport polymer, the band offsets could be adjusted to alter the performance of the device so that radiative electron-hole recombination occurred in the conjugated polymer rather than in the nanocrystalline layer. From these results, the authors concluded that the nanocrystal layer in this latter scenario served as an electron-transport layer with high conductance. These results nicely illustrate the general conclusion that recombination occurs in the nanocrystalline layer when the valence band offset is smaller than the conduction band offset (PVK-based device), and in the conjugated polymer layer when the conduction band offset was less than the valance band offset [poly(*p*-phenylenevinylene) (PPV)-based device].

Strong room temperature alternating current (ac) electroluminescence was recently achieved using ~1–2-nm diameter ZnS nanocrystals codoped with Cu^{+}, Al^{3+}, and Mn^{2+} (167). The nanocrystals were prepared by an aqueous wet-chemical precipitation method (168) and spray coated onto a transparent conducting electrode. The Al^{3+} was likely important for charge compensation to allow incorporation of Cu^{+} at Zn^{2+} sites, although the authors noted the likelihood of Cu^{+} accumulation at the nanocrystal surfaces. The electroluminescence was found to depend strongly on the S^{2-} and Al^{3+} concentrations used during nanocrystal synthesis, shifting from 462 to 530 nm on changing from S^{2-}-poor to S^{2-}-rich synthesis conditions [Fig. 36(*b*)]. This observation was interpreted as indicating the importance of sulfide vacancies (V_S) on the luminescent properties of the nanocrystals. The 462-nm emission was attributed to a V_S–Cu pair transition observed only in the presence of V_S defects. The 530-nm emission was attributed to a Cu–Al pair relaxation that became possible when sulfide vacancies were eliminated though synthesis under S^{2-}-rich conditions. When the nanocrystals were additionally codoped with Mn^{2+}, the characteristic yellow-orange Mn^{2+} $^4T_1 \rightarrow {}^6A_1$ emission was observed in the electroluminescence spectrum, clearly indicating efficient nonradiative energy transfer to the Mn^{2+}. The authors noted the simple processing procedure, low turn-on voltages (~10 V ac @ 100 Hz), and room-temperature operation as advantageous aspects of this electroluminescent device.

B. Photochemistry and Photovoltaics

The generation of H_2 and O_2 from H_2O driven by solar energy has been a long-standing “holy grail” of chemical research. Because H_2 is a storable and renewable fuel whose only combustion product is water, it is one of the most attractive alternatives to fossil fuels. Promising reactivities of microcrystalline transition metal-doped semiconductors such as $Zn_{1-x}Ni_xS$ (169), Sb/Cr-doped TiO_2 (170), and $In_{1-x}Ni_xTaO_4$ (171), have been reported recently for water splitting and other photoredox reactions. In these wide band-gap semiconductors, transition metal impurities sensitize the semiconductor to visible light, allowing solar energy harvesting that is not possible for the pure host semiconductor. Nanocrystals offer the highest surface areas per gram, and so the application of durable doped nanocrystals may be attractive for this and related photoredox catalysis.

Although photochemical water splitting is typically investigated by irradiation of aqueous suspensions of the doped semiconductor powders and monitoring the evolved gasses chromatographically, it is also possible to study photoredox chemistry using regenerative photovoltaic cells. In the traditional Grätzel-type photovoltaic cell configuration (172–174), a highly porous surface is prepared by sintering wide band-gap semiconductor nanocrystals (e.g., TiO_2 or ZnO) onto a transparent conducting electrode (e.g., ITO or $F{:}SnO_2$). Sensitizer chromophores (dyes) are then bound to the large surface area of the nanocrystalline thin film. The most widely employed sensitizers have been ruthenium bipyridyl derivatives such as *cis-bis*(isothiocyanato)*bis*(2,2′-bipyridyl-4,4′-dicarboxylato)ruthenium(II), $[RuL_2(NCS)_2]$. Recently, a few labs have explored the use of QDs of metal sulfides and phosphides as sensitizers of wide-band-gap semiconductors such as TiO_2 (12–14, 175).

Regenerative photovoltaic cells have recently been constructed from thin films of Co^{2+}:ZnO nanocrystals deposited onto ITO transparent conducting electrodes (176) The cobalt ions sensitized the wide-band-gap ZnO to visible irradiation through their $^4A_2 \rightarrow {}^4T_1(P)$ ligand-field absorption, which extends down to 700 nm. Current flow upon white light illumination of the cell with and without a 450-nm long-pass cut-off filter showed that the cobalt ions extended the cell response into the visible energy range [Fig. 37(*a*)] relative to pure ZnO, which absorbs only in the UV. Photocurrent action spectra showed the characteristic Co^{2+} ligand-field absorption fine structure [Fig. 37(*b* and *c*)], verifying that the sensitization came from excitation of the substitutional Co^{2+} dopants. Such action spectra may help to elucidate the mechanisms by which LF excitation leads to current flow, an intriguing aspect of this photochemistry and that of many of the water-splitting catalysts (171). Oxide nanocrystal photovoltaic cells may also hold certain advantages over the widely studied ruthenium dye cells with respect to cost and long-term durability, since doped ZnO nanocrystals are simple and inexpensive to prepare and do not suffer from photodegradation or chromophore desorption. At present, the solar conversion efficiencies of the Co^{2+}:ZnO cells are too low to be competitive. Nevertheless, these cells and the related photocatalysis represent promising applications of

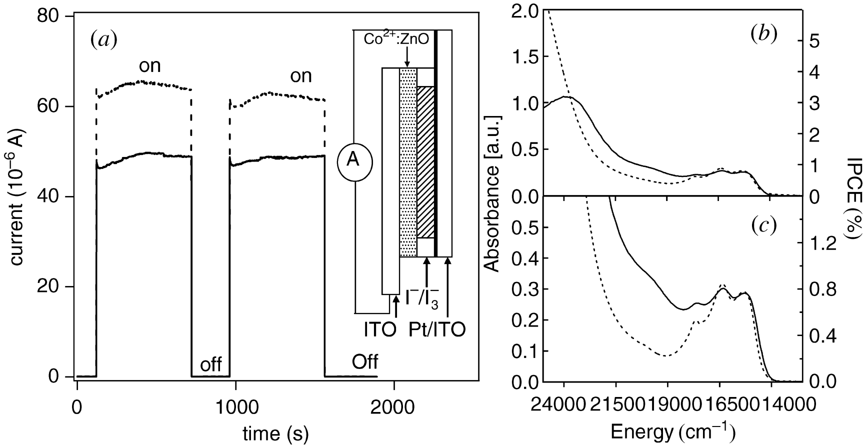

Figure 37. (*a*) Photocurrent plotted versus time for a 5% Co^{2+}:ZnO nanocrystalline Grätzel-type photovoltaic cell, switched between on and off states and illuminated by a 20-W tungsten/halogen bulb using all wavelengths (dashed) or only wavelengths >450 nm (solid). Inset: Schematic of the cell, showing nanocrystalline Co^{2+}:ZnO thin film, ITO and platinum-coated ITO electrodes, and the I^-/I_3^- redox mediator. (*b*) IPCE (solid) and absorption (dashed) spectra of the cell. (*c*) Expanded view of the LF region. [Adapted from (176).]

doped nanocrystals that will be of increasing interest for both fundamental and applied research.

C. High-Curie Temperature (T_C) Ferromagnetism in Aggregates and Nanocrystalline Thin Films

In some cases, the physical properties of collections of nanocrystals may differ substantially from those of the free-standing nanocrystals. A clear example of such a phenomenon is found in the magnetic properties of doped ZnO nanocrystals. In the freestanding Ni^{2+}:ZnO QDs, for example, the Ni^{2+} ions magnetize as paramagnets, displaying their characteristic second-order Zeeman effect giving rise to temperature independent paramagnetism at low temperatures (52, 145). At room temperature, this paramagnetism is very weak, as shown in Fig. 38. Remarkably, the same nanocrystals can be induced to undergo a magnetic transformation if allowed to aggregate slowly at room temperature under reaction limited conditions (Figs. 38 and 39) (154). Reaction-limited aggregation facilitated the formation of dense clusters. Structurally, very little change was observed beyond a small narrowing of the X-ray diffraction peaks. The aggregates showed no order or registry. Magnetically, however, the consequences were quite dramatic, as shown in Fig. 38 (154). The aggregates

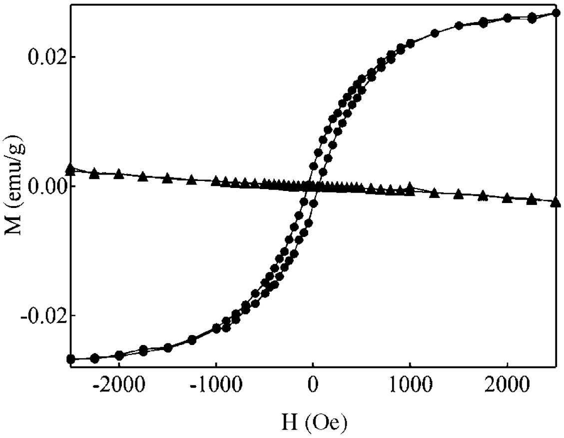

Figure 38. 350 K magnetization of rapidly (▲) and slowly (•) aggregated 0.93% Ni^{2+}:ZnO nanocrystals. [Adapted from (154).]

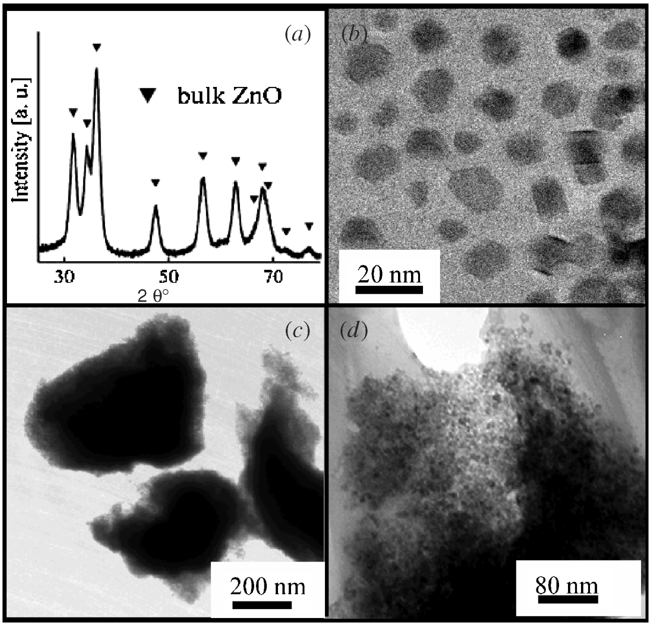

Figure 39. (*a*) XRD spectrum of 0.93% Ni^{2+}:ZnO aggregates prepared by reaction-limited aggregation of colloidal Ni^{2+}:ZnO nanocrystals. The bulk ZnO diffraction pattern is indicated (▼). (*b*) TEM image of freestanding nanocrystals from which the aggregates were prepared. (*c*) The TEM image of the aggregates used for (*a*). (*d*) Selected area TEM image of the same aggregates. [Adapted from (154).]

showed rapid magnetic saturation and a magnetic hysteresis at 300 K, indicative of ferromagnetic ordering at room temperature (154). A similar result was also found for aggregated Co^{2+}:ZnO nanocrystals (52). The emergence of ferromagnetism upon aggregation was attributed primarily to the introduction of donor defects at the fusion interfaces, which generated carriers required for long-range magnetic ordering, but the role of increased domain sizes is likely also important. The Curie temperature, T_C, for this ferromagnetism was found to exceed 350 K.

The ferromagnetism of aggregated TM^{2+}:ZnO nanocrystals was shown to be enhanced by active rather than passive aggregation via spin coating and annealing. For example, very strong and robust ferromagnetism was observed in nanocrystalline thin films of 0.2% Mn^{2+}:ZnO spin coated from colloidal nanocrystals and annealed for 2 min at 525°C between coats (~0.02 mg/coat, 20–40 coats total) (54). Analysis of the XRD peak widths using the Scherrer equation suggested an increase in effective grain diameter from 6 to 20 nm, demonstrating nanocrystal sintering during the brief anneal and 300 K saturation moments as high as 1.35 μ_B/Mn^{2+} were recorded (Fig. 40), nearly one order of magnitude larger than the previously reported room temperature value (177). A distinct ferromagnetic resonance signal was also observed in the EPR spectra of

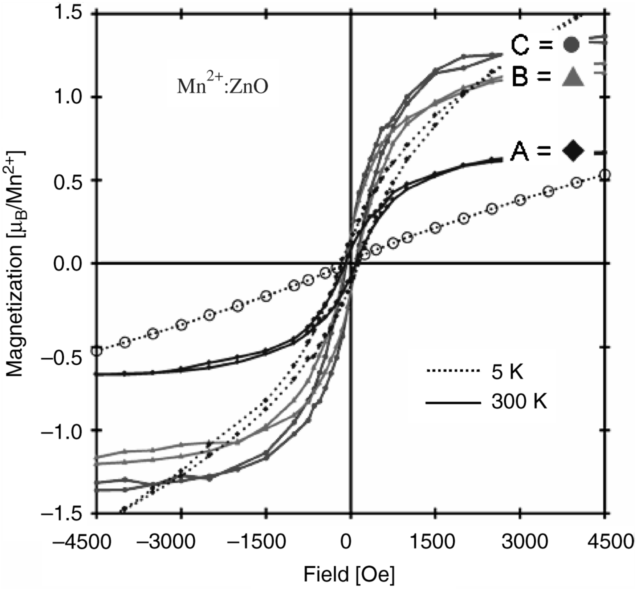

Figure 40. 5K (dotted) and 300 K (solid) magnetic susceptibilities of 0.20% Mn^{2+}:ZnO nanocrystals (○) and several thin films (A–C) prepared by spin-coat processing of the nanocrystals. [Adapted from (54).]

the ferromagnetic films. Quantification of the remaining paramagnetism of the films led to the conclusion that the majority of the Mn^{2+} remained paramagnetic, and hence that the large ferromagnetic saturation moments were in fact lower limits for the maximum values that could be achieved. This example demonstrates a simple case in which colloidal DMS–QDs were used as solution precursors for constructing higher dimensionality DMS nanostructures, and also provides a clear demonstration that the collective properties of doped nanocrystals may differ substantially from those of the individual free-standing nanocrystals.

Although ferromagnetism in DMSs has attracted attention primarily from physicists, these studies also demonstrate that direct chemical routes offer several advantages in this research area, since they may often provide better control over materials composition than is obtained with more traditional high-temperature vacuum deposition and solid-state synthetic techniques. In particular, the latter methods often use dopant source materials that are themselves undesirable contaminants [e.g., manganese oxides for Mn^{2+}:ZnO (177), NiO for Ni^{2+}:ZnO (178), and cobalt oxides or Co metal for Co^{2+}:ZnO (179)] or that require high temperatures and reducing conditions that may promote dopant segregation (180). The advantage of the direct chemical approach is perhaps best illustrated in the case of Ni^{2+}:ZnO, since the solid solubility of Ni^{2+} in ZnO is very low (181), and there is a large driving force for phase segregation. Ni^{2+}:ZnO thin films prepared by pulsed laser deposition (PLD) using NiO as the source of Ni^{2+} showed a magnetic hysteresis only $<5\,K$ (178) that closely resembled the characteristic magnetism of nanoscale NiO (182), raising concerns over the possibility of nanoscale NiO contaminants. In contrast, Ni^{2+}:ZnO DMSs prepared from ionic solutions showed ferromagnetism above room temperature ($T_C > 350\,K$) that was demonstrably an intrinsic property of the Ni^{2+}:ZnO DMS (154).

D. Templated Inverse-Opal Mesostructures

Several groups have reported the use of closest-packed polystyrene spheres to template the formation of inverse opal structures by filling the interstitial voids with a high-index material, followed by calcination of the polystyrene (183–186). Importantly, filling the interstitial volumes with nanocrystals has been found to be more effective than filling with sol–gel precursors because the former yields higher density structures with higher effective refractive indices (186, 187). The use of doped nanocrystals for this purpose would add an additional degree of functionality to the inverse opal, potentially contributing novel luminescent or magnetic properties to the resulting structure. In particular, Er^{3+} doping is attractive for photonic structures because of its 1.5 μm $^4I_{13/2} \rightarrow {}^4I_{15/2}$ emission, which coincides with the telecommunications window.

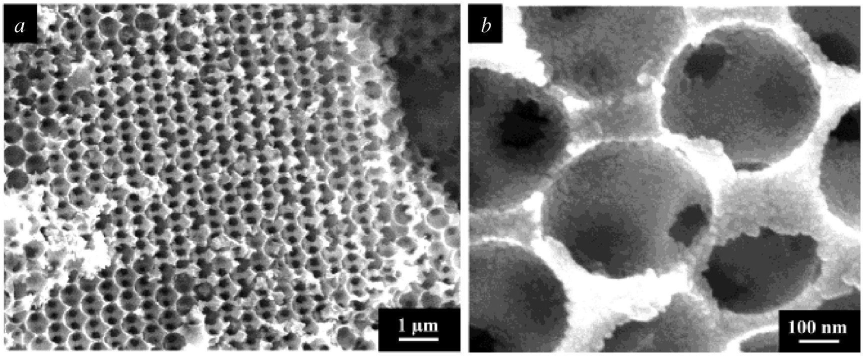

Figure 41. The SEM micrograph images of an Er^{3+}:TiO_2 inverse-opal structure templated using a colloidal crystal of 466-nm polystyrene beads by filling the interstitial volumes with colloidal ~50-nm diameter Er^{3+}:TiO_2 nanocrystals followed by calcination to remove the poylystyrene. (*a*) Low magnification. (*b*) High magnification. [Adapted from (187).]

Sintered erbium-doped TiO_2 nanocrystals have recently been explored as the active media in inverse opal structures prepared as described above (187). Colloidal 1–3% Er^{3+}:TiO_2 (anatase) nanocrystals with ~50-nm diameters were synthesized by sol–gel methods and characterized by X-ray diffraction and TEM. Powders of the nanocrystals did not luminesce until calcined >300°C, after which strong 1532 nm $^4I_{13/2} \rightarrow {}^4I_{15/2}$ emission was observed. These nanocrystals were then infused into the interstitial volume of a polystyrene photonic crystal, and the polystyrene was removed by calcination. The SEM micrographs of the resulting structure are shown in Fig. 41. From these images, it was seen that the TiO_2 nanocrystals preserved the structure of the colloidal template remarkably well. Although no results were reported that described the photonic properties of these Er^{3+}:TiO_2 structures, these images demonstrated the potential to use doped nanocrystals in the formation of photonic structures, and more importantly suggest a wide variety of experiments that could be performed along similar lines with potentially important consequences for telecommunications technologies.

VI. SUMMARY AND OUTLOOK

The body of work presented in this chapter has focused largely on the synthesis of colloidal doped semiconductor nanocrystals, and on the application of a wide variety of characterization techniques to ensure dopant incorporation into the host semiconductor lattice. Although still relatively rare, the high-quality materials prepared by several laboratories in recent years have already allowed detailed spectroscopic and magnetic studies of the physical properties of this new form of materials to be performed. With such high-quality materials now increasingly accessible, one may envision more frequent demonstration of the application of doped nanocrystals as building blocks in self-assembled or hierarchically ordered meso- and microstructures, the diversity of which will be bound only by the imagination of the experimentalist. Future advances will no doubt involve the demonstration of functional single-nanocrystal architectures in which dopants play a key role in governing performance. Electrical doping by some of the methods described here will also become increasingly important as the device structures accessible by self-assembly grow in sophistication, and future experiments will no doubt attempt to develop general methods for synthesizing and characterizing electrically doped nanostructures such as Li^+ or Na^+-doped ZnO nanocrystals(188) and the Sb:SnO_2 nanocrystals described in Section III.D (59–61). Manipulation of electronic carriers in doped nanocrystals will also likely become increasingly important, such as the "charging" of a variety of semiconductor nanocrystals that has been demonstrated using strong chemical reducing agents or electrochemical cells (189–191). New approaches to physical characterization of doped nanocrystals may also be anticipated, such as Z-contrast TEM for depth profiling of dopants within individual crystallites, which would aid the understanding of dopant gradients as discussed in Sections II.B and C and would complement the analogous variable-energy XPS studies discussed in Section III.D. It is hoped that the themes and details described in this chapter will be of assistance to all who are working in these fields and will contribute to the advancement of this exciting young research area.

ACKNOWLEDGMENTS

The original work described herein that was conducted by D.R.G. and co-workers was supported by the National Science Foundation (DMR-0239325 and ECS-0224138), Research Corporation (RI0832), American Chemical Society (ACS-PRF 37502-G), and the Semiconductor Research Corporation (2002-RJ-1051G). D.R.G. is a Cottrell Scholar of the Research Corporation. J.D.B. acknowledges support from the University of Washington/Pacific Northwest National Laboratories Joint Institute for Nanoscience and from the American Chemical Society (PRF-AEF 39844). In addition, we thank Nick Norberg, Kevin Kittilstved, Dana Schwartz, Pavle Radovanovic, William Liu, Paul Archer, Jialong Zhou, Greg Parks, James Kraus, Philip Tregenna-Piggott, Høgni Weihe, Jesper Bendix, Chongmin Wang, Marjorie Olmstead, Scott Chambers, and Kannan Krishnan for direct or indirect contributions to this manuscript and the work contained within.

ABBREVIATIONS

ac	Alternating current
BG	Band gap
CB	Conduction band
CT	Charge transfer
CW	Continuous wave
dc	Direct current
DCI–MS	Desorption chemical ionization—mass spectrometry
DMS	Diluted magnetic semiconductor
DMSO	Dimethyl sulfoxide
DMS–QD	Diluted magnetic semiconductor quantum dot
EDS	Energy dispersive spectroscopy
EDX	Wavelength-dispersive X-ray spectroscopy
EPR	Electron paramagnetic resonance spectroscopy
EXAFS	Extended X-ray absorption fine structure
FT	Fourier transform
fwhm	Full-width at half-maximum
ICP–AES	Inductively coupled plasma atomic emission spectroscopy
ICS	Isocrystalline core–shell procedure
ITO	Indium tin oxide
IPCE	Incident photon to current conversion efficiency
LF	Ligand field
LMCT	Ligand-to-metal charge transfer
MCD	Magnetic circular dichroism
ODMR	Optically detected magnetic resonance
PEDOT	Poly(3,4-ethylenedioxythiophene)
PLD	Pulsed laser deposition
PPV	Poly(*p*-phenylenevinylene)
PSS	Poly(styrene sulfonate)
PVB	Polyvinyl butyral
PVK	Poly(*N*-vinylcarbazole)
Py	Pyridine
QD	Quantum dot
SCC	Single configurational coordinate
SEM	Scanning electron microscopy
SG	Spin glass
T_C	Curie temperature
TEM	Transmission electron microscopy
TOP	Trioctylphosphine
TOPO	Trioctylphosphine oxide

UV	Ultraviolet
WAXS	Wide-angle X-ray scattering
XAS	X-ray absorption spectroscopy
XPS	X-ray photoelectron spectroscopy
XRD	X-ray diffraction
VB	Valence band

REFERENCES

1. A. P. Alivisatos, *J. Phys. Chem.*, *100*, 13226 (1996).
2. C. B. Murray, C. R. Kagan, and M. G. Bawendi, *Annu. Rev. Mater. Sci.*, *30*, 545 (2000).
3. *MRS Bull.*, *23*(2) (1998).
4. *Acc. Chem. Res.*, *32*(5) (1999).
5. A. Eychmüller, *J. Phys. Chem. B*, *104*, 6514 (2000).
6. C. J. Murphy and J. L. Coffer, *Appl. Spectrosc.*, *56*, 16A (2002).
7. M. Shim, C. Wang, D. J. Norris, and P. Guyot-Sionnest, *MRS Bull.*, *26*, 1005 (2001).
8. A. L. Efros and M. Rosen, *Annu. Rev. Mater. Sci.*, *30*, 475 (2000).
9. W. C. W. Chan and S. Nie, *Science*, *281*, 2016 (1998).
10. X. Gao and S. Nie, *Trends Biotechnol.*, *21*, 371 (2003).
11. M. Bruchez, Jr., M. Moronne, P. Gin, S. Weiss, and A. P. Alivisatos, *Science*, *281*, 2013 (1998).
12. A. Zaban, O. I. Micic, B. A. Gregg, and A. J. Nozik, *Langmuir*, *14*, 3153 (1998).
13. R. Plass, S. Pelet, J. Krueger, M. Graetzel, and U. Bach, *J. Phys. Chem. B*, *106*, 7578 (2002).
14. W. U. Huynh, J. J. Dittmer, and A. P. Alivisatos, *Science*, *295*, 2425 (2002).
15. V. I. Klimov, A. A. Mikhailovsky, S. Xu, A. Malko, J. A. Hollingsworth, C. A. Leatherdale, H.-J. Eisler, and M. G. Bawendi, *Science*, *290*, 314 (2000).
16. V. L. Colvin, M. C. Schlamp, and A. P. Alivisatos, *Nature (London)*, *370*, 354 (1994).
17. B. O. Dabbousi, M. G. Bawendi, O. Onitsuka, and M. F. Rubner, *Appl. Phys. Lett.*, *66*, 1316 (1995).
18. S. Coe, W.-K. Woo, M. G. Bawendi, and V. Bulovic, *Nature (London)*, *420*, 800 (2002).
19. J. K. Furdyna and J. Kossut, *Semiconductors and Semimetals*, R. K. Willardson and A. C. Beer, Eds., Academic, New York, 1988.
20. J. K. Furdyna, *J. Appl. Phys.*, *64*, R29 (1988).
21. K. Ando, *Solid-State Sciences: Magneto-Optics*, Springer, Berlin, 2000.
22. S. A. Wolf, D. D. Awschalom, R. A. Buhrman, J. M. Daughton, S. von Molnár, M. L. Roukes, A. Y. Chthelkanova, and D. M. Treger, *Science*, *294*, 1488 (2001).
23. D. D. Awschalom, M. E. Flatté, and N. Samarth, *Sci. Amer.*, *286*, 66 (2002).
24. H. A. Engel, P. Recher, D. Loss, *Solid State Commun.*, *119*, 229 (2001).
25. D. Ferrand, A. Wasiela, S. Tatarenko, J. Cibert, G. Richter, P. Grabs, G. Schmidt, L. W. Molenkamp, and T. Dietl, *Solid State Commun.*, *119*, 237 (2001).

26. B. T. Jonker, Y. D. Park, B. R. Bennett, H. D. Cheong, G. Kioseoglou, and A. Petrou, *Phys. Rev. B: Condens. Matter*, *62*, 8180 (2000).
27. Y. Ohno, D. K. Young, B. Beschoten, F. Matsukura, H. Ohno, and D. D. Awschalom, *Nature (London)*, *402*, 790 (1999).
28. H. Ohno, F. Matsukura, and Y. Ohno, *JSAP Int.*, *5*, 4 (2002).
29. V. N. Golovach and D. Loss, *Semicond. Sci. Technol.*, *17*, 355 (2002).
30. R. Fiederling, M. Keim, G. Reuscher, W. Ossau, G. Schmidt, A. Waag, and L. W. Molenkamp, *Nature (London)*, *402*, 787 (1999).
31. C. Rüster, T. Borzenko, C. Gould, G. Schmidt, L. W. Molenkamp, X. Liu, T. H. Wojtowicz, J. K. Furdyna, Z. G. Yu, and M. E. Flatté, *Phys. Rev. Lett.*, *91*, 216602 (2003).
32. A. L. Efros, E. I. Rashba, and M. Rosen, *Phys. Rev. Lett.*, *87*, 206601 (2001).
33. R. N. Bhargava, D. Gallagher, X. Hong, and A. Nurmikko, *Phys. Rev. Lett.*, *72*, 416 (1994).
34. Y. Wang, N. Herron, K. Moller, and T. Bein, *Solid State Commun.*, *77*, 33 (1991).
35. A. A. Bol and A. Meijerink, *Phys. Rev. B: Condens. Matter*, *58*, R15997 (1998).
36. B. A. Smith, J. Z. Zhang, A. Joly, and J. Liu, *Phys. Rev. B: Condens. Matter*, *62*, 2021 (2000).
37. J. H. Chung, C. S. Ah, and D.-J. Jang, *J. Phys. Chem. B*, *105*, 4128 (2001).
38. N. Murase, R. Jagannathan, Y. Kanematsu, M. Watanabe, A. Kurita, K. Hirata, T. Yazawa, and T. Kushida, *J. Phys. Chem. B*, *103*, 754 (1999).
39. H. Bednarski, J. Cisowski, and J. C. Portal, *J. Cryst. Growth*, *184/185*, 996 (1998).
40. R. Behringer, *J. Chem. Phys.*, *29*, 537 (1958).
41. Y. Shapira, S. Foner, D. H. Ridgley, K. Dwight, and A. Wold, *Phys. Rev. B: Condens. Matter*, *30*, 4021 (1984).
42. H. Bednarski, J. Cisowski, and J. C. Portal, *Phys. Rev. B: Condens. Matter*, *55*, 15762 (1997).
43. E. I. Solomon and M. A. Hanson, *Inorganic Electronic Structure and Spectroscopy*, E. I. Solomon and A. B. P. Lever, Eds., Wiley-Interscience, New York, 1999.
44. E. I. Solomon, M. L. Kirk, D. R. Gamelin, and S. Pulver, *Methods Enzymol.*, *246*, 71 (1995).
45. J. Kossut, *Acta Phys. Pol. A. Supp.*, *100*, 111 (2001).
46. J. Seufert, G. Bacher, M. Scheibner, A. Forchel, S.-I. Lee, M. Dobrowolska, and J. K. Furdyna, *Phys. Rev. Lett.*, *88*, 027402 (2002).
47. F. V. Mikulec, M. Kuno, M. Bennati, D. A. Hall, R. G. Griffin, and M. G. Bawendi, *J. Am. Chem. Soc.*, *122*, 2532 (2000).
48. W. B. Jian, J. Fang, T. Ji, and J. He, *Appl. Phys. Lett.*, *83*, 3377 (2003).
49. D. J. Norris, N. Yao, F. T. Charnock, and T. A. Kennedy, *Nano Lett.*, *1*, 3 (2001).
50. T. Ji, W.-B. Jian, and J. Fang, *J. Am. Chem. Soc.*, *125*, 8448 (2003).
51. P. V. Radovanovic, N. S. Norberg, K. E. McNally, and D. R. Gamelin, *J. Am. Chem. Soc.*, *124*, 15192 (2002).
52. D. A. Schwartz, N. S. Norberg, Q. P. Nguyen, J. M. Parker, and D. R. Gamelin, *J. Am. Chem. Soc.*, *125*, 13205 (2003).
53. D. A. Schwartz and D. R. Gamelin, *Proc. SPIE-Int. Soc. Opt. Eng.*, *5224*, 1 (2003).
54. N. S. Norberg, K. R. Kittilstved, J. E. Amonette, R. K. Kukkadapu, D. A. Schwartz, and D. R. Gamelin, *J. Am. Chem. Soc.*, 126, 30, 9387 (2004).
55. J. D. Bryan, S. M. Heald, S. A. Chambers, and D. R. Gamelin, *J. Am. Chem. Soc.*, *126*, 11640 (2004).
56. P. Yang, L. Cheng, N. Hua, and Y. Du, *Mater. Lett.*, *57*, 794 (2002).
57. Y. Wang, H. Cheng, Y. Hao, J. Ma, W. Li, and S. Cai, *Thin Solid Films*, *349*, 120 (1999).

58. S. R. Davis, A. V. Chadwick, and J. D. Wright, *J. Phys. Chem. B*, *101*, 9901 (1997).
59. T. Nutz, U. zum Felde, and M. Haase, *J. Chem. Phys.*, *110*, 12142 (1999).
60. J. Rockenberger, U. zum Felde, M. Tischer, L. Troger, M. Haase, and H. Weller, *J. Chem. Phys.*, *112*, 4296 (2000).
61. C. McGinley, H. Borchert, M. Pflughoefft, S. Al Moussalami, A. R. B. de Castro, M. Haase, H. Weller, and T. Möller, *Phys. Rev. B: Condens. Matter*, *64*, 245312/1 (2001).
62. P. Archer, P. V. Radovanovic, and D. R. Gamelin, in preparation.
63. G. Counio, S. Esnouf, T. Gacoin, and J.-P. Boilot, *J. Phys. Chem.*, *100*, 20021 (1996).
64. N. Feltin, L. Levy, D. Ingert, and M. P. Pileni, *J. Phys. Chem. B*, *103*, 4 (1999).
65. L. Levy, D. Ingert, N. Feltin, and M. P. Pileni, *Adv. Mater.*, *10*, 53 (1998).
66. L. Levy, N. Feltin, D. Ingert, and M. P. Pileni, *Langmuir*, *15*, 3386 (1999).
67. D. M. Hoffman, B. K. Meyer, A. I. Ekimov, I. A. Merkulov, A. L. Efros, M. Rosen, G. Counio, T. Gacoin, and J.-P. Boilot, *Solid-State Commun.*, *114*, 547 (2000).
68. P. V. Radovanovic and D. R. Gamelin, *J. Am. Chem. Soc.*, *123*, 12207 (2001).
69. O. E. Raola and G. F. Strouse, *Nano Letters*, *2*, 1443 (2002).
70. K. M. Hanif, R. W. Meulenberg, and G. F. Strouse, *J. Am. Chem. Soc.*, *124*, 11495 (2002).
71. C. A. Stowell, R. J. Wiacek, A. E. Saunders, and B. A. Korgel, *Nano Lett.*, *3*, 1441 (2003).
72. V. K. LaMer and R. H. Dinegar, *J. Am. Chem. Soc.*, *72*, 4847 (1950).
73. T. Sugimoto, *Adv. Colloid Interfac. Sci.*, *28*, 65 (1987).
74. D. W. Oxtoby, *Acc. Chem. Res.*, *31*, 91 (1998).
75. L. Vegard and H. Schjelderup, *Physik. Z.*, *18*, 93 (1917).
76. X. Peng, J. Wickham, and A. P. Alivisatos, *J. Am. Chem. Soc.*, *120*, 5343 (1998).
77. L. Qu, W. W. Yu, and X. Peng, *Nano Lett.*, *4*, 465 (2004).
78. W. W. Yu, L. Qu, W. Guo, and X. Peng, *Chem Mater.*, *15*, 2854 (2003).
79. L. Hiltunen, M. Leskela, M. Makela, and L. Niinisto, *Acta. Chem. Scand. A*, *41*, 548 (1987).
80. M. Kohls, M. Bonanni, L. Spanhel, D. Su, and M. Giersig, *Appl. Phys. Lett.*, *81*, 3858 (2002).
81. N. N. Greenwood, *Ionic Crystals, Lattice Defects, and Nonstoichiometry*, Chemical Pub. Co., New York, 1970.
82. G. Counio, T. Gacoin, and J.-P. Boilot, *J. Phys. Chem. B*, *102*, 5257 (1998).
83. A. A. Bol, R. van Beek, and A. Meijerink, *Chem. Mater.*, *14*, 1121 (2002).
84. J. Kraus and D. R. Gamelin (unpublished results).
85. K. J. Davis, P. M. Dove, and J. J. De Yoreo, *Science*, *290*, 1134 (2000).
86. M. A. Malik, P. O'Brien, and N. Revaprasadu, *J. Mater. Chem.*, *11*, 2382 (2001).
87. T. Trindale and P. O'Brien, *Adv. Mater.*, *8*, 161 (1996).
88. M. A. Malik, N. Revaprasadu, and P. O'Brien, *Chem. Mater.*, *13*, 913 (2001).
89. S. L. Cumberland, K. M. Hanif, A. Javier, G. A. Khitrov, G. F. Strouse, S. M. Woessner, and C. S. Yun, *Chem. Mater.*, *14*, 1576 (2002).
90. T. J. J. Norman, D. Magana, T. Wilson, C. Burns, J. Z. Zhang, D. Cao, and F. Bridges, *J. Phys. Chem. B.*, *107*, 6309 (2003).
91. P. V. Radovanovic and D. R. Gamelin, *Proc. SPIE-Int. Soc. Opt. Eng.*, *4807*, 223 (2002).
92. H. A. Weakliem, *J. Chem. Phys.*, *36*, 2117 (1962).
93. A. B. Greytak, L. J. Lauhon, M. S. Gudiksen, and C. M. Lieber, *Appl. Phys. Lett.*, *84*, 4176 (2004).
94. M. A. Hines and P. Guyot-Sionnest, *J. Phys. Chem.*, *100*, 468 (1996).

95. B. O. Dabbousi, J. Rodriguez-Viejo, F. V. Mikulec, J. R. Heine, H. Mattoussi, R. Ober, K. F. Jensen, and M. G. Bawendi, *J. Phys. Chem. B*, *101*, 9463 (1997).
96. D. V. Talapin, A. L. Rogach, A. Kornowski, M. Haase, and H. Weller, *Nano Lett.*, *1*, 207 (2001).
97. A. V. Baranov, Y. P. Rakovich, J. F. Donegan, T. S. Perova, R. A. Moore, D. V. Talapin, A. L. Rogach, Y. Matsumoto, and I. Nabiev, *Phys. Rev. B: Condens. Matter*, *68*, 165306 (2003).
98. J. J. Li, A. Y. Wang, W. Guo, J. C. Keay, T. D. Mishima, M. B. Johnson, and X. Peng, *J. Am. Chem. Soc.*, *125*, 12567 (2003).
99. I. Mekis, D. V. Talapin, A. Kornowski, M. Haase, and H. Weller, *J. Phys. Chem. B*, *107*, 7454 (2003).
100. X. Peng, M. C. Schlamp, A. V. Kadavanich, and A. P. Alivisatos, *J. Am. Chem. Soc.*, *119*, 7019 (1997).
101. L. Cao, J. Zhang, S. Ren, and S. Huang, *Appl. Phys. Lett.*, *80*, 4300 (2002).
102. H. Yang and P. H. Holloway, *Appl. Phys. Lett.*, *82*, 1965 (2003).
103. H. Yang and P. H. Holloway, *Adv. Funct. Mater.*, *14*, 152 (2004).
104. H. Yang and P. H. Holloway, *J. Phys. Chem. B*, *107*, 9705 (2003).
105. X. Zhong, Y. Feng, W. Knoll, and M. Han, *J. Am. Chem. Soc.*, *125*, 13559 (2003).
106. A. R. West, *Solid State Chemistry*, Wiley, Chichester, 1992.
107. R. Jenkins, Snyder, R., *Introduction to X-ray Powder Diffractometry*, Vol. 138, John Wiley & Sons, Inc., New York, 1996.
108. U. Hotje, C. Rose, and M. Binnewies, *Solid State Sci.*, *5*, 1259 (2003).
109. V. Jayaram and B. S. Rani, *Mater. Sci. Eng., A*, *304–306*, 800 (2001).
110. S. Jimenez-Sandoval, A. Lopez-Rivera, and J. C. Irwin, *Phys. Rev. B.*, *68*, 054303 (2003).
111. D. L. Peterson, A. Petrou, W. Giriat, A. K. Ramdas, and S. Rodriguez, *Phys. Rev. B: Condens. Matter*, *33*, 1160 (1986).
112. E.-K. Suh, A. Arora, K., A. K. Ramdas, and S. Rodriguez, *Phys. Rev. B: Condens. Matter*, *45*, 3360 (1992).
113. C. D. Wagner, W. M. Riggis, L. E. Davis, J. F. Moulder, and G. E. Mulenberg, *Handbook of X-Ray Photoelectron Spectroscopy*, Perkin Elmer, Eden Prarie, MN, 1979.
114. J. E. B. Katari, V. L. Colvin, and A. P. Alivisatos, *J. Phys. Chem.*, *98*, 4109 (1994).
115. Y. Cao and U. Banin, *J. Am. Chem. Soc.*, *122*, 9692 (2000).
116. H. Borchert, S. Haubold, M. Haase, H. Weller, C. McGinley, M. Riedler, and T. Moeller, *Nano Lett.*, *2*, 151 (2002).
117. A. V. Chadwick and G. E. Rush, *Characterization of Nanocrystalline Oxides by EXAFS Spectroscopy*, Kluwer, Norwell, MA, 2002.
118. Y. L. Soo, Z. H. Ming, S. W. Huang, Y. H. Kao, R. N. Bhargava, and D. Gallagher, *Phys. Rev. B: Condens. Matter*, *50*, 7602 (1994).
119. R. Bouchet, A. Weibel, P. Knauth, G. Mountjoy, and A. V. Chadwick, *Chem. Mater.*, *15*, 4996 (2003).
120. L. Levy, D. Ingert, N. Feltin, V. Briois, and M.-P. Pileni, *Langmuir*, *18*, 1490 (2002).
121. S. R. Davis, A. V. Chadwick, and J. D. Wright, *J. Mater. Chem.*, *8*, 2065 (1998).
122. A. A. Bol, R. van Beek, J. Ferwerda, and A. Meijerink, *J. Phys. Chem. Sol.*, *64*, 247 (2003).
123. K. Klein, J. Dreyhsig, H.-E. Gumlich, M. Thiede, G. Goetz, H.-J. Schultz, and J. W. Allen, *Phys. Status Solidi A*, *130*, K207 (1992).
124. R. N. Bhargava, *J. Lumin.*, *70*, 85 (1996).
125. R. N. Bhargava, *J. Cryst. Growth*, *214–215*, 926 (2000).

126. F. Jain and W. Huang, *J. Appl. Phys.*, *85*, 2706 (1999).
127. K. Yan, C. Duan, Y. Ma, S. Xia, and J.-C. Krupa, *Phys. Rev. B: Condens. Matter*, *58*, 13585 (1998).
128. G. F. Imbush, *Luminescence Spectroscopy*, M. D. Lumb, Ed., Academic Press, New York, 1978.
129. A. B. P. Lever, *Inorganic Electronic Spectroscopy*, Elsevier Science Publishers, Amsterdam, The Netherlands, 1984, and references cited therein.
130. W. Chen, R. Sammynaiken, Y. Huang, J.-O. Malm, R. Wallenberg, J.-O. Bovin, V. Zwiller, and N. A. Kotov, *J. Appl. Phys.*, *89*, 1120 (2001).
131. M. McCarthy and D. R. Gamelin (unpublished results).
132. J. Dreyhsig and J. W. Allen, *J. Phys.: Condens. Matter*, *1*, 1087 (1989).
133. J. Yu, H. Liu, Y. Wang, and W. Jia, *J. Lumin.*, *79*, 191 (1998).
134. F. G. Anderson, W. M. Dennis, and G. F. Imbush, *J. Lumin.*, *90*, 27 (2000).
135. H.-S. Yang, K. S. Hong, S. P. Feofilov, B. M. Tissue, R. S. Meltzer, and W. M. Dennis, *J. Lumin.*, *83–84*, 139 (1999).
136. A. J. Nozik, *Annu. Rev. Phys. Chem.*, *52*, 193 (2001).
137. C. B. Murray, S. Sun, H. Doyle, and T. Betley, *MRS Bull.*, *26*, 985 (2001).
138. S. Jin, D. Whang, M. C. McAlpine, R. S. Friedman, Y. Wu, and C. M. Lieber, *Nano Lett.*, *4*, 915 (2004).
139. Z. Zhong, D. Wang, Y. Cui, M. W. Bockrath, and C. M. Lieber, *Science*, *302*, 1377 (2003).
140. H. C. Jeon, Y. S. Jeong, T. W. Kang, T. W. Kim, K. J. Chung, K. J. Chung, W. Jhe, and S. A. Song, *Adv. Mater.*, *14*, 1725 (2002).
141. S. A. Chambers, T. Droubay, C. M. Wang, A. S. Lea, R. F. C. Farrow, L. Folks, V. Deline, and S. Anders, *Appl. Phys. Lett.*, *82*, 1257 (2003).
142. B.-S. Jeong, Y. W. Heo, D. P. Norton, J. G. Kelly, R. Rairigh, A. F. Hebard, J. D. Budai, and Y. D. Park, *Appl. Phys. Lett.*, *84*, 2608 (2004).
143. A. Hausmann and H. Huppertz, *J. Phys. Chem. Sol.*, *29*, 1369 (1968).
144. P. B. Dorain, *Phys. Rev.*, *112*, 1058 (1958).
145. P. Koidl, *Phys. Rev. B: Condens. Matter*, *15*, 2493 (1977).
146. W. H. Brumage and C. C. Lin, *Phys. Rev.*, *134*, A950 (1964).
147. P. M. Shand, A. Lewicki, I. Miotkowski, B. C. Crooker, and J. K. Furdyna, *Phys. Rev. B: Condens. Matter*, *44*, 6152 (1991).
148. A. Twardowski, H.J.M.Swagten, and W. J. M. Dejonge, *Cobalt Based II-VI Semimagnetic Semiconductors*, World Scientific, Singapore, 1993.
149. K. Ueda, H. Tabata, and T. Kawai, *App. Phys. Lett.*, *79*, 988 (2001).
150. Y. M. Cho, W. K. Choo, H. Kim, D. Kim, and Y. Ihm, *App. Phys. Lett.*, *80*, 3358 (2002).
151. H. Saeki, H. Tabata, and T. Kawai, *Sol. State Commun.*, *120*, 439 (2001).
152. D. P. Norton, S. J. Pearton, A. F. Hebard, N. Theodoropoulou, L. A. Boatner, and R. G. Wilson, *App. Phys. Lett.*, *82*, 239 (2003).
153. A. Tuan, J. D. Bryan, A. Pakomov, V. Shutthanandan, S. Thevuthasan, D. McCready, D. Gaspar, M. Engelhard, J. W. Rogers, Jr., K. M. Krishnan, D. R. Gamelin, and S. A. Chambers, *Phys. Rev. B: Condens. Matter*, *70*, 054424 (2004).
154. P. V. Radovanovic and D. R. Gamelin, *Phys. Rev. Lett.*, *91*, 157202/1 (2003).
155. S. A. Chambers, Y. K. Yoo, and Eds., *MRS Bull.*, *23*, 706 (2003).
156. S. I. Gubarev, *J. Lumin.*, *52*, 193 (1992).
157. A. K. Bhattacharjee, *Phys. Rev. B: Condens. Matter*, *58*, 15660 (1998).

158. S. B. Piepho and P. N. Schatz, *Group Theory in Spectroscopy with Applications to Magnetic Circular Dichroism*, John Wiley & Sons, Inc., New York, 1983.
159. H. Alawadhi, I. Miotkowski, V. Souw, M. McElfresh, A. K. Ramdas, and S. Miotkowska, *Phys. Rev. B: Condens. Matter*, *63*, 155201 (2001).
160. P. Kacman, *Semicond. Sci. Technol.*, *16*, R25 (2001).
161. T. Dietl, H. Ohno, and F. Matsukura, *Phys. Rev. B: Condens. Matter*, *63*, 195205 (2001).
162. J. Blinowski, P. Kacman, and T. Dietl, *arXiv: cond-mat/0201012 VI* (2002).
163. A. K. Bhattacharjee, *Phys. Rev. B: Condens. Matter*, *46*, 5266 (1992).
164. S. Chaudhary, M. Ozkan, and W. C. W. Chan, *Appl. Phys. Lett.*, *84*, 2925 (2004).
165. J. Huang, Y. Yang, S. Xue, B. Yang, S. Liu, and J. Shen, *Appl. Phys. Lett.*, *70*, 2335 (1997).
166. W. Que, Y. Zhou, Y. L. Lam, Y. C. Chan, C. H. Kam, B. Liu, L. M. Gan, C. H. Chew, G. Q. Xu, S. J. Chua, S. J. Xu, and F. V. C. Mendis, *Appl. Phys. Lett.*, *73*, 2727 (1998).
167. K. Manzoor, S. R. Vadera, N. Kumar, and T. R. N. Kutty, *Appl. Phys. Lett.*, *84*, 284 (2004).
168. K. Manzoor, S. R. Vadera, N. Kumar, and T. R. N. Kutty, *Mat. Chem. Phys.*, *82*, 718 (2003).
169. A. Kudo and M. Sekizawa, *Chem. Commun.*, 1371 (2000).
170. H. Kato and A. Kudo, *J. Phys. Chem. B*, *106*, 5029 (2002).
171. Z. Zou, J. Ye, K. Sayama, and H. Arakawa, *Nature (London)*, *414*, 625 (2001).
172. M. Gratzel, *J. Photochem. Photobiol. C*, *4*, 145 (2003).
173. A. Hagfeldt and M. Gratzel, *Acc. Chem. Res.*, *33*, 269 (2000).
174. M. K. Nazeeruddin and M. Gratzel, *Comprehensive Coordination Chemistry II*, J. A. McCleverty and T. J. Meyer, Eds., Elsevier, Oxford, 2004.
175. A. J. Nozik, *Physica E*, *14*, 115 (2002).
176. W. Liu and D. R. Gamelin (to be published).
177. P. Sharma, A. Gupta, K. V. Rao, F. J. Owens, R. Sharma, R. Ahuja, J. M. Osorio Guillen, B. Johansson, and G. A. Gehring, *Nature Mater.*, *2*, 673 (2003).
178. T. Wakano, N. Fujimura, Y. Morinaga, N. Abe, A. Ashida, T. Ito, *Physica E*, *10*, 260 (2001).
179. K. Rode, A. Anane, R. Mattana, J.-P. Contour, O. Durand, R. LeBourgeois, *J. Appl. Phys.*, *91*, 7676 (2003).
180. J. H. Kim, H. Kim, D. Kim, Y. E. Ihm, W. K. Choo, *J. Appl. Phys.*, *92*, 6066 (2002).
181. M. Lo Jacano, P. Porta, A. Cimino. *J. Sol. State Chem..*, *3*, 501 (1971).
182. R. H. Kodama, S. A. Makhlouf, A. E. Berkowitz. *Phys. Rev. Lett.*, *79*, 1393 (1997).
183. A. Stein and R. C. Schroden, *Curr. Opinion Sol. State Mater. Chem.*, *5*, 553 (2001).
184. R. W. J. Scott, S. M. Yang, G. Chabanis, N. Coombs, D. E. Williams, and G. A. Ozin, *Adv. Mater.*, *13*, 1468 (2001).
185. Y. Xia, B. Gates, Y. Yin, and Y. Lu, *Adv. Mater.*, *12*, 693 (2000).
186. G. Subramanian, V. N. Manorahan, J. D. Thorne, and D. J. Pine, *Adv. Mater.*, *11*, 1261 (1999).
187. S. Jeon and P. V. Braun, *Chem. Mater.*, *15*, 1256 (2003).
188. S. B. Orlinskii, J. Schmidt, P. G. Baranov, D. M. Hofmann, C. de Mello Donega, and A. Meijerink, *Phys. Rev. Lett.*, *92*, 047603 (2004).
189. M. Shim and P. Guyot-Sionnest, *Nature (London)*, *407*, 981 (2000).
190. C. Wang, M. Shim, and P. Guyot-Sionnest, *Science*, *291*, 2390 (2001).
191. A. L. Roest, J. J. Kelly, D. Vanmaekelbergh, and E. A. Meulenkamp, *Phys. Rev. Lett.*, *89*, 036801 (2002).